Organic Light-Emitting Diodes: Development of Electrode and Multilayer Deposition Processes

Dissertation

Zur Erlangung des akademischen Grades

Doctor rerum naturalium (Dr. rer. nat)

Im Fach Physik

Spezialisierung: Experimentalphysik

eingereicht an der

Mathematisch-Naturwissenschaftlichen Fakultät

der Humboldt-Universität zu Berlin

von

M.Sc. Michael Hengge

Präsidentin der Humboldt-Universität zu Berlin

Prof. Dr. Julia von Blumenthal

Dekanin der Mathematisch-Naturwissenschaftlichen Fakultät

Prof. Dr. Caren Tischendorf

Betreuer:	Prof. Dr. Emil List-Kratochvil
Co-Betreuer:	Dr. Felix Hermerschmidt
Gutachter/innen:	1. Prof. Dr. Emil List-Kratochvil
	2. Prof. Dr. Eva Unger
	3. Prof. Stelios Choulis, PhD
Tag der mündlichen Prüfung:	27.04.2023

Selbstständigkeitserklärung

Hiermit erkläre ich, die Dissertation selbstständig und nur unter Verwendung der angegebenen Hilfen und Hilfsmittel angefertigt zu haben. Ich habe mich nicht anderwärts um einen Doktorgrad in dem Promotionsfach beworben und besitze keinen entsprechenden Doktorgrad. Die Promotionsordnung der Mathematisch-Naturwissenschaftlichen Fakultät, veröffentlicht im Amtlichen Mitteilungsblatt der Humboldt-Universität zu Berlin Nr. 42 am 11. Juli 2018 habe ich zur Kenntnis genommen.

_____

Datum   Michael Hengge

Acknowledgments

Zusammenfassung

Organische Leuchtdioden weisen, verglichen mit anorganischen Leuchtdioden, viele Vorteile auf. So sind sie nicht nur energiesparender in der Display- und Beleuchtungstechnik einsetzbar, sondern können auch in neuen flexiblen Technologien verwendet werden. Um ihr volles Potenzial auszuschöpfen, können einem herkömmlichen OLED-Aufbau zusätzliche Schichten und neue Materialien hinzugefügt werden. Der Ersatz spröder Elektroden durch dünne Metallschichten kann OLEDs flexibler machen, Zwischenschichten verbessern den Ladungstransport und neuartige Materialien können die Lösungsprozessierung von OLEDs vereinfachen. In den Kapiteln dieser Arbeit wurden je ein Ansatz zur Steigerung der Leistung von OLEDs untersucht.

Es wurden dünne Silberschichten aus einer partikelfreien Silbertinte mittels Tintenstrahldruck hergestellt und ihre optischen sowie elektrischen Eigenschaften mit mechanischen, optischen und elektrischen Messverfahren charakterisiert. Einige der dazu notwendigen Messaufbauten zur Messung der Leuchtdichte und externen Quanteneffizienz der Dioden, sowie der Trübung wurden speziell für diese Arbeit angefertigt. Die gedruckten Elektroden zeigen eine hohe Biegefestigkeit, bei gleichbleibend guten elektrischen Eigenschaften. Die damit hergestellten Leuchtdioden übertreffen in ihrer Effizienz Referenzdioden mit Indium Zinn Oxid Elektroden. Da Silberelektroden aufgrund (elektro-)chemischer Reaktionen im Kontakt mit anderen Schichten nicht für alle Zwecke geeignet sind, wurde eine partikelfreie Goldtinte untersucht, um eine inertere Alternative herzustellen. Aus dieser Tinte wurden mittels eines Rakelverfahrens Elektroden hergestellt und ihre Eigenschaften im Vergleich zu den Silberelektroden analysiert.

Um die Effizienz organischer Leuchtdioden weiter steigern zu können wurden anschließend Zwischenschichten aus neuartigen Materialkombinationen untersucht. Mittels einer binären Zwischenschicht aus Zinkoxid und einem Polymer konnte die Leuchtstärke und Effizienz von invertierten Leuchtdioden signifikant gesteigert werden. Die Erforschung der optimalen Herstellungsparameter mittels optischer und elektrischer Analysemethoden wurde durchgeführt. Weiterhin wurden zwei neu synthetisierte Moleküle dazu verwendet, um die Benetzung von Perowskiten auf Elektroden zu verbessern und somit ihre Herstellbarkeit mittels Tintenstrahldruck zu ermöglichen. Diese Perowskite wurden dann zum Nachweis der Machbarkeit erfolgreich in Solarzellen eingesetzt.

Durch das zuvor erwähnte Einfügen von Zwischenschichten in organischen Leuchtdioden lassen sich zwar deren Eigenschaften stark verbessern, jedoch ergeben sich neue Herausforderungen, wenn mehrere solcher Schichten aus Lösungen prozessiert werden sollen. In diesem Fall wird meist nach einem sogenannten orthogonalen Lösemittelsystem gesucht. In diesem Ansatz lösen sich bereits hergestellte Schichten nicht im nachfolgend verwendeten Lösungsmittel. Jedoch ist solch ein System nicht für alle Materialkombinationen vorhanden. Das Quervernetzen von Polymeren stellt in diesem Fall einen alternativen Lösungsansatz dar. Hierbei wird ein die Löslichkeit eines Polymers durch verschiedene Ansätze verringert. Mittels eines neu-synthetisierten Quervernetzers wurde dieses Prinzip anhand des lichtemittierenden Polymers Super Yellow demonstriert. Die Beständigkeit einer Schicht aus Super Yellow gegenüber Toluol konnte erfolgreich stark erhöht werden. Somit wurde eine nachfolgende Prozessierung einer zusätzlichen Schicht aus demselben Lösungsmittel ermöglicht. Erneut konnte die Effizienz von organischen Leuchtdioden durch das Hinzufügen dieser Zwischenschichte gesteigert werden.

Abstract

Organic light-emitting diodes have many advantages compared to their inorganic counterparts. Not only can they be used more energy-efficiently in display and lighting technology, but they can also be used in new, flexible technologies. To reach their full potential, additional layers and new materials can be added to a conventional OLED structure. Replacing brittle electrodes with thin metal layers can make OLEDs more flexible, intermediate layers improve charge transport, and novel materials can simplify solution processing of OLEDs. In each of the chapters of this thesis, an approach to increasing the performance of OLEDs was examined.

Thin silver layers were produced from a particle-free silver ink using inkjet printing to replace brittle indium tin oxide electrodes. Their optical and electrical properties were characterized using mechanical, optical, and electrical measurement methods. Some of the necessary measurement setups for determining the luminance and external quantum efficiencies of the diodes, as well as the haze, were purpose-built for this work. The printed electrodes show a high flexural strength while retaining good electrical properties. The efficacy of the light-emitting diodes produced in this way exceeds that of reference diodes with indium tin oxide electrodes. Since silver electrodes are not suitable for all purposes due to (electro)chemical reactions when in contact with other layers, a particle-free gold ink was investigated to fabricate a more inert, alternative. Electrodes were produced from this ink using a doctor blade process and their properties were analyzed in comparison to the silver electrodes.

To be able to further increase the efficiency of organic light-emitting diodes, intermediate layers made of new material combinations were subsequently investigated. The luminosity and efficiency of inverted light-emitting diodes could be significantly increased by means of a binary intermediate layer made of zinc oxide and a polymer. Using optical and electrical analysis methods, the optimal manufacturing parameters were studied. Furthermore, two newly synthesized molecules were used to improve the wetting of perovskites on electrodes and thus enable their manufacturability using inkjet printing. These perovskites were then successfully used in solar cells to prove their feasibility.

Although the above-mentioned insertion of intermediate layers in organic light-emitting diodes can greatly improve their properties, new challenges arise if several such layers are to be processed from solutions. In this case, a so-called orthogonal solvent system is usually employed. With this approach, layers that have already been produced do not dissolve in the solvent used subsequently. However, such a system is not readily available for all material combinations. If so, the crosslinking of polymers represents an alternative approach. Here, the solubility of a polymer is reduced by various approaches. Using a newly synthesized crosslinker, this principle was demonstrated using the light-emitting polymer Super Yellow. The resistance of a layer of Super Yellow against toluene was successfully increased significantly. Thus, subsequent processing of an additional layer from the same solvent was made possible. Again, the efficacy of organic light-emitting diodes produced with this intermediate layer could be boosted.

Table of Contents

List of Abbreviations

ASTM	American Society for Testing and Materials
CIE	Commission Internationale de l'Éclairage
CL	Crosslinker
DMD	Dielectric-Metal-Dielectric
DOD	Drop-On-Demand
DSC	Differential Scanning Calorimetry
EBL	Electron blocking Layer
EIL	Electron Injection Layer
EL	Electroluminescence
EML	Emission Layer
EQE	External Quantum Efficiency
FF	Fill Factor
FOM	Figure of Merit
FTIR	Fourier-Transformed Infrared Spectroscopy
FTO	Fluorine-Doped Tin Oxide
HOMO	Highest Occupied Molecular Orbital
IE	Ionization Energy
IR	Infrared
ITO	Indium Tin Oxide
JVL	Current Density-Voltage-Luminance
LED	Light-Emitting Diode
LUMO	Lowest Unoccupied Molecular Orbital
MOD	Metal-Organic Decomposition
MPP	Maximum Power Point
NP	Nanoparticle
OWRK	Owens, Wendt, Rabel, and Kaelble
PCE	Power Conversion Efficiency
PE	Polyethylene
PEDOT	Poly(3,4-ethylenedioxythiophene)
PEG	Polyethylene Glycol
PEI	Polyethyleneimine
PET	Polyethylenterephthalat
PI	Polyimine
PL	Photoluminescence
PLQY	Photoluminescence Quantum Yield
PP	Polypropylene
PPV	Polyphenylene-Vinylene
PSC	Perovskite Solar Cells
PSS	Polystyrene Sulfonate
PTAA	Poly[bis(4-phenyl)(2,4,6-trimethylphenyl)amine
PYS	Photoelectron Yield Spectroscopy
PSC	Perovskite Solar Cell
SEM	Scanning Electron Microscopy
SFM	Scanning Force Microscopy
SY	Super Yellow
TADF	Thermally Activated Delayed Fluorescence
TFB	poly(9,9-dioctylfluorene-alt-N-(4-sec-butylphenyl)-diphenylamine)
TGA	Thermogravimetric Analysis
TNA	Trinaphthylamine
TPA	Triphenylamine
TPD	N,N′-Bis(3-methylphenyl)-N,N′-diphenylbenzidine
UPS	Ultraviolet Photoelectron Spectroscopy
UV	Ultraviolet
WF	Work Function
XPS	X-Ray Photoelectron Spectroscopy
XRD	X-Ray Powder Diffraction

1 Introduction

This chapter provides a short motivation of the scope and applicability of this work. It summarizes the single chapters are summarized, and a graphical overview is given.

1.1 Motivation

Electric lighting technology has undergone a drastic development in the last years. In the 1880s, arc lights that used an electric arc between carbon electrodes to generate light were used. Due to their harsh light and high power consumption, these were only applied for street lighting and large halls. Incandescent and fluorescent lights were employed in indoor lighting as soon as suitable electrical grids were available. In the decades after, the advancement of lighting technologies was mainly accomplished by improvements to existing technologies such as the introduction of the tungsten filament in 1910. Only in 1962 came the next big step with the commercial introduction of the light-emitting diode (LED) by Texas Instruments. In the beginning, only infrared diodes were available, but soon the first red LED in the visible spectrum was produced. Since it had a very high initial price of 200 US dollars it was only used in high-end equipment, but prices fell down to just a few cents in the 1970s.[1] Other colors such as green or yellow followed soon, but there was a lack of material to produce a blue-emitting LED. This was a huge drawback since blue light is needed for the creation of white light and multicolor displays. Blue LEDs based on a doped gallium nitride material were first available in the 1990s.[2] Since then, developments of new and improved display and lighting applications centered on LED technology have been ongoing. The development of the organic light-emitting diode (OLED) has just been the latest step in a continuous quest for new and enhanced lighting technologies.

In practical display applications such as panels for TVs or smartphones, LED technology is still the de-facto standard today. However, as energy efficiency is becoming more of a focus for consumers, displays with OLED technology are on the rise.[3] LED displays make use of LEDs only as a white backlight, while colors are added by utilizing color filters. In most devices, the backlight is always turned on, therefore using energy, even when a black screen is displayed. OLEDs, on the other hand, are used directly as light-emitting pixels and therefore only consume energy when a pixel is on. This enables, for example, the production of so-called "always-on" displays, where part of the screen is never switched off (for example the digits of a smart watch), while still maintaining good battery life. As a positive side effect, this also gives OLED displays a comparably better contrast between dark and bright pixels. However, OLED displays can suffer from burn-in since the OLED sub-pixels, especially the blue ones, are prone to degradation.[4] This can lead to burned-in artifacts in areas of the display where there is no picture change for a long time, e.g., a battery icon.

Compared to the first generation of OLED consumer devices, the stability, as well as the lifetime, have been drastically improved in the last years with operating lifetimes (lifetime T_{50}, half the initial brightness) of 900 000 h for red and 400 000 h for green OLEDs. Blue OLEDs still suffer from faster degradation with a lifetime of only 20 000 h.[5] However, inorganic LED displays still surpass OLEDs in terms of efficacy, low production cost, and durability. Therefore, it is crucial to investigate the influences certain OLED layers can have on their performance and to improve the fabrication process. New, more resource-saving manufacturing techniques such as solution processing must be studied, and additional materials have to be analyzed to improve the device's performance. Finally, emerging technologies such as flexible displays require established processes to be adapted to meet consumer demands for thinner and more flexible applications.

1.2   Thesis Outline

This work deals with the production of organic optoelectronic components. While the focus lies on the improvement and adaptation of organic light-emitting diodes (OLEDs) for future applications such as flexible electronics, perovskite solar cells (PSC) will also be investigated briefly. Strategies to facilitate and scale device production and approaches to improve device efficiency will be discussed theoretically as well as experimentally. Generally, this thesis consists of the following chapters:

Chapter 2 gives a theoretical background to the topic of this thesis. Based on an introduction to the fundamental interactions between light and matter, organic semiconductors, electrodes, and hybrid systems are discussed. Finally, the two optoelectronic components, the OLED and the solar cell are introduced, and their properties are described.

Chapter 3 contains an explanation of the experimental methods. Processing methods used, such as spin coating, vapor deposition, or inkjet printing are introduced. Characterization equipment for optical, elemental, or morphological analysis is described. In the last part, beginning from section 3.2.8, special emphasis is placed on custom-made setups for the characterization of organic light-emitting diodes (current-voltage-luminance characterization as well as external quantum yield), electrode laser structuring, bending tests, and a setup for haze measurements.

Chapter 4 deals with the solution processing of flexible electrodes. Here, a particle-free silver ink is employed to fabricate thin transparent metal films. The produced films are characterized and compared to commercial indium tin oxide (ITO) electrodes in terms of their optical and electrical properties. Rigid as well as flexible OLEDs are fabricated with both electrodes and their properties are analyzed. In the second part, a brief evaluation of gold electrodes for future optoelectronic applications is made.

Chapter 5 describes possibilities to enhance surface properties by adding injection- and interlayers. This section is split into two main parts. The first part introduces a composite mixture of zinc oxide nanoparticles and polyethylenimine that is utilized to significantly enhance the performance of inverted OLEDs by improving the electron injection. In the second part, two novel molecules are applied as a wetting enhancement to facilitate the solution processing (spin coating and inkjet printing) of perovskite layers for perovskite solar cells. Their chemical, optical and morphological properties are assessed in detail prior to the fabrication of perovskite solar cells.

Chapter 6 investigates the possibilities of crosslinking to manufacture multilayer devices. A short introduction to crosslinking techniques is given first. Afterward, optimization processes for the crosslinking process are described. The chapter concludes with the fabrication and characterization of multilayer OLEDs, including an electron blocking layer in comparison with standard OLEDs.

A general conclusion of the results of this thesis, an outlook for future continuation of this work, a list of references, as well as an appendix with additional information can be found after the main text. A graphical representation of this thesis in form of an OLED overview is shown in Figure 1.1.

Top Electrode:
· Theory: Sec. 2.3

Emissive Layer:
· Theory: Sec. 2.2.3
· Crosslinking: Ch. 6

Transparent Electrode:
· Theory: Sec. 2.3.1
· Silver: Sec. 4.1
· Gold: Sec. 4.2

Injection & Transport:
· Theory: Sec. 2.2.1
· Interlayers: Sec. 5.1
· Wetting: Sec. 5.2
· Blocking: Sec. 6.5

Substrate:
· Haze: Sec. 3.2.8
· Bending: Sec. 3.2.9
· Structuring: Sec. 3.2.12
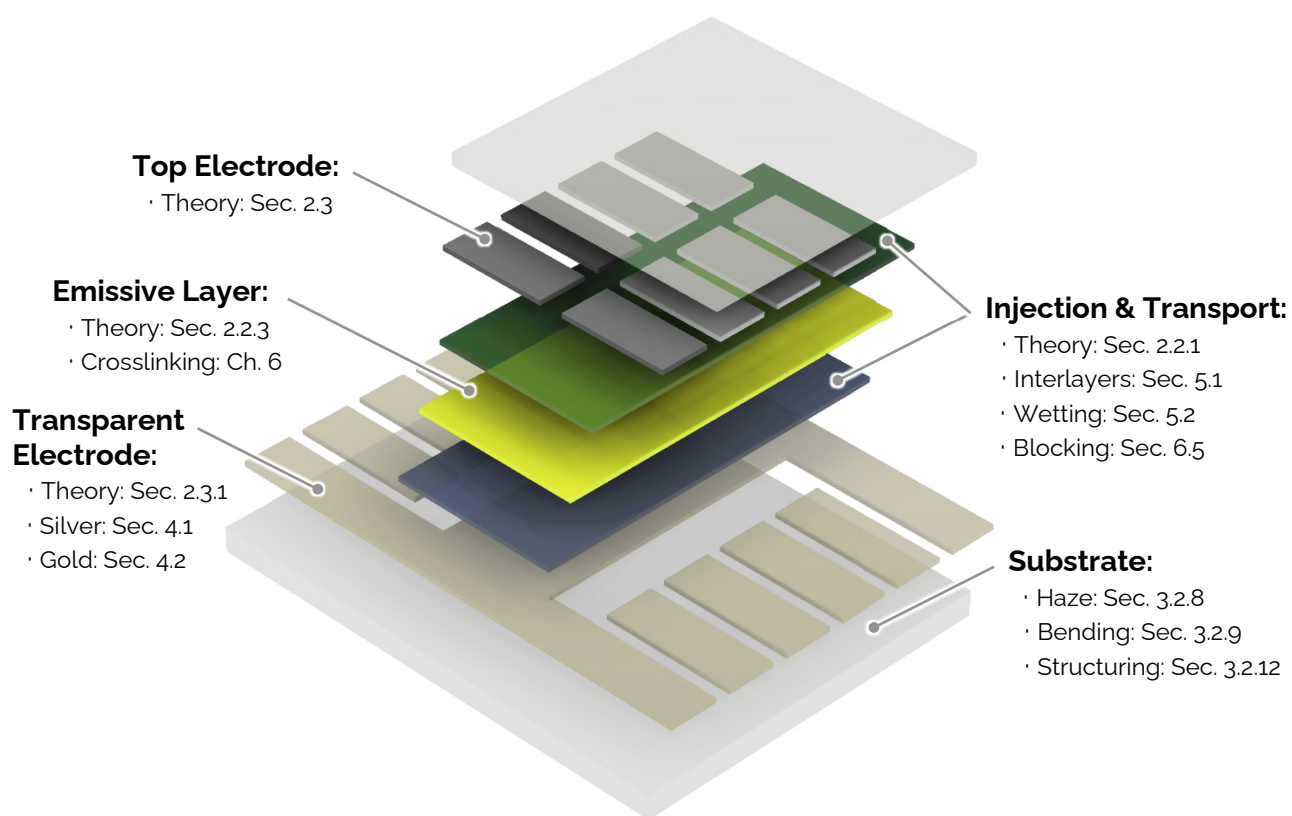
Figure 1.1. Exploded view of an organic light-emitting diode giving an overview of the topics of this thesis. The individual components are examined in more detail in the specified chapters or sections.

2 Fundamentals

In this chapter, the fundamental concepts of organic semiconductors will be discussed. The basic interactions of light and matter are briefly described and their practical application in organic semiconductors is explored. Different types of electrode materials are introduced and the interplay between organic and inorganic layers is analyzed. Finally, the working principles and characteristics of optoelectronic devices are depicted. While the focus lies on organic light-emitting diodes, the structure of hybrid solar cells is briefly examined as well since novel materials are employed in solar cells throughout this thesis.

2.1   Interactions of Light and Matter

This section gives a brief introduction to the interactions between light and matter. Starting from very basic reflection and transmittance laws, the focus will gradually shift to a more detailed description of the atomic processes of light absorption and color perception. General knowledge of these processes is crucial for the description and understanding of OLEDs and solar cells later in this work.

2.1.1   Transmission, Reflectance, and Absorption

One of the most fundamental physical laws every physics student will learn is the basic law of (specular) reflection. Known already to the ancient Greeks,[6] it states that the angle of the incident light θ_i is equal to the angle of the reflected light θ_r:

$$\Theta_i = \Theta_r \tag{2.1}$$

When light is not fully reflected, it enters from one medium into the other and is refracted based on the relation of the refractive indices of the two materials. Snell's law describes the relationship between the refractive indices $n_{1,2}$ and the angles:

$$n_1 \sin \Theta_1 = n_2 \sin \Theta_2 \tag{2.2}$$

This relation is valid since the speed of light in a medium is different from that in a vacuum. It is dependent on the permittivity and permeability of the material. Looking at light in more detail, it can be described as a wave of alternating electric and magnetic fields. Depending upon the fluctuation of the field in relation to the plane of incident, two polarization states of light can be defined. S-polarization (from the German senkrecht, meaning perpendicular), where the fluctuations of the electric field happen perpendicular to the plane of incident i.e., the magnetic field fluctuates in-plane, and P-polarization (parallel), where the electric field is in the plane of incident light (see Figure 2.1).
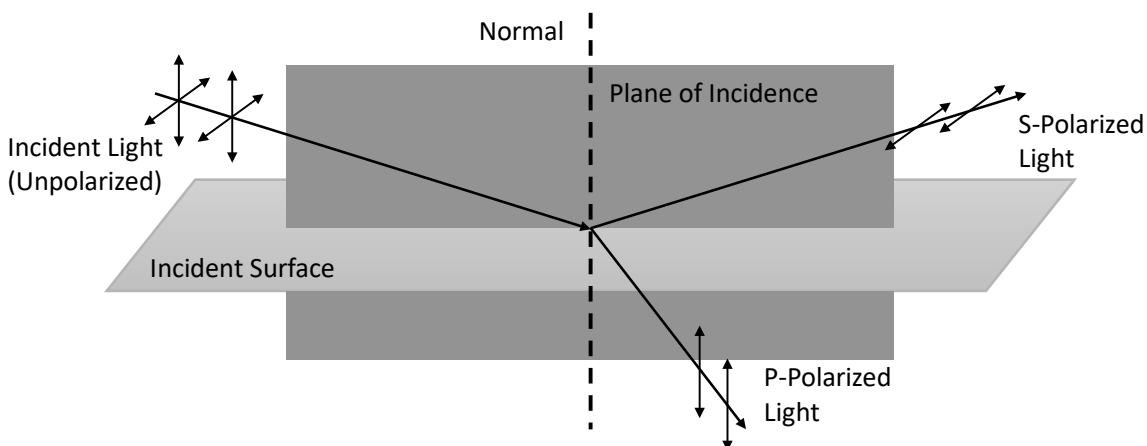

Figure 2.1. Definition of S- and P-polarized light. S-polarized light is perpendicular to the plane of incidence while P-polarized light refers to the parallel component. Unpolarized light contains both components.

The three general types of light polarization (linear, circular, and elliptical) can then be expressed as a combination of the two orthogonal s and p polarizations. Returning to the case of light and a medium, the Fresnel coefficients describe the reflection amplitudes ($r_{s,p}$) and transmission ($t_{s,p}$) amplitudes of s or p-polarized light as:

$$r_s = \frac{n_1 \cos \Theta_i - n_2 \cos \Theta_t}{n_1 \cos \Theta_i + n_2 \cos \Theta_t} \tag{2.3}$$

$$t_s = \frac{2n_1 \cos \Theta_i}{n_1 \cos \Theta_i + n_2 \cos \Theta_t} \tag{2.4}$$

$$r_p = \frac{n_2 \cos \Theta_i - n_1 \cos \Theta_t}{n_2 \cos \Theta_i + n_2 \cos \Theta_t} \tag{2.5}$$

$$t_p = \frac{2n_1 \cos \Theta_i}{n_2 \cos \Theta_i + n_1 \cos \Theta_t} \tag{2.6}$$

When calculating the reflection or transmission of light through a medium, the amplitude of the light waves is often less important than the power since power can be measured directly. In general, the power is proportional to the square of the amplitudes, meaning that the power coefficients for reflected (called reflectance, R) and transmitted (transmittance, T) light can be calculated from the amplitudes as follows:

$$R = |r|^2 \tag{2.7}$$

$$T = \frac{n_2 \cos \Theta_t}{n_1 \cos \Theta_i} |t|^2 \tag{2.8}$$

The calculation of R is much simpler due to the fact that both the incident and reflected wave travel in the same medium. If one now wants to include the absorbance in this picture of light interaction, a simple relation can be found. Since no light is lost, the absorbance A together with the reflectance and transmittance must add up to one and the unknown quantity can be calculated from the other two, i.e.

$$A + R + T = 1 \tag{2.9}$$

The absorbance can also be described by introducing a complex refractive index $\boldsymbol{n}$:

$$\boldsymbol{n} = n - i\kappa \tag{2.10}$$

While n is the same refractive index as before, κ is called the extinction coefficient and describes the attenuation of light when it enters a medium. Inserted into the equation of the electromagnetic wave, one obtains an attenuation term that describes the intensity of the light in relation to the penetration depth x into the material:

$$I(x) = I_0 e^{-\frac{4\pi\kappa x}{\lambda_0}}, \tag{2.11}$$

where I_0 is the initial light intensity and λ_0 is the light's wavelength in a vacuum. Introducing an absorption coefficient α as follows:

$$\alpha = \frac{4\pi\kappa}{\lambda_0},$$ (2.12)

results in the Beer-Lambert law, an essential law to a multitude of optical techniques (see for example section 3.2.1):

$$I(x) = I_0 e^{-\alpha x}$$ (2.13)

2.1.2 Radiometry, Photometry, and Human Color Perception

After describing the absorption of light, a description of the emitted light is necessary as well. When characterizing different light sources, it is important to measure the absolute light intensity that they emit. However, the human eye has different sensitivity across the visible spectrum (380–780 nm). Red and especially blue light of the same absolute intensity seems to the human eye less bright than green light. In 1924, the Commission Internationale d'Eclairage (CIE) conducted an experiment with more than 100 participants and asked them to match the brightness of lights of different wavelengths.[7] Figure 2.2a shows the results of this study for high light levels (photopic, daylight vision) and low light levels (scotopic, night vision). With bright light, daylight for example, the maximum eye sensitivity for humans occurs at 555 nm. This curve, called the photopic response curve or photopic luminous efficiency function $V(\lambda)$, now enables the conversion from units relating to absolute light intensity (radiometry) to human-adapted intensities (photometry) by multiplying the radiometric units with $V(\lambda)$.
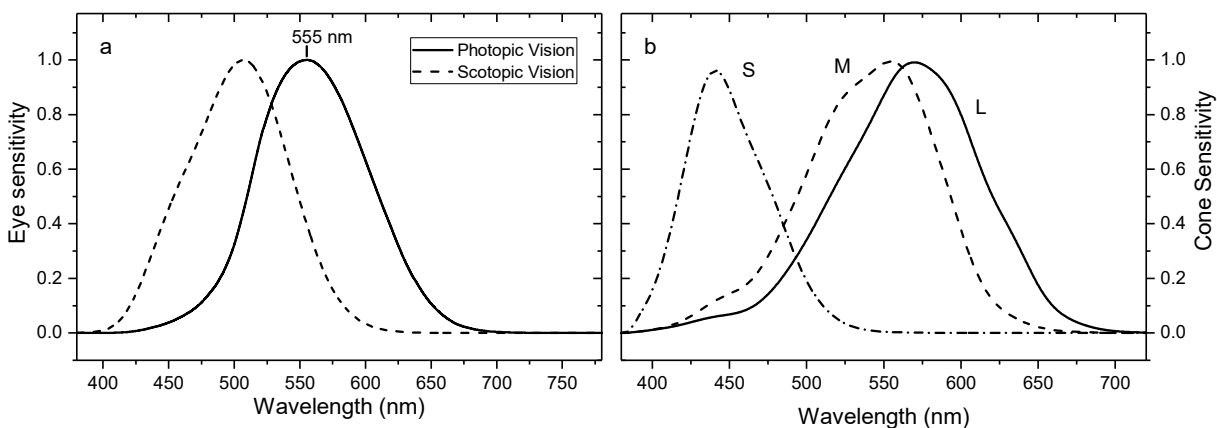
Figure 2.2. The human eye responds differently to different wavelengths of light. (a) Photopic and scotopic eye response curves with a perceived maximum at 555 nm. (b) Normalized sensitivity for human cone cells. The short, medium and long wavelength cones have different maxima which enables color vision. Data from reference.[8]

In radiometry, the output power (flux) of a light source is measured in watts, while the correction with the luminous efficiency function yields the photometric unit lumen.

Table 2.1 gives an overview of the important radiometric quantities and their photometric analogies. Measurements of light-emitting devices are usually performed using photometric quantities, most importantly the luminance (see section 3.2.10).

Table 2.1. Comparison of important radiometric and photometric quantities. The photometric quantities can be obtained by scaling the radiometric quantities with the luminous efficiency function.

Rad. Quantity	Symbol	Unit	Phot. Quantity	Symbol	Unit
Radiant Flux	Φ_e	J s^{-1} = W	Luminous Flux	Φ_v	lm
Radiant Energy	Q_e	J	Luminous Energy	Q_v	lm s
Radiant Intensity	$I_{e,}$	W sr^{-1}	Luminous Intensity	I_v	lm sr^{-1} = cd
Irradiance	E_e	W m^{-2}	Illuminance	E_v	lm m^{-2} = lx
Radiance	L_e	W sr^{-1} m^{-2}	Luminance	L_v	lm sr^{-1} m^{-2} = cd m^{-2}

Human eyes have three receptors for color vision. These have different sensitivities for different wavelengths. There exists one receptor with a maximum sensitivity for short wavelengths, one for medium, and one for long wavelengths as displayed in Figure 2.2b. The classical picture of the red, green, and blue receptors is not absolutely correct, since both the medium and the long-range receptors have their maximum sensitivity in the green wavelength area (S-receptor: 440 nm, L-receptor: 560 nm, M-receptor: 530 nm).

To have an accurate and distinct description of colors, W. D. Wright and J. Guild performed color matching experiments in 1931.[9,10] Participants were asked to recreate a given color by combining three primary light sources with wavelengths of 700 nm, 546.1 nm, and 435.8 nm. However, it turned out that not all colors are reproducible by any three wavelengths and participants had to add some "negative" colored light to the target color in order to accurately recreate any given color. These experiments resulted in the so-called 1931 RGB color matching functions shown in Figure 2.3a.
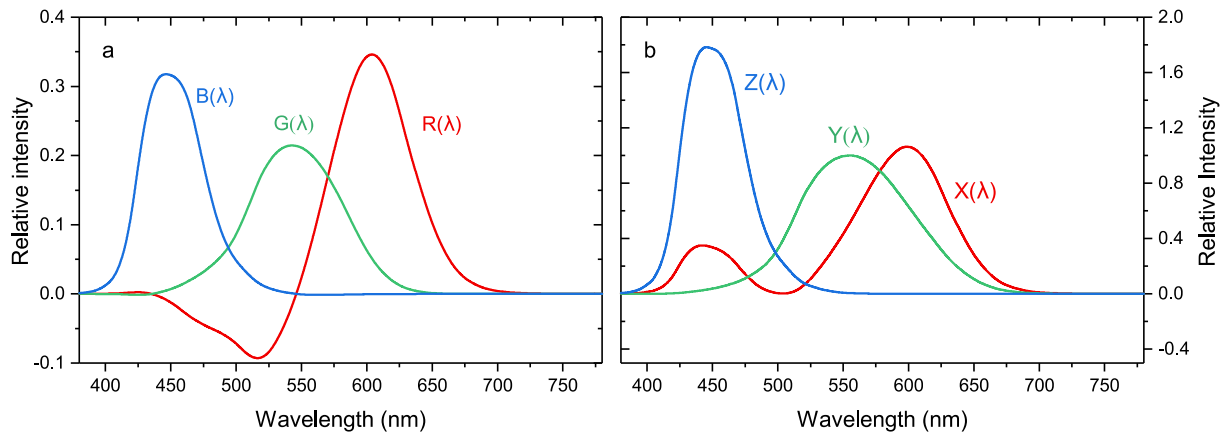

Figure 2.3. Color matching functions. (a) The RGB color matching functions were modeled after experiments with human vision. However, they exhibit undesirable properties such as negative numbers. (b) A mathematical transformation (eq. 2.17) yields the XYZ color matching functions. Additionally, the Y function now closely matches the photopic eye sensitivity (see Figure 2.2a).

From these functions, the tristimulus chromaticity coordinates r, g, and b can be calculated:

$$r = \frac{R}{R + G + B},\tag{2.14}$$

$$g = \frac{G}{R + G + B},\tag{2.15}$$

$$b = \frac{B}{R + G + B},\tag{2.16}$$

Where R, G, and B are the values from the color matching functions corresponding to a particular wavelength. The chromaticity coordinates add up to one so that only two coordinates need to be determined at any time.

The system defined by the above equations has some shortcomings. Calculating with the RGB color functions requires negative numbers which could not be easily handled by computers in the 1930s. Additionally, it would be preferable if one of the color functions closely matched the luminosity function $V(\lambda)$. This would imply that the perceived brightness of any color could be easily determined by regarding one of that color's primary values. Finally, equal values for all the coordinates should produce white. A linear transformation was therefore introduced to obtain a new color space, denoted with XYZ coordinates:

$$\begin{pmatrix} X \\ Y \\ Z \end{pmatrix} = \begin{pmatrix} 2.768 & 1.751 & 1.13 \\ 1 & 4.59 & 0.06 \\ 0 & 0.056 & 5.594 \end{pmatrix} \cdot \begin{pmatrix} R \\ G \\ B \end{pmatrix}\tag{2.17}$$

For these new coordinates, using the same relations as in equations (2.14)-(2.16) yields the xyz coordinates. Since these again add up to one, the three-dimensional color space can be projected to a two-dimensional one without losing any information. A projection to the xy space is usually chosen, which results in the CIE 1931 color diagram as presented in Figure 2.4. This graph shows the spectral colors as the contour of the chart (called the spectral locust). The area within this contour, called the color scale, contains all the colors humans can perceive. At the equality point, where x = y = ⅓, lies pure white.

With this diagram, colors displayable with any display or projector can be established. When the primary colors of the display's subpixels are marked in the CIE diagram, they form a triangle. This subset of the full-color gamut is reproducible with the chosen primary colors. The triangle marked in Figure 2.4 shows a hypothetical color gamut with primary wavelengths of 610, 550, and 465 nm. However, since most real-life displays use LEDs that do not emit monochromatic light, they have color gamuts such as the sRGB or Adobe RGB gamut which, again, can only display a subset of all perceivable colors. When fabricating light-emitting devices the CIE 1931 x and y coordinates are used to give an accurate, comparable representation of the device's color.
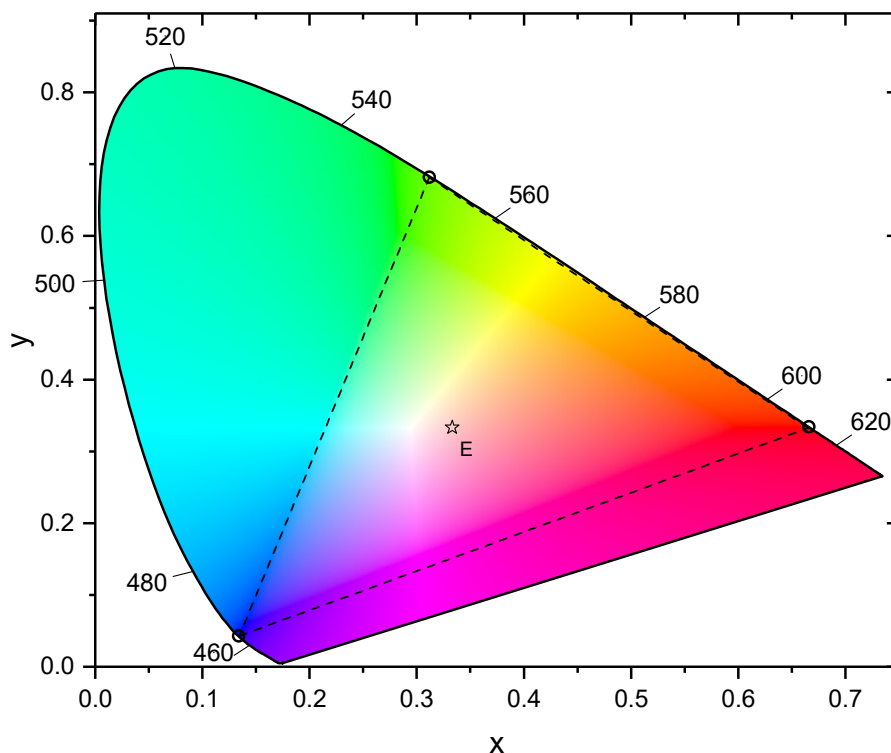
Figure 2.4. CIE 1931 color diagram. The outside lines show spectral colors. All colors in the confined area are mixtures of multiple spectral wavelengths. If the wavelengths marked with circles were chosen as primary colors, then all colors within the triangle gamut would be displayable. The equality point is marked with a star.

2.2 Organic Semiconductors

The discovery of the ability of organic matter to conduct electricity is fairly recent. To understand the processes leading to conductivity in polymers, it is best to first start with the conduction of inorganic materials. The combination of atoms into molecules and how this process leads to conductivity is considered. From there the similarities and differences between conduction organic and inorganic materials are discussed. Finally, the theory of conduction along long chains of polymers is examined.

In an isolated atom, electrons are present in electronic orbitals. These orbitals do not show the concrete position of each electron but rather describe the probability of finding an electron inside the orbital's volume.[11] Going from the simplest of atoms, hydrogen, with only one electron and hence also just one orbital, to more complicated ones, the shape of the orbitals gets more intricate as well since no two electrons are allowed to be in the same quantum state. When multiple of these atoms combine, forming a chemical bond, atomic orbitals interact with each other. Again, since electrons in the same state are forbidden, atomic orbitals must split into molecular orbitals with each having a slight difference in energy. Once a sufficiently large number of atoms interact, forming a solid, the energetic difference between the molecular orbitals becomes so minute that they can be treated as one continuous orbital, a so-called energy band.[12]

11

Once again, describing the exact location and energy of each electron in the bands is not possible, but an important quantity is given by the so-called Fermi level.[13] This describes the energy level with an energy μ (also written as E_F) at a temperature T which has a 50% probability of being occupied by an electron as described by the Fermi-Dirac distribution:

$$f(\varepsilon) = \left(e^{\frac{\varepsilon - \mu}{k_B T}} + 1 \right)^{-1} \tag{2.18}$$

The bands on either side of the Fermi level are of special importance. Below the Fermi level lies the valence band. Electrons in this band take part in the bond formation between atoms and are therefore more strongly bound to the cores. The conduction band, with an energy higher than E_F, contains delocalized electrons that can move freely through the solid and are responsible for electric conduction. In some materials, there exists an energetic gap between the two bands where no allowed electronic states exist, the band gap. The size of this gap, together with the relative location of the Fermi level to the gap, allows different classes of materials to be distinguished (see also Figure 2.5a):

Insulators: If the energy level μ lies within a gap and this gap has a sufficient size (there is conflicting information about the necessary band gap for insulators, however, most sources seem to agree that the band gap needs to surpass 4 eV) the material is called an insulator. The valence band is fully occupied but the band gap is too large for electrons to pass into the conduction band at room temperatures (however, at very high temperatures conductivity can be observed). Therefore, no electrical conduction occurs.

Metals: This material class is the opposite of insulators. The conduction and valence band overlap without any gap in between, and the Fermi level lies in the interior of the bands. Electrical conduction is directly possible even at absolute zero temperatures. If the temperature is increased, the conductivity of metals is decreased due to increased electron-phonon interactions:

$$\sigma \sim \frac{1}{T} \tag{2.19}$$

Semiconductors: In between lies the material class of semiconductors. As with insulators, there is a band gap here, but it is small enough (approx. between 0.1 eV and 6.4 eV) to allow electrons to enter the conduction band at temperatures > 0 K. The location of the bands in this class of material can be altered via a process called doping where impurities are introduced into the solid. Impurities with a higher number of electrons than the primary material lead to a shift of the conduction band towards the Fermi level and result in what is called an n-type semiconductor. Introducing dopants with fewer electrons results in the opposite, a p-type semiconductor with a valence band closer to E_F.
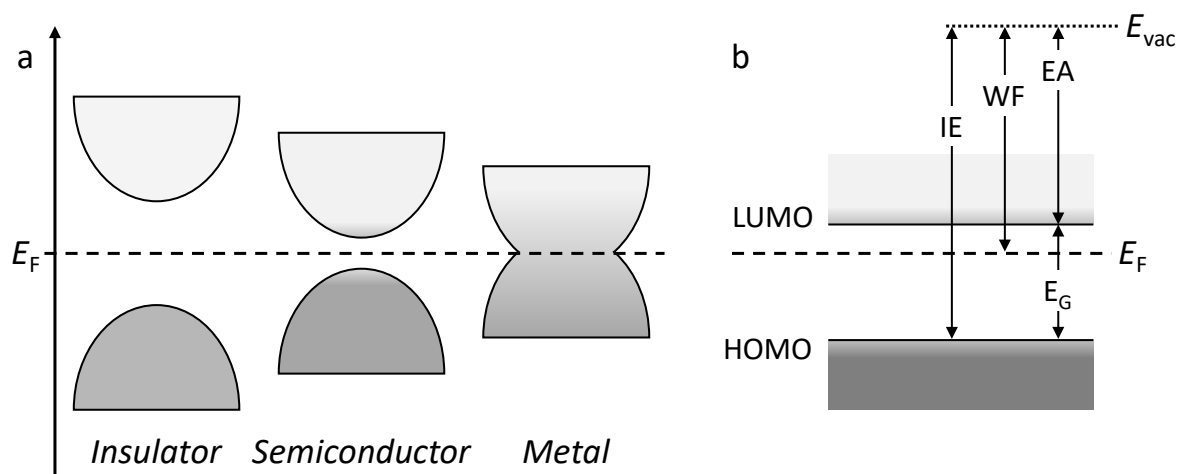
Figure 2.5. Schematic overview of possible band structures. (a) Simplified band structure in relation to the Fermi level of an insulator, semiconductor, and metal. (b) Energy diagram of a semiconductor with important parameters: Fermi Level E_F, vacuum level E_{vac}, electron affinity EA, bandgap E_G, work function WF and ionization energy IE. Modified from [14].

This model is useful for inorganic materials. Now shifting the focus to organic ones, the question arises whether the same concept of band structures can be applied. Molecular orbital theory can also be applied to organic molecules. When carbon atoms form bonds, hybridization of the atomic orbitals results in multiple molecular orbitals.[12]

Considering the most basic example of ethane hybridization, the 2s orbital and the three 2p orbitals form four sp³ orbitals per atom as shown in Figure 2.6. Bonding then happens via the formation of so-called sigma bonds between two sp³ orbitals and between the remaining sp³ orbitals and the 1s orbitals of the hydrogen atoms. Because σ bonds are highly localized, no delocalized charge carriers are available and thus no electric conduction is possible. This applies not only to an ethane molecule but also to longer chains that are merely connected by single bonds.

Introducing double bonds into the chain drastically changes this situation. In ethene, the simplest molecule with a double bond, sp² hybridization occurs resulting in five σ bonds and leaving the two p_z orbitals perpendicular to the sp² orbitals unaltered (see again Figure 2.6). These then combine to form a so-called π bond in which the electrons are delocalized. If more carbon atoms were connected in this way, the π system would spread throughout the molecule, allowing the electrons to move freely. However, the polymerization of ethane opens the double bond, again leaving no loosely bound charge carriers for conduction.

Taking this thought one step further and now considering ethyne, two π bonds are formed via sp¹ hybridization. The polymerization now produces polyethyne (polyacetylene), a polymer in which single and double bonds alternate. This is what is called a conjugated polymer. In this class of materials, the π-system is delocalized over the polymer chain, allowing charge transport, resulting in a conductive polymer. However, due to its high resistivity (~10^8 Ω m) and overall unfavorable material properties, polyacetylene is only seldomly used as a conductive polymer material. [15]

13
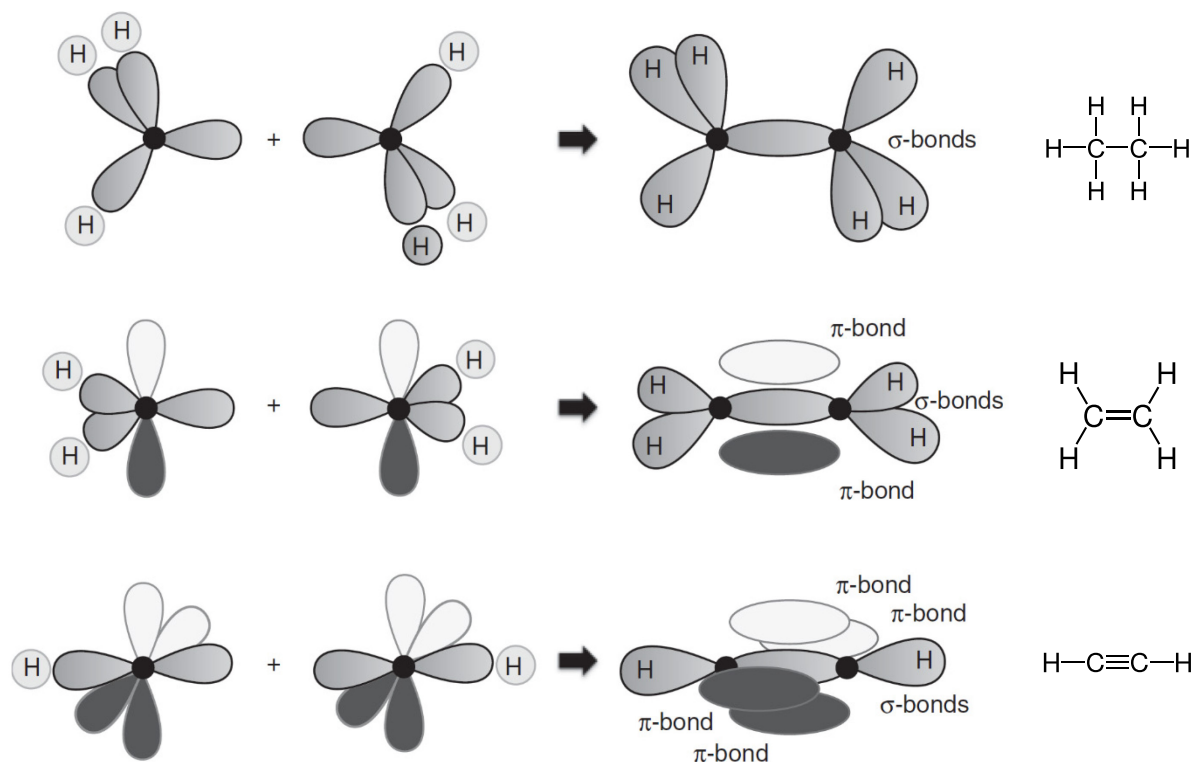
Figure 2.6. Hybridization of ethane, ethene, and ethyne (top to bottom). Molecular orbitals are formed from atomic orbitals. While σ bonds are highly localized, π bonds enable charge carrier transport. Polymerization of ethyne leads to a conjugated, conductive polymer. Modified from [12].

Returning to the concept of band structure, what was called the conduction and valence band can be found here as well. The Fermi level again lies in between occupied and unoccupied states. These are here the highest occupied molecular orbital (HOMO), and the lowest unoccupied molecular orbital (LUMO), also called the frontier orbitals. Their difference in energy is again called the band (or energy) gap. Since the π-electrons are only weakly bound the size of the gap for most organic semiconductors lies typically in the range between 2.0 eV and 3.0 eV which is the range of visible to near ultraviolet (UV) light.[12,16] Therefore, organic semiconductors are suitable for use in optical applications such as organic light-emitting diodes or organic photovoltaic cells. The position of the HOMO and LUMO in materials and consequently the size of the gap is determined by the size of the π system. Increasing its size (meaning increasing the length of the molecule/ polymer) lowers the energy gap. The addition of functional side groups can further shift the levels of the HOMO and LUMO.[17]

A few additional important parameters should be briefly mentioned here since they are of crucial importance when talking about semiconductors (organic or inorganic), metals, or insulators. A graphical representation is shown in Figure 2.5b. The *vacuum level* is the energy level of an electron positioned at rest close (a few nanometers) to the solid surface.[18] The *ionization energy* is the energy necessary to remove an electron from the valence band maximum/ HOMO out of the system. The *electron affinity* is the energy gained by adding an electron from the vacuum level to the conduction band minimum/ LUMO, and the *work function* is the energy required to remove an electron from the Fermi Level, as depicted in Figure 2.5b.[14]

2.2.1 Charge Transport

In the previous section, the transport of charge carriers through the formation of a band structure was described. However, this only partially explains the intramolecular conductance, for a more detailed description of this transport as well as the intermolecular transport other theories have to be applied. The key quantity when talking about transport is the charge carrier mobility μ. This quantity describes how fast a charge carrier can move through a material when dragged by an applied electric field E:

$$\mu = \frac{v_d}{E} \tag{2.20}$$

The quantity v_d is called the drift velocity, the average movement speed of a charge carrier. For inorganic semiconductors, a typical range for the mobility is between 10^6 cm^2 V^{-1} s^{-1} and 10^7 cm^2 V^{-1} s^{-1}.[19] In organic semiconductors, the mobility, even in the optimal case, is multiple orders of magnitude smaller with the best results in literature reaching values of 170 cm^2 V^{-1} s^{-1}.[20]

Band Transport:

In the case of a very large interaction energy between neighboring parts of a molecule or polymer, charge carriers can be described as fully delocalized, and transport happens via a band structure. This can be assumed in molecular crystals at very low temperatures. The mobility of charge carriers μ is then found to vary with temperature T:

$$\mu \propto T^{-n}, \qquad 0 < n < 3 \tag{2.21}$$

As the semiconductor temperature increases, mobility decreases due to scattering interactions of charge carriers with impurities or phonons.[21] The mobility itself can then be described by applying the concept of an effective mass m_{eff} (determined by the strength of the electronic coupling to the neighborhood) and the mean time between scattering events τ:

$$\mu = \frac{q\tau}{m_{eff}} \tag{2.22}$$

In organic semiconductors, band transport can be assumed to be prevalent if the carrier mobility is larger than 5 cm^2 V^{-1} s^{-1}.[22] However, typical values are often several orders of magnitude smaller. Therefore, an alternative transport mechanism has to be assumed.

Hopping Transport:

When the coupling between molecules is weak, the time scale for a charge transfer is very small. This implies that the excited carrier has time to relax back into the ground state and no band transport can take place. Since the charge carrier is now fully localized on a molecule, charge transfer is assumed to occur in jumps between molecules, hence the name hopping transport. Classically (if molecular vibrations are described as harmonic oscillators) this process can then be described by the Marcus theory,[23] where the charge-transfer rate k is given by:

$$k = \frac{2\pi}{\hbar} \frac{J^2}{\sqrt{4\pi\lambda k_B T}} e^{-\frac{\lambda}{4k_B T}} \qquad (2.23)$$

Here, h is the Plank constant and J is the transfer integral (or electronic coupling). λ is the reorganization energy which in the classical Marcus theory describes the energy needed to reorganize the geometry of the initial system to that of the final one. k_B is the Boltzmann constant, and T the temperature. Again, the mobility can be considered as stated in equation (2.22) Noticing that a charge carrier can hop now along multiple molecules, a statistical approach has to be adopted, using the Boltzmann equipartition theorem

$$m_{\text{eff}}\langle v^2 \rangle = n k_B T, \qquad (2.24)$$

where n is the degree of dimensionality and $\langle v^2 \rangle$ the average of the squared charge carrier velocity. It follows then that

$$\mu = \frac{q\langle v^2 \rangle \tau}{n k_B T}. \qquad (2.25)$$

In one dimension this average can be expressed by

$$\langle v^2 \rangle = \frac{k a^2}{2\tau}, \qquad (2.26)$$

with k again the hopping rate, a is the lattice constant, and the factor ½ is a result of the fact that charge carriers can go back and forth on a molecule.[19] The charge carrier mobility can then finally be described as

$$\mu = \frac{q}{k_B T} \frac{k a^2}{2}. \qquad (2.27)$$

Distinguishing between the transport mechanisms

As the last point, it should be briefly discussed how one can be able to distinguish between the two transport mechanisms presented. Since the effective charge carrier mass m_{eff} plays a role in both processes it seems only logical to take a closer look. More specifically, the effective mass to free-electron mass ratio m_{eff}/m_0 can be used to indicate the means of transport. If the ratio is roughly one ($m_{\text{eff}}/m_0 \sim 1$), the effective mass does not differentiate much from the free mass. In this case, charge carriers are said to move "without friction" and band transport theories can be applied.[19] When the ratio is bigger ($m_{\text{eff}}/m_0 \gg 1$), the effective mass is dominating, and charge carriers face much friction. A hopping transport can then be assumed. As a sidenote, there also exists a case where $m_{\text{eff}}/m_0 \sim 0$, observed for extremely high mobility organics such as graphene, indicating that charges are moving in the relativistic limit.[24]

A second way to distinguish between the transport mechanisms is by looking at the ratio of the reorganization energy λ to the coupling energy J. In the case of the ratio being $2J/\lambda \gg 1$, vibrational relaxation of charges is much slower than the transport due to strong intermolecular coupling. The wave function describing a charge carrier is then spread over multiple molecules (or a large part of a polymer) and the transport is band-like.[19] In the other limit where

$2J/\lambda \ll 1$, relaxation happens faster than transport, and charge carriers are localized in their ground state. As described above, transport occurs then via hopping between molecular sites.

2.2.2 Hybrid Systems

Most applications of organic semiconductors do not solely rely on organic materials. Metals can be combined with organics in organic light-emitting diodes (OLEDs), organic solar cells (OSCs), or transistors. This section aims to give a brief description of the effects when metals and organic semiconductors are brought into contact. Keeping in mind the difference between an inorganic and organic semiconductor (conduction band and valence band vs. HOMO and LUMO, see above) the same theory can be applied to both types of semiconductors.

Metal-Semiconductor Junction:

Both organic and inorganic semiconductors, when brought into contact with a metal, form a metal-semiconductor (M-S) junction. Upon contact, the two materials align their Fermi levels and thus charge carriers flow between the metal and semiconductor (due to an electron gradient), from the higher to the lower Fermi level, until equilibrium is reached. This can create an energy barrier, the so-called Schottky barrier Φ_B, described by the Schottky-Mott rule:

$$\Phi_B \approx \Phi_m - EA_s, \tag{2.28}$$

where, Φ_m is the work function of the metal, and EA_s is the electron affinity of the semiconductor. However, the alignment of the vacuum level is not as easy. Interfacial dipoles can form and induce a shift in the vacuum level of up to 1 eV.[25,26] Possible reasons for these dipoles are chemical reactions at the interface, varying electron densities as well as charge transfer at the interface.[25] The interface dipoles can result in the formation of barriers for the injection of electrons or holes (see also Figure 2.7).[12] They can be described by:

$$\chi_e = \Phi_c + \Delta_c - LUMO, \tag{2.29}$$

$$\chi_h = HOMO - \Phi_a - \Delta_a. \tag{2.30}$$

Here, χ_e and χ_h are the barriers for electrons and holes respectively. Φ_c and Φ_a are the work functions of the cathode and anode, and Δ_c and Δ_a are the interface dipoles at either the cathode or anode. From the work functions of the electrodes, another important factor can be derived. The built-in potential Φ_{bi} is the difference between the work functions of the anode and cathode. When operating a device, the voltage applied has to be at least equal to the built-in voltage for charges to be injected (see also Figure 2.11):

$$V_{bi} = \frac{1}{q}(\Phi_a - \Phi_c). \tag{2.31}$$

When a voltage is now applied to the newly formed bilayer device, the flowing current can be either rectified or not.[27] If the barrier is very low, there is no charge carrier depletion zone formed in the semiconductor and the contact is ohmic, meaning that Ohm's law applies:

$$J = \sigma E, \tag{2.32}$$

where J is the current density, σ is the conductivity, and E is the electric field. However, the more interesting case occurs when the barrier is higher. A depletion zone forms near the interface. When only a small voltage is applied, the barrier has a high resistance, and no current can flow. With a larger voltage bias, charge carriers can overcome the barrier since it is lowered by the electric field. Under reverse bias, only a small leakage current is flowing through the junction due to a minimal amount of charge carriers having enough energy to overcome the barrier. Therefore, the junction is rectifying the flowing current.
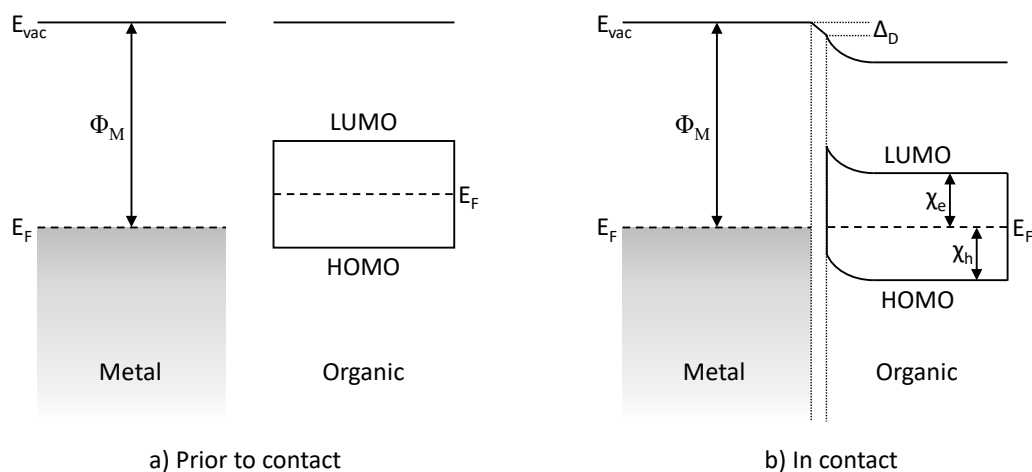
Figure 2.7. Band bending and formation of an interfacial dipole. (a) Prior to contact. (b) After contact band bending aligns the Fermi levels. An interface dipole Δ_D is formed.

2.2.3 Photoexcitation and Excited States

In the last section, the important differences between organic and inorganic semiconductors were described. Another detail in which both groups differ greatly is the coupling between the electrons and the semiconductor lattice i.e., the bound, symmetrical atoms. Therefore, it is crucial to consider the response of the lattice when an additional charge carrier is injected or an existing one is excited to a different energy level. Both actions can be best described as the formation of a quasi-particle.

In the case of injection (or extraction) of an additional charge carrier, the semiconductor lattice is displaced by the charge of the injected particle. In the case of an electron, negative ions in the semiconductor are repelled and positive ones attracted, effectively screening the charge. When the carrier moves through the semiconductor, this "cloud" of polarization moves with it, and both together can be described as a charged quasi-particle named polaron. Exciting a charge carrier results in a quasi-particle called an exciton. It consists of an electron and a hole that are bound by the Coulomb force between them. A hole in this context means a missing electron at a point in an atomic or crystal lattice where an electron could be located. In contrast to the polaron, the exciton is neutral. Excitons can be further classified by their spin. Since both the electron and the hole as fermions have spin $\pm 1/2$, the resulting exciton can have either spin 1 or 0. The Pauli exclusion principle states that particles with the same properties are not

allowed to occupy the same energy level. Therefore, in the state of minimal energy, the electron and hole must have opposite (antiparallel) spins and the net spin of the resulting exciton is zero. However, since the spin also precesses, there are three different higher energy configurations in which the spins are parallel (see Figure 2.8). These are called triplet excitons. The ratio between singlet and triplet excitons is 1:3 which plays an important role in the efficiency of some semiconductor devices, as will be described in more detail in section 2.4.1.
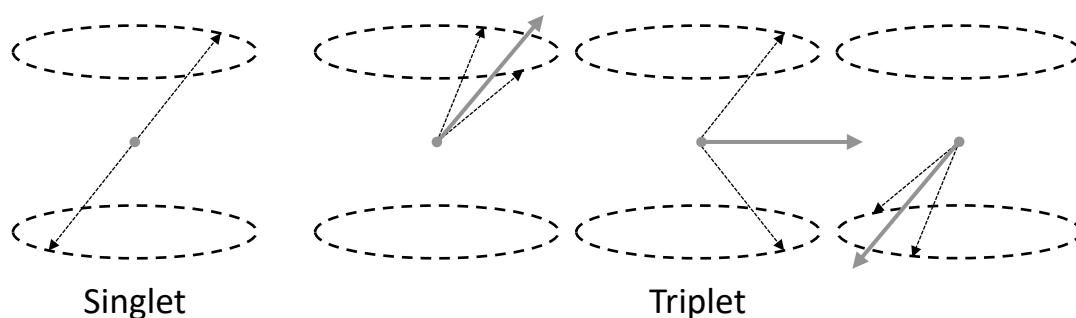
Singlet   **Triplet**

Figure 2.8. Schematic view of singlet and triplet excitons. For the singlet exciton (left) the resulting spin is 0, for the three triplet excitons (right), the resulting spin (thicker gray arrow) is 1.

An overview of the different electronic states and their interactions is displayed in the Jablonski diagram (Figure 2.9). It is important that next to the electronic states, there exists a multitude of additional states with higher energy. The extra energy is stored in vibrational modes. In general, photon emission occurs only from the vibronic ground state of an electronic state (Kasha's rule) because vibronic relaxation is significantly faster than electronic relaxation. Additionally, direct optical excitation into a triplet state is not allowed in quantum mechanics, due to the necessary spin flip (theoretically forbidden, meaning very unlikely). However, it has recently been observed experimentally in inorganic as well as organic materials.[28,29]
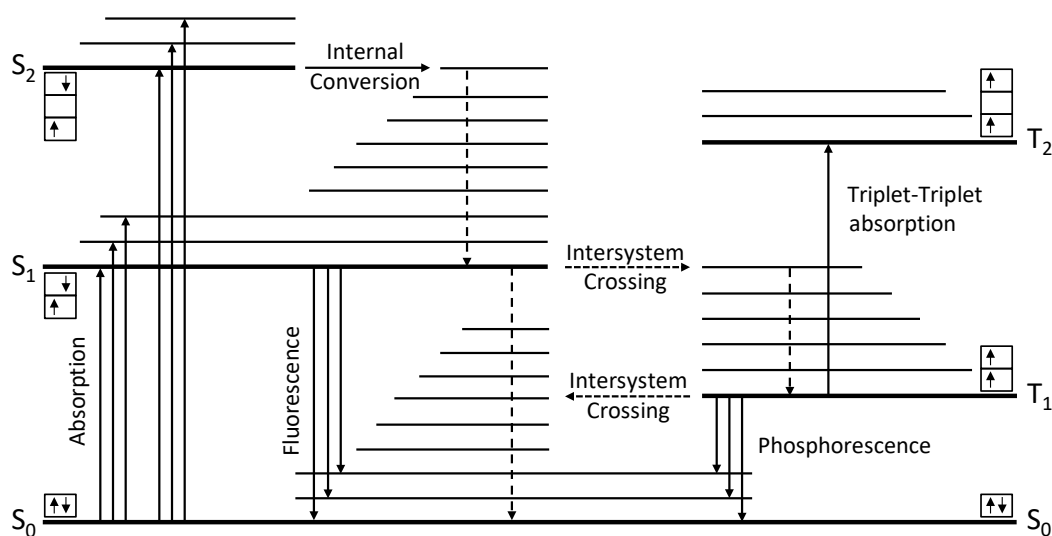
Figure 2.9. Jablonski-diagram. Thick lines represent electronic states, thin lines vibrational ones. Solid arrows indicate absorption or emission of a photon while dashed arrows signify vibrational relaxation.

When a photon is absorbed, the transition to the higher energy state rarely happens to the vibronic ground state. This is due to the fact that the transition is strongly favored if the vibrational wavefunctions of the two states overlap. Since the electron excitation happens on a vastly faster timescale than the movement of the core, it is assumed that the core stays stationery and transitions happen "vertically". The mechanism called the Franck–Condon principle (displayed in Figure 2.10), is responsible for the different intensities of the absorption and fluorescence peaks for a substance. Note, that other transitions are not forbidden but rather very unlikely.

After an exciton is excited into a higher-energy state, there are several dissipative pathways for the excited electron to relax back to the electronic ground state: radiant transitions, where a photon is emitted, and non-radiant transitions. Non-radiative decay occurs through internal conversion through the generation of heat. When a singlet state relaxes by the emission of a photon, the process is called fluorescence. In contrast to the higher singlet states, triplet states cannot be directly excited by the absorption of a photon, but through what is called intersystem crossing where a spin-flip can occur and transfer a singlet to a triplet state. Since the direct return to the singlet ground state by emission of a photon (phosphorescence) is again quantum mechanically forbidden (very unlikely) the lifetime of this excited state is much longer (10^{-6}-10^{+1} s) compared to fluorescence (10^{-10}-10^{-7} s).
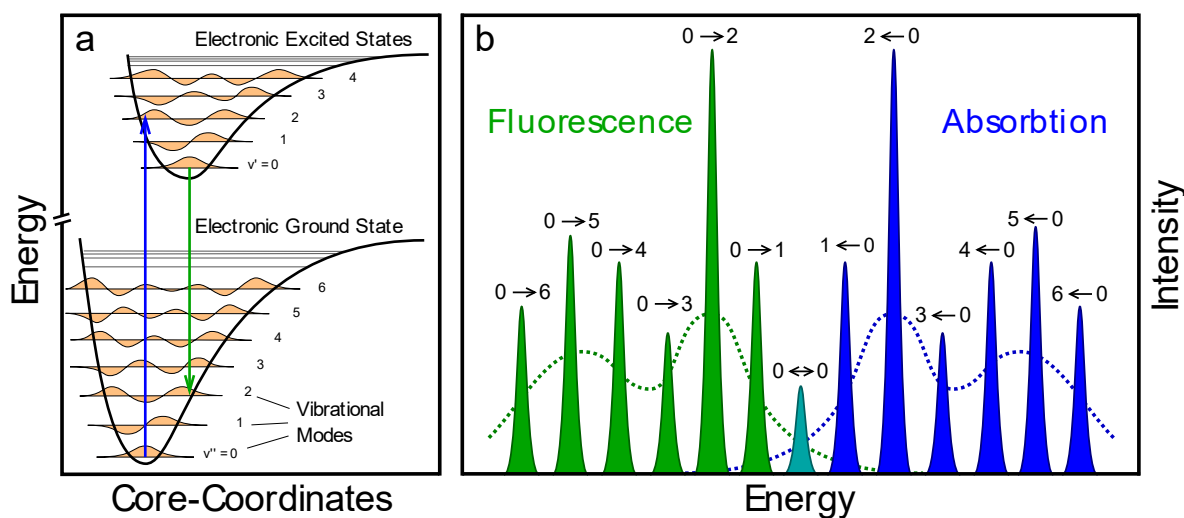
Figure 2.10. Frank-Condon principle. (a) Transitions between states are more likely if the vibrational wavefunctions of the two states overlap. (b) Fluorescence and absorption spectra exhibit different heights of peaks according to the likeliness of the transition. Modified from [30,31].

2.3 Electrodes

The electrodes are a crucial part of any optoelectronic device. Understanding their properties and behavior enables the development of improved materials for higher device efficiency. This section takes a closer look at the important parameters of an electrode. The focus here is on the commonly used metallic electrodes. Finally, options for transparent electrodes are discussed, especially concerning their use in organic devices.

Reflectance, Absorption, and Transmission:

As mentioned in the previous section, the conduction and valence bands overlap in metals. Therefore, electrons are only very loosely bound and can move freely over the entire metal surface. This state is also called electron gas. If the gas is compressed locally (e.g., by an electric field), the Coulomb forces counteract the compression to restore a homogeneous charge distribution. Since electrons have mass and therefore also inertia, the electrons and thus the electron density oscillates with the so-called plasma frequency ω_p:

$$\omega_p = \sqrt{\frac{n_e e^2}{\varepsilon m_e}}. \tag{2.33}$$

Here, n_e is the electron density, e is the elemental charge, ε is the permittivity, and m_e is the electron mass. When the frequency of the incident light is changed, the charge carriers follow the electric field. Up to a frequency equal to ω_p, this is possible and hinders the electric field from entering the metal. However, once the frequency of the incoming light surpasses the plasma frequency, the electrons are too inert, and the light is transmitted through the metal without absorption.

The plasma frequency of typical metals (having an electron density of 10^{28} m^{-3}) is in the range of 10^{15} s^{-1}, resulting in the metal reflecting all visible light but becoming transparent in the higher UV region. In the case that the incident light is absorbed, electrons are excited to a higher state and relax back to the ground state either by re-emitting a photon or by transferring the excess energy to a phonon. The transfer of energy to a phonon is responsible for the absorption of light.

Charge Injection Mechanisms:

For a successful operation of organic devices, charges must be efficiently injected from the electrodes into the organic layers. There are multiple theories describing the mechanisms by which the charge carriers can overcome the potential barrier that exists between the metal and the organic:

If the applied electric field is low, thermionic injection is the prevailing mechanism. Here, charge carriers are thermally excited to overcome the injection barrier. The Richardson-Dushman equation relates the work function Φ of the electrode with the current density of the thermally emitted charges:[32]

$$J_{th} = AT^2 e^{-\frac{\Phi}{k_B T}} \tag{2.34}$$

A is the material-dependent Richardson constant that, according to Dushman,[33] can be expressed as follows:

$$A = b \cdot \frac{4\pi m_e q k_B^2}{h^3}, \tag{2.35}$$

where T is the temperature, k_B is the Boltzmann constant, m_e the electron mass, q the charge, and h is Plank's constant. b is a material-dependent correction factor.

As can be seen from the temperature dependence in equation (2.34), thermionic emission plays a role, especially at elevated temperatures. In organic semiconductors at room temperature, however, a different mechanism prevails.

Initially introduced to explain electron emission from a metallic tip through a triangular barrier into the vacuum, the Fowler-Nordheim tunneling formalism can also be applied to the injection from electrodes into organic semiconductors.[34] In quantum mechanics, charge carriers can be described by a probability wave function, describing the location of the particle. Since this wave function is not extinguished when entering a potential barrier but is only strongly attenuated, charge carriers have a low probability of crossing the barrier, so-called tunneling. In the case of a metal-semiconductor interface, the triangular barrier can be seen as a superposition of the rectangular metal-vacuum barrier and the applied potential.[12] The injected current density can then be described by:

$$J_{\text{FNT}} \cong E^2 e^{-\frac{4\sqrt{2m_{\text{eff}}\Phi^3}}{3\hbar qE}}, \tag{2.36}$$

where E is the applied electric field, and the other values are as previously described. The quadratic dependence of the current density from the applied field is visible when regarding a current-voltage curve of an organic semiconductor device. Thus, tunneling injection plays a crucial role in understanding the current-voltage characteristics of the devices produced in this thesis as seen again in the characteristics of OLEDs in section 2.4.1.

2.3.1 Transparent Electrodes:

Organic light-emitting diodes that emit light and organic solar cells that absorb light share a common design challenge. Both require light to pass through at least one of the device's electrodes to function. Simultaneously, they require good conductance from the electrodes for effective device operation. Combining these two factors is no easy task. However, over the years several solutions have been developed to create simultaneously transparent and conductive electrodes. This section gives an overview of different techniques and their advantages and disadvantages. To quantitatively compare different electrode materials, a figure of merit (FOM) θ_{H} relating the optical transmission T with the electrical sheet resistance R_s was proposed by Haacke in 1976:[35]

$$\Theta_{\text{H}} = \frac{T^{10}}{R_s} \tag{2.37}$$

A higher value of the FOM indicates a better-performing electrode. Note that the FOM is usually denominated with a capital Phi (Φ_{H}). A different symbol has been chosen here to avoid confusion with the aforementioned work function.

Thin Metallic Layers:

As described in the previous section, metals are in general opaque to light in the visible range. Since these are the primary wavelengths at which OLEDs and hybrid solar cells are working, care must be taken when using metallic layers as transparent electrodes. Reducing the thickness of the layer increases the transmission. Therefore, metallic layers of gold, silver, or platinum of only a few nanometers thickness have been successfully used in optoelectronic devices,[36–38] having a FOM of $5.6 \cdot 10^{-4}$ sq Ω^{-1} for gold and $2.9 \cdot 10^{-2}$ sq Ω^{-1} for silver. However, their resistivity increases with decreasing thickness due to grain boundaries and the scattering of electrons at the surface.[39]

The transmission of thin metallic films can be increased drastically when they are sandwiched between two dielectric materials, creating what is called a dielectric-metal-dielectric (DMD) electrode. Incoming light is reflected at the metal surface and this reflected light is then partially reflected again at the interface between the dielectric and the air. Choosing proper values for the refractive indices and thicknesses of the dielectrics makes the reflected waves interfere destructively, and the overall reflection is canceled out. Since the reflection is eradicated, more light needs to be transmitted (see equation (2.9)). DMD electrodes can have good transparency as well as low resistance. A Haacke FOM of $70 \cdot 10^{-2}$ sq Ω^{-1} has been reported. [40,41]

Doped Metal Oxides:

Today's most commonly used material for transparent electrodes is indium tin oxide (ITO). Consisting of indium oxide In_2O_3 doped with tin impurities, it has excellent optical and electrical properties. However, its high brittleness severely limits its range of applications (see chapter 4). The work function of ITO can be increased or lowered by the use of plasma processes or solvents.[42] With a FOM of $1.9 \cdot 10^{-2}$ sq Ω^{-1}, ITO exhibits excellent electrode functions. However, due to the high cost of indium, the research on alternative metal oxides such as fluorine-doped tin oxide (FOM of $1.1 \cdot 10^{-2}$ sq Ω^{-1}) or aluminum-doped zinc oxide (FOM of $6 \cdot 10^{-3}$ sq Ω^{-1}) is on the rise.[42]

Conductive Polymers and Other Materials:

Conductive polymers as described in section 2.2 have been implemented as transparent electrodes as well. Materials such as polyaniline were reported in the literature with a FOM of $2.8 \cdot 10^{-4}$ sq Ω^{-1}.[43] However, the material with the widest use is the polymer Poly(3,4-ethylenedioxythiophene) (PEDOT). To increase its conductivity and solubility in water it is doped with polystyrene sulfonate (PSS) to form PEDOT:PSS.[44] Electrodes fabricated from PEDOT:PSS exhibit a FOM of $6 \cdot 10^{-4}$ sq Ω^{-1}.[42]

Additional materials for transparent electrodes are metal nanowires, carbon materials such as graphene or carbon nanotubes, or thin, (printed) metal grids.[45–48] These are discussed in more detail in chapter 4.

2.4 Optoelectronic Devices

This section is intended as a brief introduction to the working principles of organic light-emitting diodes as well as hybrid solar cells. Their basic characteristics and ideal characterization curves are introduced and discussed.

2.4.1 Organic Light-Emitting Diodes

Brief History:

The development of modern organic light-emitting diodes can be seen as a continuation of the progress in LED research. LED development began in the 1960s when an infrared emitting diode was manufactured at Texas Instruments. Electroluminescence had previously been observed in semiconducting crystals in materials such as gallium arsenide,[49] as well as in organic materials such as acridine orange, for which Bernanose et al. reported electroluminescence as early as 1950.[50] By investigating more complex structures such as doped anthracene crystals, theories of injection and charge transport in organic molecules were developed.[51] However, hampered by the relatively low conductance of organic materials, manufactured devices had to be operated at voltages of 1000 V and more.[52] With the discovery of novel, highly conductive polymer materials, Tang and Van Slyke were able to report the first practical OLED in 1987.[53] The operation voltage was significantly decreased by the introduction of separate materials for the transport of electrons and holes. This configuration confined the exciton recombination (see detailed description below) mostly to the middle of the organic layers.

General Working Principle:

The general working principle of an OLED is relatively simple: from the electrodes, charges are injected into the active materials where they are meant to form an exciton. This exciton then decays radiatively, sending out a photon. Figure 2.11. gives an overview of the four crucial steps in OLED operation:

1. ***Charge carrier injection:*** From the electrodes, charge carriers are injected into the organic materials. For the injection of electrons, materials with a low work function such as calcium ($\Phi_{Ca} = 2.8$ eV) are chosen,[54] while hole injection requires high work function materials. Here a typical choice is molybdenum trioxide ($EA_{MoO_3} = 6.7$ eV).[55] Adding designated injection layers can improve charge carrier injection by modifying the electrode work function (experimental details are given in section 5.1).

2. ***Charge carrier transport:*** The injected charge carriers must now be transported to the emission layer for recombination. Layers responsible for charge carrier transport must have good conductivity for holes or electrons. To prevent charges from passing through the active material without recombination, the work functions of the transporting

materials can be chosen specifically to block unwanted charge carrier transport (see the dashed lines in Figure 2.11). Alternatively, additional blocking layers can be included (experimental details are given in section 6.5).
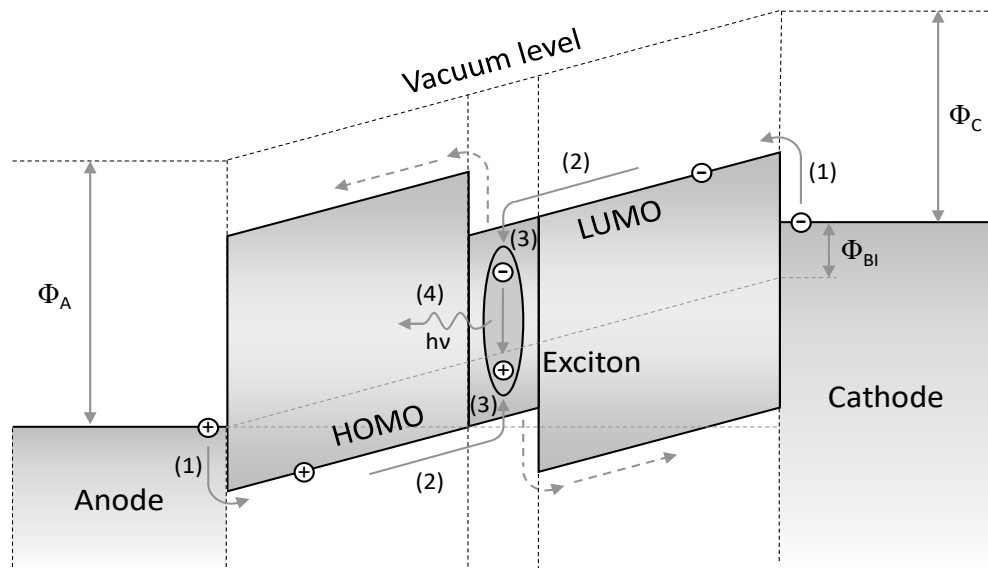

Figure 2.11. Simplified schematic representation of the basic steps of operation in an OLED: (1) Charge injection, (2) charge transport, (3) exciton formation, and (4) radiative exciton decay. The multilayer structure confines exciton formation to the active layer and prevents charges from reaching the opposite electrode without recombination (dashed arrows). Interface effects are not included. Recreated from [56].

3. *Exciton formation:* In the emitter layer, electrons and holes are bound together by the Coulomb force into an exciton. The spins of the electron and hole can thereby be either antiparallel or parallel, resulting in a singlet or triplet exciton respectively. This is of special importance for the OLED quantum efficiency as described below. Blocking layers for electrons and holes can help to confine the exciton formation to the emitter layer. Excitons are often divided into two groups according to their binding energy. A small dielectric constant in a material may lead to excitons with a strong Coulomb interaction and thus high binding energy ($E_b = 0.1 - 1$ eV). The electron-hole distance is very small, and the exciton might be located on one molecule. This type of exciton is called Frenkel exciton. In the case of lower binding energy ($E_b \sim 0.01$ eV) and thus larger exciton radius, they are referred to as Wannier-Mott excitons. Frenkel excitons are the dominating type of excitons in organic semiconductors.[57]

4. *Exciton decay:* Excitons in organic semiconductors have a very short lifetime of only 1-10 ns after which they decay by recombination of the electron and hole. This can happen radiatively by emitting a photon or non-radiatively by vibrational relaxation. In high-performance OLEDs, the emitter oftentimes consists of a guest-host blend. The exciton is formed in the host material and then either transported to the guest material or decays on the host while the released energy is transferred to the guest.[58] Using a phosphorescent emitter, triplet excitons can be harvested as well, significantly increasing the OLED efficiency (see below).

Device Architectures:

OLEDs can be manufactured in a variety of different architectures. As described above, the most basic OLED consists of two electrodes and an emitter layer. However, additional layers are oftentimes included to ameliorate the device's efficacy. In general, OLED types can be divided into two groups, according to their direction of light emission. Top emitting OLEDs emit light through a transparent cathode while having an opaque anode. The opposite is true for bottom emitting devices. While the advantage of top emitting OLEDs is that they can be easily combined with a driver transistor in an active-matrix configuration, finding a suitable transparent cathode material is not an easy task. The commonly used transparent electrode material ITO does not have an appropriate work function. Thus, thin metallic or metal-doped layers are oftentimes employed as transparent cathodes.[59,60] Of course, transparent top and bottom electrodes can be combined to obtain so-called transparent OLEDs.[61] A distinction of OLEDs into different architectures can also be performed by the position of the electrodes. When the anode is the bottom contact and the cathode is the top, the architecture is called regular or standard architecture. In the opposite case, the OLED architecture is referred to as inverted. Figure 2.12 gives an overview of the mentioned OLED types. Inverted architectures have the advantage of not requiring high work function materials such as calcium which is prone to oxidation.[62]
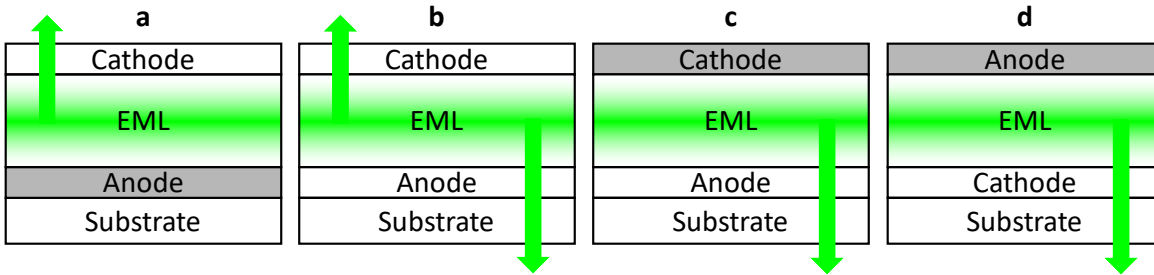
Figure 2.12. Comparison of different OLED architectures. (a) Standard top emitting, (b) standard transparent, (c) standard bottom emitting, (d) and inverted bottom emitting. In every architecture, the simple emission layer (EML) can be supported by injection, transport, and blocking layers.

Loss mechanisms and quantum efficiency:

The explanation above for the different steps of OLED operations illustrates an ideal OLED without any losses. Device performance will be significantly reduced in a real device by multiple loss mechanisms. These can be best described by looking at the so-called external quantum efficiency (EQE). In short, this value describes the ratio of outcoupled photons to injected charge carriers. It consists of multiple constituents:

$$EQE = \eta_{int}\,\eta_{out} = \eta_{rec}\,\eta_{st}\eta_{pl}\eta_{out} \qquad (2.38)$$

In a first approximation, the external quantum efficiency can be described as an internal quantum efficiency η_{int} multiplied by an outcoupling efficiency η_{out}. This can be a major loss factor for OLEDs as it describes the percentage of generated photons that were able to leave the device (in the forward direction).

For conventional OLED architectures, this outcoupling efficiency is in the range of 20 to 50%, meaning that for most OLEDs more than half of the generated light is lost.[63] Internal reflection with subsequent scattering out of the edges of the device due to higher refractive indices of the ITO compared to the glass, reabsorption of emitted photons or non-radiatively decaying excitons are included in this factor.[64] Light extraction can be improved in many ways. A simple roughening of the glass surface, as well as the addition of designated outcoupling structures, have been discussed in literature.[65,66]

The internal efficiency η_{int} can then be described in more detail by further separation into three factors: the probability of charge carrier recombination $\boldsymbol{\eta_{rec}}$, the singlet-triplet ratio of the excitons $\boldsymbol{\eta_{st}}$, and the photoluminescence yield of the employed emitter material $\boldsymbol{\eta_{pl}}$. The first of these factors, η_{rec} is influenced by the charge carrier recombination. For an ideal OLED, it is assumed that all recombination occurs in the middle of the emitter layer. This prevents non-radiative quenching of excited states at the electrodes. However, in real devices, differences in the mobility of holes and electrons can lead to a shift of the recombination zone and thus to a decrease in η_{rec}. Charge carrier balance is another contributing factor. As described above, the injection of carriers should be equal from both electrodes for optimal recombination. By choosing electrodes with suitable work functions and semiconductors with appropriate transport properties, the recombination zone can be centered. The introduction of designated blocking layers can further confine the recombination to the emitter material. Both measures increase the recombination factor η_{rec}.

The next factor η_{st} describes the influence of singlet and triplet generation. Quantum mechanics states that when recombining two species with spin ½ three times more products with spin 1 (the so-called triplet stated) are generated than products with spin 0 (singlet states, see also section 2.2.3). Since in the most common emitter materials radiative triplet decay has an extremely low rate, the singlet excitons are almost exclusively responsible for light emission. This means that 75% of all generated excitons decay without the emission of a photon, thus severely limiting the device's efficiency.

To address this, two novel material classes have been introduced into OLEDs. Phosphorescent emitter materials, such as iridium-containing complexes were first introduced by Forrest et al.[67] The heavy metals included in these materials greatly increase the intersystem crossing, allowing for (indirect) radiative decay from triplet states. By this process, a η_{st} of 100% can be theoretically achieved. However, phosphorescent materials must mainly be used in a guest-host blend since the long lifetime of the triplet states would otherwise make them susceptible to triplet-triplet annihilation. A second way to harvest the triplet excitons are materials, in which the energy difference between the triplet T_1 and singlet S_1 state is small enough for thermally activated transport between them. These materials are aptly named thermally activated delayed fluorescence (TADF) emitters and, like phosphorescent emitters, are capable of harvesting the 75% of triplet excitons generated.[68]

The last parameter, the photoluminescence yield η_{pl} is more difficult to optimize. Since it is an intrinsic parameter of the utilized emitter material, enhancements of the luminescence yield require altering the structure of the employed materials. Again, radiative decay of excited states should be favored, implying that the radiative decay rate must be high compared to the non-radiative decay rate. Therefore, processes such as intersystem crossing must be suppressed. Since this process is mediated by vibrational modes, it can be counteracted by reducing the

molecular vibrations by making the molecule more rigid for example by bridging rings as displayed in Figure 2.13. using the example of biphenyl and fluorene.[69]
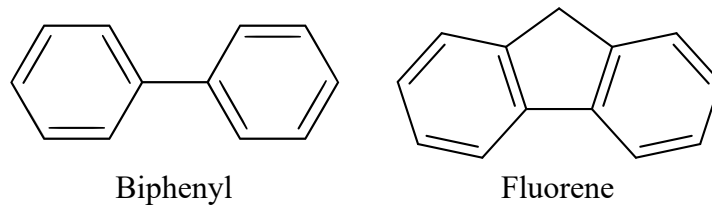
Biphenyl   Fluorene

Figure 2.13. The rigidity of chemical molecules can be increased by bridging rings as shown for biphenyl and fluorene. The improved rigidity reduces vibrational modes and thus increases the photoluminescence yield.

Ideal Electronic Characteristics:

To analyze the function of an OLED, it is common to record the light production and flowing current in a current density-voltage-luminance (JVL) characteristic and plot the current density and luminance against the applied bias voltage. A typical JVL plot for an OLED is displayed in Figure 2.14.
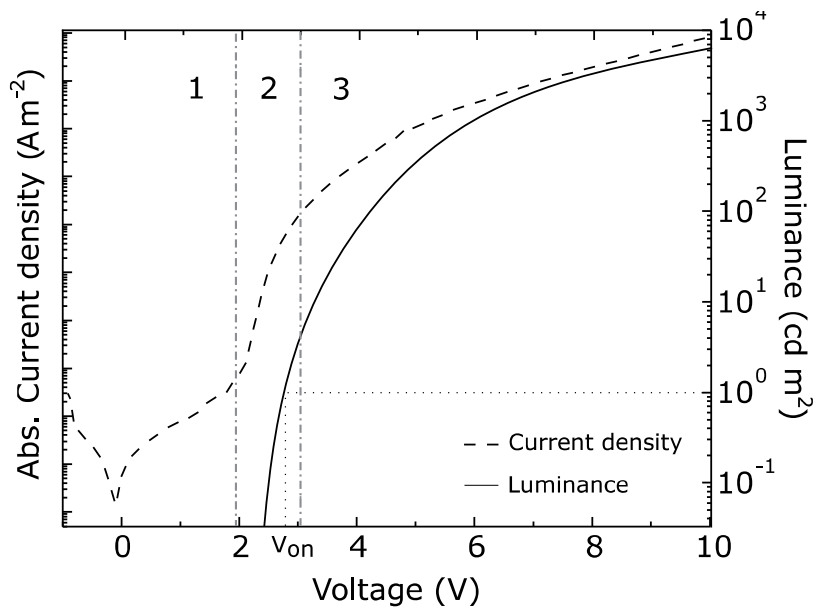
Figure 2.14. Typical JVL curve of an OLED. Three distinct areas are marked. (1) Voltage smaller than built-in potential where no current should flow. (2) Exponentially increasing current for voltages larger than V_{bi}. (3) Current starting to get limited by built-up of space charge. Modified from [70].

In the JVL plot, three distinct regions can be distinguished. When a negative voltage or very small voltage ($V < V_{bi}$) is applied there should be no current flowing. However, due to minor defects such as pinholes a very small leakage current does flow. Since the leakage current is proportional to the applied voltage, it can be described by Ohm's law:

$$J_1 \propto V \tag{2.39}$$

When the applied voltage is increased, the flowing current rises as well. In the region where the voltage is similar to the built-in voltage ($V \approx V_{bi}$), the flowing current is due to a superposition

of a diffusion current away from the electrodes, caused by the gradient of the charge density, and an opposing drift current, due to the actual electric potential gradient.[12] If the diffusion current is dominating, a positive current can be observed. The exponential increase in current can be described in this region by the Shockley equation:

$$J_2 = J_s \left(e^{\frac{qV}{nkT}} - 1 \right)$$ (2.40)

Here, J_s denotes the saturation current density, q is the elemental charge, V is the applied voltage, n is the ideality factor (in this case $n \approx 1.2$ to 2),[71] k is the Boltzmann constant, and T is the temperature.

In the third region, the applied voltage is much larger than the built-in one ($V \gg V_{bi}$). Charge carriers are injected by the electrodes and drift due to the electric field present. The amount of flowing current is merely restricted by the formation of space charges. At reaching a value of 1 cd m^{-2} (this is an arbitrarily defined value, for low-emission materials, it is oftentimes defined as a smaller luminance value) the OLED is considered "on", and the corresponding voltage is called the turn-on voltage (V_{on}). Theoretically, this third region is described by the Mott–Gurney law:

$$J_3 = \frac{9}{8} \varepsilon \mu \frac{(V - V_{bi})^2}{L^3}$$ (2.41)

Where ε is the material permittivity, μ is the combined mobility of electrons and holes, V is the applied voltage and L is the material thickness. The charge carrier mobility can then be extracted from this relation, as will be done in section 5.2.

2.4.2 Solar Cells

In general, organic solar cells can be described as the opposite of OLEDs. The simplest approach is an organic semiconductor between two metal electrodes. Incident light is absorbed in the organic material, and excitons are formed if the light is of energy bigger than the band gap of the active material. The charges are then separated by the electric fields created by the built-in potential of the employed heterojunction materials. As with OLEDs, this approach works but is highly ineffective since the electric field is not strong enough to adequately prevent carrier recombination. Various approaches have been taken to address this problem. Two active layers, one as a donor and one as an acceptor, increase the local electric field so that excitons can be split more efficiently. However, since the splitting is taking place at the interface between donor and acceptor, and since the diffusion length of excitons in organic semiconductors is small (~10 nm) only the area immediately around the heterojunction is effective in splitting excitons and generating unbound charge carriers. Mixing donor and acceptor into a bulk heterojunction can solve this problem. In this type of material, excitons can easily reach an interface and split up. However, if the materials are too finely distributed, the current flow is impeded. Therefore, care must be taken when designing OSC interfaces.

If a solar cell is measured in the dark, the JV curve obtained corresponds exactly to that of a normal diode. At exposure to light, the curve is the resulting superposition of the diode curve and the current generated by the light.[72] That means the curve is shifted into the negative area.

Therefore, the JV characteristics of an OSC can be described by the Shockley diode equation (eq. 2.40) along with an added term J_L describing the light-generated current density:[73]

$$J = J_S \left(e^{\frac{V}{nV_T}} - 1 \right) - J_L \tag{2.42}$$

Here, J_S is the saturation current density (under reverse bias), V the voltage across the cell, and n the ideality factor (n is added to account for an imperfect diode, mainly charge carrier recombination. It is one for an ideal diode and higher for real diodes). V_T denotes the thermal voltage, a value calculated from the elemental charge e and the Boltzmann constant k at a given temperature T:

$$V_T = \frac{kT}{e} \tag{2.43}$$

At room temperature (300 K), the thermal voltage is approximately 26 mV. A typical JV curve of a solar cell is portrayed in Figure 2.15. Important solar cell characteristics are included: The short-circuit current density J_{sc} is the value of the current density at which the voltage is zero, i.e., the cell is short-circuited. V_{oc}, the open-circuit voltage, is the maximum voltage available from the cell, which happens at a current density of zero. It is given by rearranging equation (2.42):

$$V_{oc} = nV_T \ln\left(\frac{J_L}{J_S} + 1 \right) \tag{2.44}$$
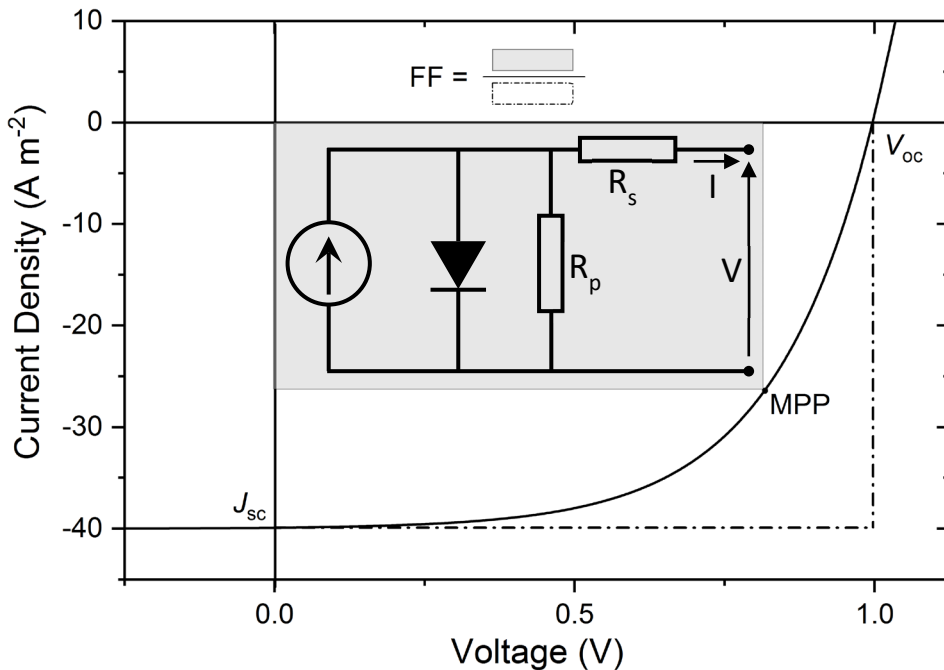

Figure 2.15. Current density-voltage characteristics of a typical OSC. Important parameters such as the open-circuit voltage V_{oc}, the short circuit current density J_{sc}, and the maximum power point *MPP* are marked. The inset shows an equivalent circuit diagram of an OSC including the series and parallel resistances R_s and R_p. Modified from [74,75].

Multiplying the voltage and current gives the power produced by the solar cell. The maximum power point (*MPP)* is the point (voltage/ current) where the cell delivers the maximum output power. It is an important value when calculating the fill factor (FF) of the solar cell, which together with J_{sc} and V_{oc} determines the maximum available power from the OSC. In Figure 2.15. the fill factor is shown as the quotient of the gray rectangle and the dashed one. Calculation of *FF* is done as follows from the current and voltage at *MPP*:

$$FF = \frac{V_{MP}J_{MP}}{V_{oc}J_{sc}} \tag{2.45}$$

The bigger the fill factor is, the more efficient the OSC. Generally, the efficiency can be given by the ratio of input to output power. The efficiency, or in this case power conversion efficiency (*PCE),* can also be described by the product of the *FF* with the J_{sc} and V_{oc}:

$$PCE = \frac{V_{oc}J_{sc}FF}{P_{in}} \tag{2.46}$$

P_{in} is the input power of the cell, under standard experimental conditions (AM1.5, 25 °C) the input power is $1 \, \text{kW m}^{-2}$. AM1.5 describes a standard solar spectrum at sea level through 1.5 atmosphere thickness (corresponding to a solar zenith angle of 48.2°) that is used to test solar cells. This spectrum is appropriate for most solar cell testing in temperate latitudes such as central Europe.[76] Other AM values exist for different latitudes. Testing the cells with a standardized AM spectrum enables the comparison of differently manufactured cells.

Until now an ideal solar cell was assumed. In real cells, however, resistances have to be taken into account. The inset in Figure 2.15. shows an equivalent circuit diagram of an OSC. It can be described as a current source with a parallel diode. Included are also the two main resistances. The series resistance R_s is a result of the contact between the electrodes and the semiconductor as well as the resistances of the electrodes themselves. R_s mainly impacts the fill factor, which is lowered. The parallel (shunt) resistance R_p is mainly caused by defects while manufacturing the OSC. Power losses in the cell are caused by providing an alternative path for the current, bypassing the diode. Equation 2.42 can then be adapted to include these resistances:

$$J = J_S \left(e^{\frac{V - JR_S}{nV_T}} - 1 \right) - J_L + \frac{V - JR_S}{R_p} \tag{2.47}$$

However, it should be noted that this is an implicit function since the current density appears on both sides of the equation. Therefore, numerical solution methods are required.

This theoretical consideration provides the basis for examining the characteristics of the solar cells produced in section 5.2.

3 Experimental Techniques

In this chapter, the theoretical background and the practical applications of the processing and measuring techniques used in this work are briefly described. Solution processing methods are described first, followed by evaporative techniques. In the second part, the characterization methods for optical, electrical, and morphological analysis, as well as the laser structuring setup are illustrated. As multiple setups were custom-built while working on this thesis, namely the EQE, haze, bending, and OLED measuring apparatus, these setups are explained in more detail.

3.1 Sample Preparation

This section describes the various sample preparation techniques used in this work. Plasma treatment, spin coating, doctor blading, inkjet printing, and physical vapor deposition are briefly discussed theoretically as well as practically.

3.1.1 Plasma Treatment

Before coating a surface by any one of the techniques discussed in the next section, it is important to have adequate wetting behavior. This means that the ink or solution in contact with the surface of a substrate forms a homogenous, closed layer rather than being prone to de-wetting, which is the process in which a layer of liquid contracts into a smaller area due to its surface tension. To guarantee this, two factors can be improved via plasma treatment. Firstly, the sample surface is freed from contaminants by the active plasma. Especially when using a reactive gas such as oxygen to generate the plasma, surface contaminants are oxidized by the plasma species into more volatile constituents such as carbon dioxide and water.[77] Then, the vacuum pump of the plasma chamber removes these from the sample. Secondly, the wetting behavior can be improved by activation of the sample surface by plasma treatment. Here, the sample is exposed to an oxygen plasma by which functional groups can be deposited onto the sample surface.[78] Polar groups such as OH groups can drastically improve the surface energy and thus change the wetting and work function of the material through plasma-generated surface dipoles.[79]

For a more detailed description of this topic see section 3.2.6. Plasma treatment can also be used for curing metallic inks as seen in chapter 4. From a purely technical point of view, the sample is placed in a vacuum chamber for plasma treatment. The chamber is evacuated, and a small flow of working gas is applied. Then plasma is generated by a variety of processes such as arc or corona discharge or radio frequencies.

In this work, the wetting behavior is improved by applying a plasma treatment with a Diener Femto plasma system. The sample surface is then ready for further coating steps with a solution processing technique.

3.1.2 Solution Processing

Spin coating: Spin coating is a very basic method to fabricate a thin film. In this process, the samples are rotated at variable speeds. Solutions are dispensed onto the substrate and are then spread over the substrate by the centrifugal force. A distinction must be made between static and dynamic spin coating. In the former, the solution is applied before the sample is rotated, in the latter, the solution is deposited onto a sample that is already rotating. The film thickness achieved through spin coating is theoretically described by a variety of different models, each accounting for different solution properties. The most important seems to be solution viscosity,

its evaporation rate, and angular velocity. According to a model by Chen,[80] the layer thickness h can be calculated as follows:

$$h = k_3 \left(\frac{E\lambda}{C_p}\right)^{\gamma} \eta_0^{\beta} \omega^{\alpha} \tag{3.1}$$

E is the average solvent evaporation rate, and λ denotes the latent heat of evaporation. C_p the solvent's heat capacity, η_0 the solution viscosity, ω the angular spin coating velocity, and k_3, α, β and γ are constants. The exponents α and β were found to be fairly independent of the solvent used, being around 0.29 to 0.39 for β, and around -0.5 for α, while k_3 and γ are strongly depending on the solution used. Solvent volatility, an additional parameter is not considered in this model. However, literature indicates that highly volatile solutions lead to higher film thicknesses.[81] Even though the formula mentioned above can accurately describe what influence the spin coating parameters have on the film thickness, it is not very practical to use. Therefore, a simpler relation between the spin coating speed ω and the film thickness h is oftentimes enough to obtain a film of the correct thickness:

$$h \propto \frac{1}{\sqrt{\omega}} \tag{3.2}$$

Throughout this thesis, this simple approach was used to determine the spin coating speeds. This work uses an Ossila Spincoater with a rotation speed between 1000 and 6000 rpm. Static as well a dynamic spin coating was used. An overview of the steps of a typical spin coating process can be seen in Figure 3.1.
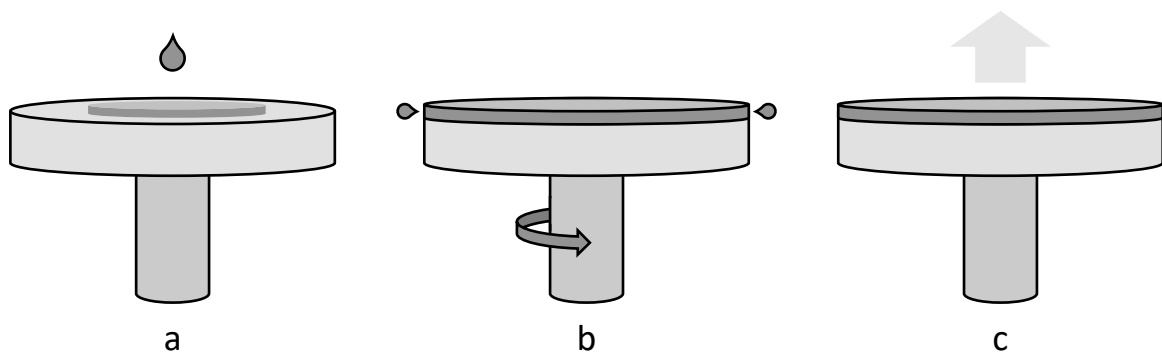
Figure 3.1. Schematic view of the spin coating process. (a) A solution is applied to the sample. (b) Excess solution is removed via rotation. (c) The solvent evaporates to result in a solid film. Sample rotation can be varied or kept constant through all three steps.

When scalability is considered, the process of spin coating faces multiple challenges. Large amounts of solution must be dispensed to fully cover an area, of which only a small part is deposited on the substrate.[82] With polymeric research materials easily reaching prices of 1000 € per gram, this is not a feasible approach. Additionally, the further away from the center a point on the substrate is, the less homogeneous the thin film becomes. For such samples, doctor blading can be used as an alternative method.

Doctor blading: In doctor blading, sometimes also just called blade coating, a thin blade is placed at a short distance over the substrate surface. A small amount of solution is deposited, and the blade is moved over the surface area. The movement of the blade applies a shear force to the solution, spreading it through the gap between the blade and the surface onto the substrate. Heating of the substrate table is commonly applied as well. The thickness of the coated film is dependent on the solvent properties, the table temperature, the gap between the substrate and blade, and the speed of the blade. A model equation for the resulting film thickness (assuming a Newtonian flow) is given by Chou et al. [83]:

$$h = \frac{\alpha \beta h}{2} \frac{\rho_l}{\rho_f} \left[1 + \frac{h^2 \Delta P}{6 \eta v L} \right] \tag{3.3}$$

Here, α and β are correction factors for the side flow and the shrinking of the solution while drying, h is the blade gap, ρ_l and ρ_f are the densities of the liquid and the dried film, ΔP is the liquid pressure head, η the solution viscosity, v the blade speed and L the blade length. While doctor blading requires manual deposition of the solution, slot-die coating automatically dispenses solution through the blade. The rest of the coating process is analogous to doctor blading.

Here a Zehntner ZAA 2300 doctor blade was used with variable speeds between 10 mm and 50 mm s^{-1} and different substrate table temperatures. Figure 3.2 shows a schematic representation of the doctor blading process.
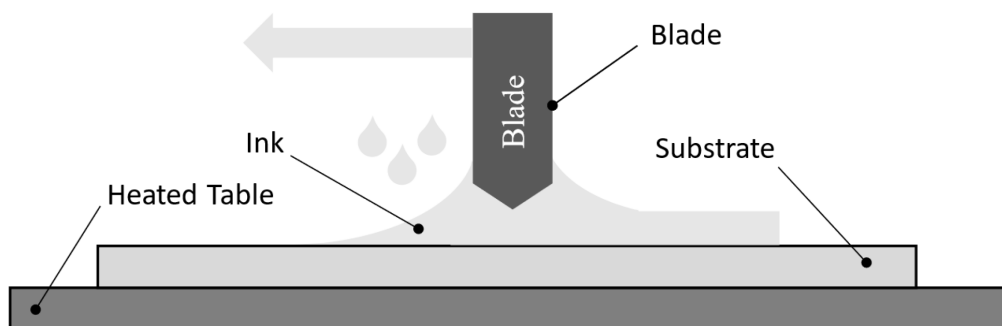
Figure 3.2. Schematic view of the doctor blading process. Ink is spread by a blade onto a substrate and dried by an integrated hotplate. Film thickness depends on the coating speed, ink parameters such as the viscosity or loading, and the table temperature.

Inkjet printing: Though the aforementioned techniques of spin coating and doctor blading are mostly utilized to coat the whole substrate area, partial coverage, even down to single lines or drops is sometimes required. Inkjet printing as a drop-on-demand (DOD) technique can fulfill these requests. Historically, there were two types of inkjet printing, continuous and drop-on-demand printing. Continuous inkjet printers print with a continuous stream of solution (the ink) from a cartridge. The stream then breaks into droplets which are deflected and directed to their target positions by electric fields. While this is a very fast printing technique, it is also very wasteful as the unneeded ink from the continuous stream is discarded.

The other type of printer uses ink cartridges with a variety of different techniques such as piezo actuators, thermal or acoustic actuators, or electrostatic fields to produce small droplets with a drop volume in the range of picolitres.[84,85] After detaching from the nozzle, the shape of the droplet is strongly dependent on viscous forces and surface tension. Inks with lower surface tensions generally result in smaller droplets and therefore allow for higher print resolution on the final substrate.

However, to fully cover larger areas, the droplets must merge on the substrate, requiring a well-adjusted balance between different parameters such as ink viscosity, solvent evaporation, and surface free energy of the substrate.[86] To achieve a higher throughput of material, in commercial inkjet printers, multiple nozzles are used simultaneously. In contrast, so-called single nozzle printers rely on only one nozzle to accomplish printing of extremely fine details.

In this work, a PiXDRO LP50 system from Meyer Burger/Süss Microtec was used in combination with a Spectra S-Class printhead with a nominal drop volume of 30 pl. The printhead utilizes the piezoelectric effect for droplet generation. This means that a voltage, which is applied to the piezoelectric actuator, causes a deformation of the crystal. The deformation creates a pressure wave in the ink which ultimately expels it out of the nozzle opening. A schematic representation of this process is shown in Figure 3.3 Properly adjusting the timing and voltage levels of these pulses is critical, as wrong values can easily result in misaligned drops or the creation of unwanted satellite drops. Thus, optimization of the printhead waveform is essential for every new ink.
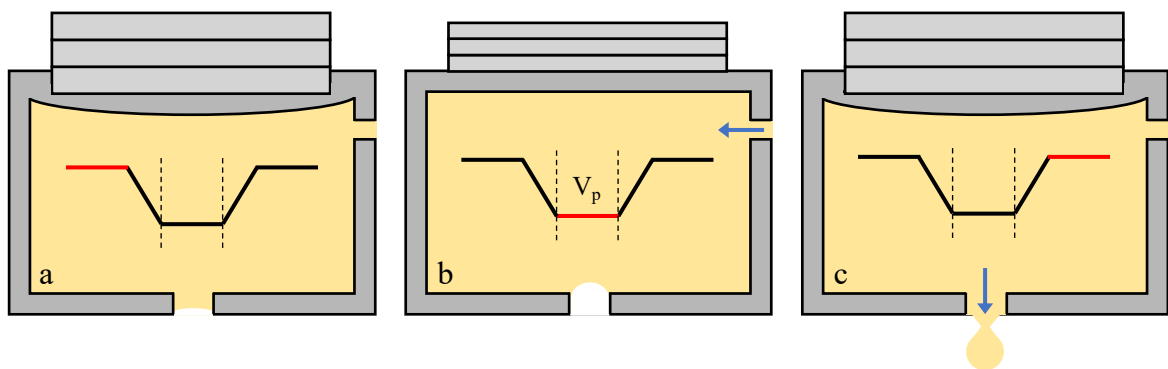
Figure 3.3. Simplified scheme of piezoelectric droplet ejection. (a) The piezo element defines the shape of the ink chamber. (b) When a voltage V_p is applied, the piezo contracts, expanding the chamber, which creates a pressure differential to draw additional ink into the chamber. (c) By returning the piezo and thus the chamber to their original dimensions, the excess ink is ejected as a droplet.

Another important parameter when printing is the viscosity of the ink, which also needs to be carefully adjusted. A viscosity that is too high can prevent proper jetting and clog the printhead, while too low viscosity will cause the ink to run out of the head, dripping the ink uncontrolled onto the sample, or spreading too much on the substrate. By heating the printhead, the viscosity can be adjusted to some extent, but most adjustment is done by additives in the ink. The so-called "magic triangle" of inkjet printing (see Figure 3.4) gives an overview of these print-quality influencing factors.[87] The substrate, ink, and printer are all related to the print quality by different factors which need to be carefully adjusted.

Figure 3.4. The magic triangle of inkjet printing. This shows the simplified influences every element has on the quality of the finished print. Modified from Klug et al.[87]

3.1.3 Physical Vapor Deposition
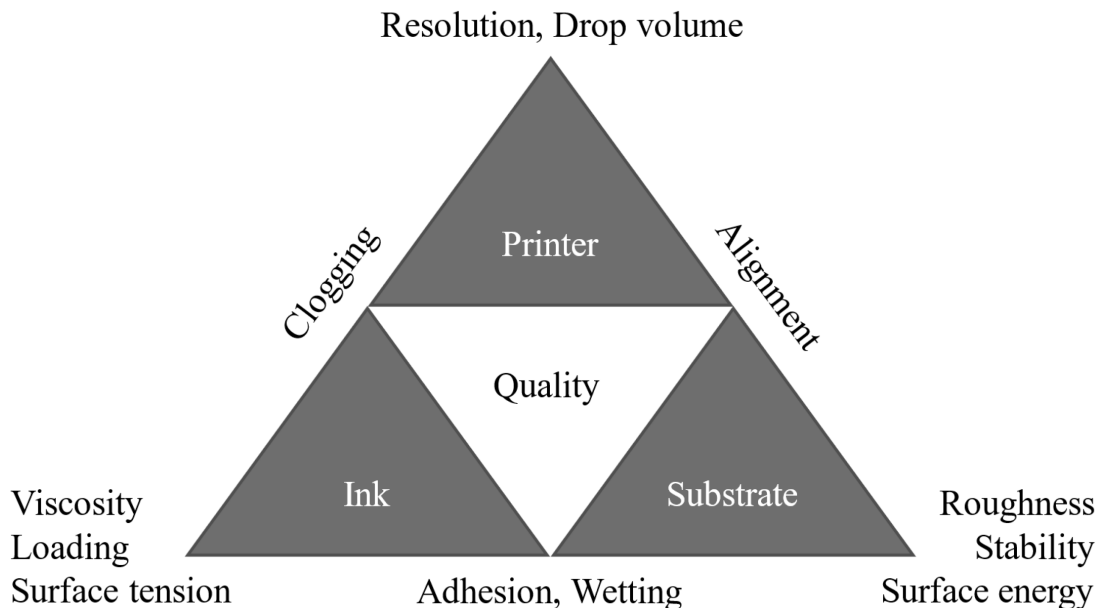
Physical vapor deposition is a group of procedures that use physical processes (in contrast to chemical vapor deposition) to produce thin films from precursor materials such as metals (commonly used are gold, silver, or aluminium) or organic materials. The precursors are vaporized by heating them with a current flow, electron beam, or laser under vacuum. Alternatively, an ion beam can be used in a process called sputtering to eject microscopic particles from the material surface. Vapors then condense on the target surface to form a thin film. For the particles to reach the surface, the process must take place in a vacuum. The important variable here is the mean free path λ of the particles:

$$\lambda = \frac{k_B T}{4\pi p r^2} \tag{3.4}$$

k_B denotes the Boltzmann constant, T the temperature, p the pressure, and r the particle radius. λ needs to be much larger than the distance between the source and target to minimize the possibility of particle collisions. For controlling the thickness of the deposited layer, a quartz microbalance is used in which a quartz crystal vibrates with a set frequency. When materials are deposited on the crystal, its frequency changes. If one compares the altered frequency with that of a pristine reference crystal, the mass of the deposited material and from it, the thickness of the same can be calculated. Günther Sauerbrey demonstrated in the 1950s that there is a linear relationship between the crystal mass and its oscillation frequency when three conditions apply: Firstly, the crystal mass must be large compared to the added mass. Secondly, it is assumed that the added mass is absorbed rigidly onto the crystal and lastly, the additional mass is distributed evenly over the whole active crystal area.[88]

If these conditions are met, the Sauerbrey equation can be applied:

$$\Delta m = -\frac{C}{n}\Delta f \tag{3.5}$$

Δm and *Δf* are the changes in mass and frequency, *n* is the overtone number, and *C* is the mass sensibility, a crystal dependent constant.
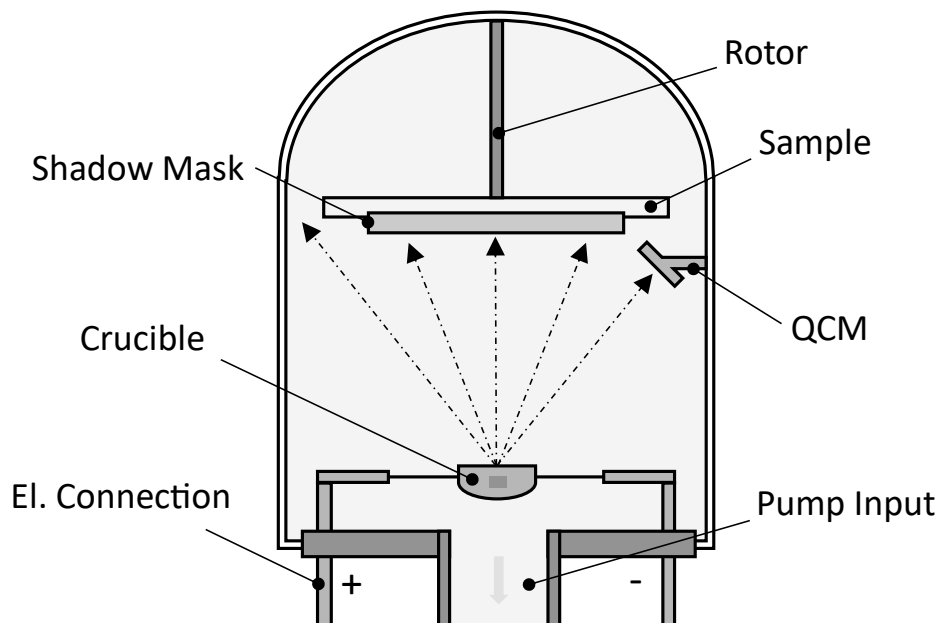
Figure 3.5. Schematic view of a vapor deposition chamber. The whole setup is under vacuum. Metals or organic materials can be placed in the crucible and are thermally evaporated by heating the crucible with an electric current. The thickness of the evaporated film is measured with a quartz crystal microbalance (QCM).

A custom-built vapor deposition chamber was used for all evaporations in this work. Figure 3.5 shows a schematic overview of the evaporation setup.

3.2 Characterization

After samples have been prepared using one or multiple of the above-mentioned procedures, they must be characterized to determine their morphological, optical, or electrical properties. This section aims at giving a brief insight into the applied measurement techniques and their physical background.

3.2.1 Transmission and Emission

UV-Vis spectroscopy: In a very basic sense, light passing through a material can be described as follows: At the surface, a part of the light gets reflected, and another enters the medium. The entering part can further be divided into a part that gets absorbed and the part that successfully passes through the material.

If we consider the reflected part to be negligibly small, the light intensity before and after the sample can be described as an exponential drop:

$$I = I_0 e^{-\alpha d} \qquad (3.6)$$

Here I_0 is the initial and I the final intensity, α the absorption coefficient, a material parameter, and d the film thickness. Solving this equation for the absorption coefficient yields:

$$\alpha = \frac{1}{d} \cdot \ln\left(\frac{I}{I_0}\right) \qquad (3.7)$$

Considering that in optical spectroscopic measurements usually the absorbance A is measured,

$$A = \log_{10} \frac{I}{I_0} \qquad (3.8)$$

and taking into account the base change of the logarithm, it is found that:

$$\alpha = \frac{1}{d} \cdot \frac{\log_{10}\left(\frac{I}{I_0}\right)}{\log_{10}(e)} \approx 2.3 \cdot \frac{A}{d} \qquad (3.9)$$

When measuring using UV-Vis instruments, usually the transmission T of light is measured. The absorbance can subsequently be calculated from the transmission (in percent):

$$A = 2 - \log_{10} T_{\%} \qquad (3.10)$$

From the UV-Vis measurements, the optical bandgap of a material can be estimated. For organic semiconductors, it is oftentimes sufficient to use the onset of the absorption curve as the value for the optical gap, while for metals and metallic semiconductors a Tauc plot can be used.[89] In this method developed by Jan Tauc, the optical bandgap is derived from the absorption coefficient and absorbance spectrum of a material. Plotting $(\alpha h v)^{1/r}$, where h is Plank's constant and v the photon frequency, to different powers against the photon energy hv and extrapolating the linear regime to the x-axis yields the bandgap energy of the material. The exponent r accounts for different transition types: $r = 1/2$ indicates a direct allowed transition bandgap, $r = 2/3$ a direct forbidden gap, $r = 2$ an indirect allowed one, and $r = 3$ an indirect forbidden transition.[90]

In this work, a Perkin Elmer Lambda 950 double-beam spectrometer is used. The advantage of this instrument is that it simultaneously measures the transmission of a sample and a blank, thereby automatically correcting for the influence of the sample substrate. The incident light, from a white light source such as a halogen or deuterium lamp, is dispersed by a prism or grating and sent through the sample and reference. The transmitted light is then measured and displayed.

Infrared spectroscopy: While UV-Vis spectroscopy uses UV and visible light to investigate a sample, infrared (IR) spectroscopy uses IR light. This light does not possess enough energy to excite electrons to higher states. However, molecular vibrations can be excited by the absorption of infrared light. Since these vibrations are specific to functional groups of molecules, their presence or absence can be determined via the IR spectrum.[91]

Fourier-transformed infrared spectroscopy (FTIR) is an alternative IR spectroscopy method. Instead of shining a monochromatic beam of light onto a sample, an interferometer produces a multi-frequency beam, which is directed onto the sample. This measurement is repeated with different frequency compositions to obtain multiple data points. In the last step, the absorption spectrum is calculated from the so-called interferogram using Fourier transformation.

Photoluminescence: As previously described, when light passes through a medium a portion of it is transmitted, and some is absorbed. While the transmitted part can be analyzed via UV-Vis measurements, photoluminescence deals with the part of the light that gets absorbed. This light is interacting with the material, inducing excited electronic states due to the absorptions of photons. Excited states decay quickly either radiatively by emitting a photon with less energy than the incident one or non-radiatively via vibrational relaxation. Like in UV-Vis, light from a white light source is split by a diffraction grating and sent onto the sample. Two different kinds of spectra can be measured: emission and excitation spectra. Emission spectra are measured by exciting a material with light of a fixed wavelength. A spectral region is then scanned, and the intensity of the emitted light is recorded. To measure excitation spectra, the detector is kept at a fixed wavelength while simultaneously varying the wavelength of the excitation light. Again, the intensity of the emitted light is recorded.

For excitation and emission measurements, Edinburgh Instruments fluorescence spectrometers (FLS980 and FS5) were used.

3.2.2 Energy Level and Element Determination

There are multiple techniques to determine energy levels or the elemental composition of materials. All photoemission spectroscopy techniques described in this section are based on the fundamental principle of the photoelectric effect. This effect describes that materials exposed to electromagnetic radiation such as light or X-rays emit electrons. Using Planck's theory of quantized radiation, Albert Einstein showed that the frequency of the incident radiation, not intensity, is the key factor in releasing electrons from a material. [92] To release an electron, the energy of the incident radiation has to exceed the binding energy of the electron, which corresponds to the work function of the material. If the incoming radiation has excess energy compared to the work function, this energy can be transferred to the electron as kinetic energy resulting in the following relation:

$$E_{kin}^{max} = hf - \Phi \qquad (3.11)$$

E_{kin} is the maximum kinetic energy of the outcoming electron, h is Planck's constant, f is the frequency of the incoming radiation, and Φ the material work function. The following techniques are used in this work:

Photoelectron yield spectroscopy (PYS): By using photoelectron yield spectroscopy, the work function of a material can be determined. To give a more detailed description, PYS measures the ionization energy of a sample (as a reminder, for metals this is equal to the work function, see section 2.2). A sample under ambient conditions is exposed to UV radiation of varying energy. The photoelectrons generated are accelerated towards the detector by an electric field, where they trigger an electron avalanche in the surrounding gas. These secondary electrons are then counted by the detector. This co-called open counter was invented in 1979 by Uda and Kirihata.[93] After the counting, another electric field quenches the avalanche, while a second field prevents electrons and ions from the avalanche from contaminating the sample. A linear fit of the photon energy via the detected counting rate yields the ionization potential.

In this work, an AC2 photoelectron yield spectrometer by Riken Keiki is used with incident photon energies between 4.2 eV and 6.2 eV.

UV photoemission spectroscopy (UPS): UV photoemission spectroscopy works on a similar principle to PYS. UV light with higher incident energy than PYS is used to generate photoelectrons from a sample. Since, in contrast to PYS, UPS works under vacuum, these electrons are then directly examined by an energy analyzer. Compared to XPS, explained in the next paragraph, UPS has lower energies and is limited to probing the energy levels of valence electrons. Since UPS detectors have a very high energy resolution, even the fine structure of materials can be investigated. However, the short penetration depth of UV light makes UPS particularly surface sensitive.[94] By probing the onset of the kinetic energy of the electrons in a UPS spectrum, the valence band onset of the probed material can be determined. Furthermore, the work function can be determined from the secondary electron cut-off.[95]

X-ray photoelectron spectroscopy (XPS): In contrast to UPS, X-ray photoelectron spectroscopy uses X-rays as incident radiation to investigate the sample. This means that with its higher energies in the range of 200 eV to 2 keV, core levels of the atoms in the sample are probed, making this technique highly element sensitive. All elements except hydrogen and helium, which have a too-small scattering cross-section, can be identified by XPS. Electrons in the sample absorb the X-rays and leave the sample. Their energy is characteristic of a particular atomic orbital, allowing the elemental composition of the sample to be determined. Since the local bonding environment also affects electron energies, chemical states can be probed by XPS as well.[96,97]

On their way to the surface, the core electrons can excite and release additional electrons leading to a broad background in the XPS spectrum. This has to be taken into account while analyzing the data. Furthermore, positive charge accumulation on non-conductive samples due to electrons being emitted must be prevented as well. The charge buildup can lead to a shift or

distortions in the XPS spectrum.[98] Grounding the sample (with sufficient conductivity) or other compensation can be applied to alleviate this problem.

For all UPS and XPS measurements in this work, a JEOL JPS 9030 photoelectron spectrometer system was used. The UV excitation source, using the Lyman α line was controlled by an Excitech E-lux EPU unit within the JEOL system.

3.2.3 Morphology

Surface morphology can be investigated by a variety of different contact or non-contact techniques. In this work, the following was used:

Confocal laser scanning microscopy: With this technique, the surface morphology as well as the sample roughness can be analyzed. Optical images of the surface can be taken over a large area via an image stitching algorithm. With confocal laser scanning, the thickness of surface structures can be assessed by rastering the surface and taking laser scans at different focus depths. A pinhole in the instrument ensures that of the reflected light only the part in focus can reach the detector. When analyzing a film's thickness, the film has to be scratched first to obtain depth data.

A LEXT OLS4100 laser scanning microscope from Olympus was used in this work. It has a magnification of up to 100x and a Z resolution of 10 nm.

Profilometry: With profilometry, the surface of a sample can be analyzed in terms of roughness and curvature. There are contact and as non-contact profilometers. In the contact one used here, a stylus is dragged over the sample surface and its vertical displacement is measured as a function of position. Care must be taken to select an appropriate tracking force to not scratch the sample while measuring. Again, for measuring the film thickness, a scratch is made through the film.

A DektakXT stylus profiler from Bruker was used for the experiments in this thesis.

Scanning force microscopy: Sometimes also known as atomic force microscopy, scanning force microscopy (SFM) uses a cantilever with an extremely fine tip to record interactions with a sample surface. When being rastered over the surface area in very close proximity, interactions such as mechanical contact forces or van der Waals forces deflect the cantilever.[99] This deformation is measured by reflecting a laser from the cantilever onto a segmented photodiode, making even minimal movements visible. According to the feedback from this measurement, a constant force between the tip and the surface can be retained.

Multiple measurement modes are possible for SFM. In contact mode, the tip of the cantilever is in physical contact with the sample surface. The tip is dragged along the surface contour and the cantilever position is directly measured and displayed as a height profile. When measuring

in non-contact mode, the cantilever is oscillated at or sometimes slightly above its resonant frequency. Surface forces that attract or repel the tip influence the recorded oscillation frequency. Since this frequency can be recorded with extremely high precision, the non-contact mode was the first mode to achieve atomic resolution.[100] In between the two aforementioned modes is the so-called dynamic contact or tapping mode. Here the cantilever oscillates near its resonance frequency and only intermittently comes into close contact with the sample surface. This alleviates lateral forces acting between the tip and the sample.[101] The change in cantilever frequency is used for motion feedback, where a controller attempts to keep the oscillation amplitude constant. An image in this mode is a recording of the force of intermittent contacts between the tip and sample.[102] Next to the measuring modes relying on contact forces, there is a multitude of different techniques combining SFM with magnetic microscopy,[103] chemical force,[104] Kelvin probe measurements,[105] and much more.

To measure SFM a Bruker FastScan SFM in tapping mode was used for this work.

3.2.4 Thermal analysis

Thermal analysis is a set of measurement techniques that study material properties as temperature changes. There are a variety of different techniques, two of which are used here:

Differential scanning calorimetry (DSC): In differential scanning calorimetry, the material to be analyzed is placed in a crucible. The crucible is positioned in a calorimeter along with an empty reference one. Here heat-flux DSC is used, where the change in heat flow is recorded while the sample is heated. When a material undergoes a phase transition a different amount of heat is required to keep the sample at the same temperature as the reference.[106] The comparison of the heat flow between the sample and the reference enables the amount of heat required for the transition to be determined.[107]

Thermogravimetric analysis (TGA): TGA is a technique where the sample mass is recorded while it is heated. Similar to DSC, the material is placed in a crucible and is heated in an oven along with a reference. Heating can take place under different atmospheric conditions such as in a vacuum or under inert gases. This technique is used to study the thermal stability of a material. A decomposition is visible as a mass loss in the resulting graph.[108] There are multiple measurement modes. Mass can be tracked over time at constant temperatures (static thermogravimetry), at stepwise increasing temperatures (quasistatic thermogravimetry), or a linear temperature change (dynamic thermogravimetry). TGA can be combined with other measurement techniques to further study material degradation.[109]

3.2.5 Sheet Resistance

When fabricating a thin film of conducting material, it is necessary to measure its resistance. However, measuring with just a multimeter can be inaccurate since the measured resistance

would be dependent on the measuring length. Since in contrast to that, the sheet resistance is invariable under scaling of the film size, it can be used to directly compare films of different dimensions and geometries. Sheet resistance can be measured via a 4-point probe. This instrument has four equally spaced probes. Through the outermost probes, a current is injected into the sample. A voltage meter is connected between the inner probes. Since a voltmeter has very high resistance, no current flows through the inner probes and therefore the wire resistances do not contribute to the measurement. The drop in voltage between the inner probes is therefore only caused by the sample resistance. From the voltage drop ΔV and the applied current I the sheet resistance can be calculated:

$$R_{sh} = \frac{\pi}{\ln(2)} \frac{\Delta V}{I} \tag{3.12}$$

However, it must be taken into account that this equation is a simplification that is only applicable if a) the material thickness tested is not thicker than 40% of the probe spacing and b) the sample size is significantly larger (preferably said to be at least 40 times) than the probe spacing. If this is not the case, correction factors must be applied.[110]

In this work, a Jandel 4-point probe with a tip-to-tip distance of 1 mm and a tip radius of 100 μm is used.

3.2.6 Surface Free Energy and Wetting Behavior

When fabricating a sample by solution processing, the ink and the surface of the substrate must be matched. Not every ink can wet every surface. The so-called wetting behavior describes the interaction between the ink and a surface. Good wetting means that the ink can coat the surface well. This also implies a low contact angle (the angle between a drop of liquid and the surface). In general, an ink is considered to wet a surface if the contact angle is between 0° and 90° and non-wetting for contact angles above 90° (see Figure 3.6).[111] Most solution processing methods have the aim of fully covering a sample and thus low wetting is preferable. When fabricating well-defined structures, a delicate balance must be found, since high wetting comes with the drawback of lower possible resolution (for example in inkjet printing). Thin lines, for example, cannot be produced with ink that wets a surface too well.

Good wetting is caused by a low surface tension of the ink and a high surface free energy of the substrate. While the surface tension of a liquid can be measured directly by multiple techniques, the surface free energy must be calculated. It can be determined by measuring the contact angle of a drop of ink on a surface. Using Young's equation,[112] the surface free energy σ_s can be calculated from the contact angle θ:

$$\sigma_s = \sigma_{sl} + \sigma_l \cdot \cos\theta \tag{3.13}$$

σ_{sl} is the interfacial tension between the liquid and solid and σ_l is the surface tension of the ink. Since the contact angle is measured with fluids of known surface tension, the additional unknown variable σ_{sl} has to be determined. This can be done via a variety of methods but the most commonly used is the Owens, Wendt, Rabel, and Kaelble (OWRK) method.[113–115] Each surface tension can be described as having a polar and a dispersive part:

$$\sigma_l = \sigma_l^d + \sigma_l^p \tag{3.14}$$

This is used in the OWRK model, where the interfacial tension is calculated using two liquids with known surface tension (polar, as well as dispersive part. At least one liquid must have a polar part > 0):

$$\sigma_{sl} = \sigma_s + \sigma_l - W_A \tag{3.15}$$

where the adhesion work W_A is calculated as follows:

$$W_A = 2\left(\sqrt{\sigma_s^d \cdot \sigma_l^d} + \sqrt{\sigma_s^p \cdot \sigma_l^p}\right) \tag{3.16}$$

In combination with equation (3.13), the surface free energy can then be calculated.
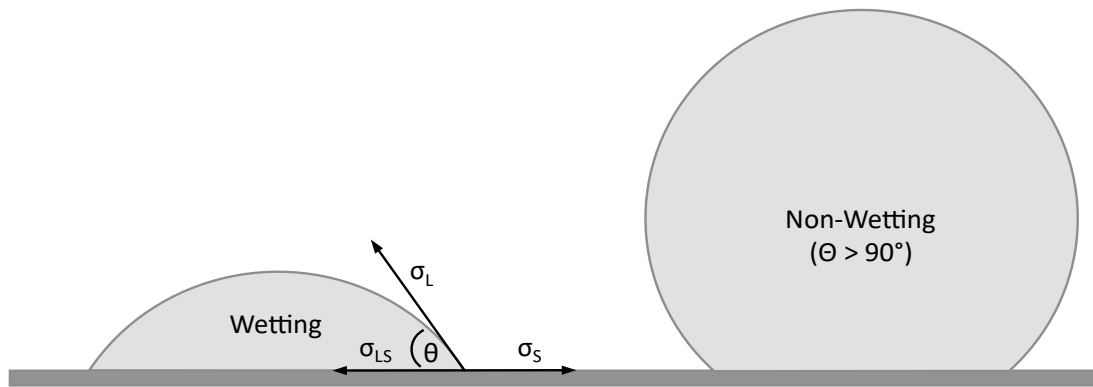

Figure 3.6. Schematic view of a wetting and a non-wetting drop of liquid on a solid surface. Also shown is the relation between the surface free energy σ_s, the surface tension of the liquid σ_l, the interfacial tension between the liquid and solid σ_{ls}, and the contact angle θ.

When having a large batch of different substrates, it is oftentimes not feasible to measure the contact angle for every new ink. The so-called wetting envelope can be used to determine the contact angle on a specific surface without actually measuring it.[116] To do this, the polar and the dispersive components of the inks must be known. Then, the Young-Dupré equation for the adhesion work W_A can be used:[117]

$$W_A = \sigma_l(1 + cos\theta) \tag{3.17}$$

Where a solution is considered to fully wet a surface if $\cos\theta = 1$. Combining equations (3.14), (3.16), and (3.17) yields:

$$\sigma_l^d + \sigma_l^p = \sqrt{\sigma_s^d \cdot \sigma_l^d} + \sqrt{\sigma_s^p \cdot \sigma_l^p} \tag{3.18}$$

If now a wetting parameter R is defined,

$$R = \sqrt{\left(\sigma_l^d\right)^2 + \left(\sigma_l^p\right)^2} \tag{3.19}$$

meaning that

$$R \cdot \cos \varphi = \sigma_l^d \text{ and } R \cdot \sin \varphi = \sigma_l^p \,. \tag{3.20}$$

By inserting (3.20) in (3.18), the wetting envelope can then be displayed in a polar coordinate system, evaluated for $\varphi = 0\text{-}90°$ as follows:

$$R(\varphi) = \left(\frac{\sqrt{\cos \varphi \cdot \sigma_S^d} + \sqrt{\sin \varphi \cdot \sigma_s^p}}{\cos \varphi + \sin \varphi} \right)^2 \tag{3.21}$$

Now, if an ink with known polar and dispersive parts lies inside the wetting envelope, it is considered to wet the surface. The wetting behavior of a surface can be altered by a variety of techniques such as the plasma treatment described in section 3.1.1.

In this work, a DSA100 Drop Shape Analyzer from Krüss was used to determine surface free energies.

3.2.7 Charge Carrier Mobility

The efficiency of electronic devices strongly is strongly dependent on the properties of the employed materials. One such important property is the ability of a material to conduct charge carriers. This property is quantified by what is called charge carrier mobility. For most organic semiconductors, the mobility for one type of charge carrier (electron or hole) is much higher than for the other. Experimentally, the charge carrier mobility can be determined from so-called single-carrier devices. In these components, the layer to be analyzed sits between layers with high conductivity for the charge carrier (e.g. PEDOT:PSS and MoO_3 for holes). Current-voltage curves are recorded and assuming a space charge limited current, the Mott-Gurney law can be applied to evaluate the carrier mobility (see also section 2.4.1):[118]

$$J = \frac{9}{8} \varepsilon \mu \frac{V^2}{L^3}$$

Here, J is the current density, ε the permittivity of the material, μ the carrier mobility, V is the applied bias voltage, and L is the material thickness. Through a linearized fit, the carrier mobility can then be calculated. However, caution has to be taken when the layer has possible defects as the Mott-Gurney law assumes trap-free current flow.[119]

3.2.8 Haze

Parts of this section have been previously published.[120] Additional data has been included.

A guide to qualitative haze measurements demonstrated on inkjet-printed silver electrodes for flexible OLEDs

F. Hermerschmidt, M. Hengge, V.R.F. Schröder, P. Hänsch, K. Livanov, N. Zamoshchik, and E.J.W. List-Kratochvil

Proc. SPIE 11808, Organic and Hybrid Light Emitting Materials and Devices XXV, 118080B (9 August 2021); doi:10.1117/12.2594486

When light passes through a transparent medium, it can be scattered. This can be caused by contaminants in the thin film such as particles and air bubbles, or surface irregularities. If the incident ray is scattered by less than 2.5° from the normal of the light source, this is called clarity, if it is scattered by more than 2.5° it is called haze. A high haze can be desirable, for example in the case of lighting applications, where utilization of high haze materials results in a softer, more uniform light. In contrast, in display applications, low haze materials are required to enable clear, sharp images for the viewer. Measurement of haze is performed according to the ASTM D1003 or BS EN ISO 12468 standard using either a spectrophotometer or a dedicated haze meter.[121,122] Both methods measure the transmittance haze T_H as well as the total transmittance T. The haze H is then calculated by the ratio:

$$H = \frac{T_H}{T}$$

(3.22)

When using a spectrophotometer, four measurements are necessary to obtain the haze of a sample. A spectrum with a white standard at the exit of an integrating sphere, blocking the light output, has to be measured first. Then, the sample is added while keeping the standard. These two measurements are then repeated without the white standard. Calculation of the haze can then be performed by integrating the four measurements.[123]

A hazemeter considerably simplifies this measurement due to the inclusion of a ring detector in its integrating sphere that detects the deviation of the light from its normal path of incidence.[124] A schematic view of this measuring instrument is displayed in Figure 3.7. Although these instruments offer a precise quantification of the haze of a substrate, it is oftentimes not necessary to determine the absolute haze value. Even the qualitative analysis of the haze of a sample can be of great value. Therefore, a setup to qualitatively investigate the haze of samples made from readily available laboratory materials can be very advantageous. From this, it can be determined if a sample has lower or higher haze compared to a reference, for example comparing a printed layer to the pure substrate as shown below.
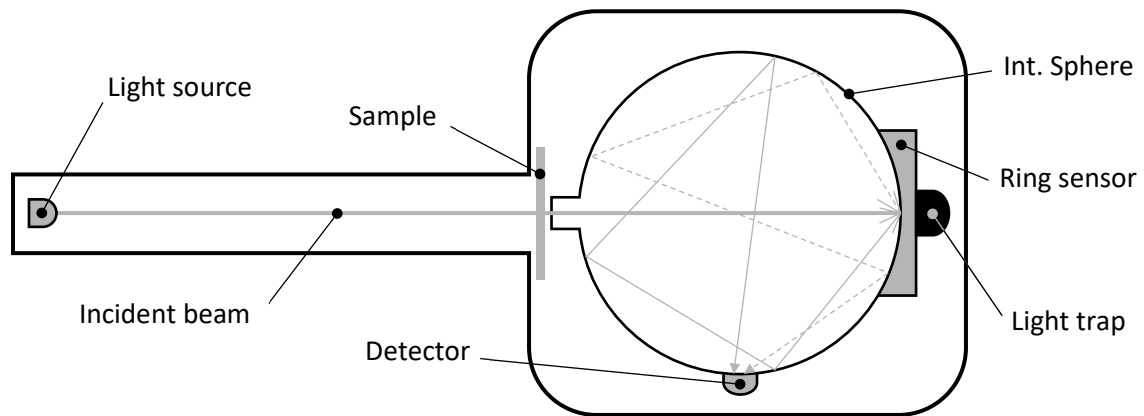
Figure 3.7. Schematic representation of a hazemeter. Through a sample, the incident light is sent into an integrating sphere where a ring sensor detects light deviation and a detector the light intensity

In commercial setups, the light source is normally a filtered white light source that is employed in combination with an integrating sphere. However, it was suspected that a simpler setup with a laser pointer as the light could be used. Instead of utilizing a ring detector to measure the deviation of the incident beam a simple printed sighting disc was used. Figure 3.8 shows a photograph of the full setup. A laser pointer is aimed at a sample at a distance of 1 cm using metal clamps. The scattered light was then projected onto the target 1 m away. With the camera being fixed on a tripod, pictures were taken in the dark with fixed exposure time, aperture, and gain to obtain comparable pictures. An external trigger can be used to obtain more stable pictures (pressing the trigger manually can vibrate or shift the camera). To verify if the haze is dependent on the wavelength of the incident light, different red, green, and blue laser pointers with wavelengths of 650 nm, 532 nm, and 405 nm were used.
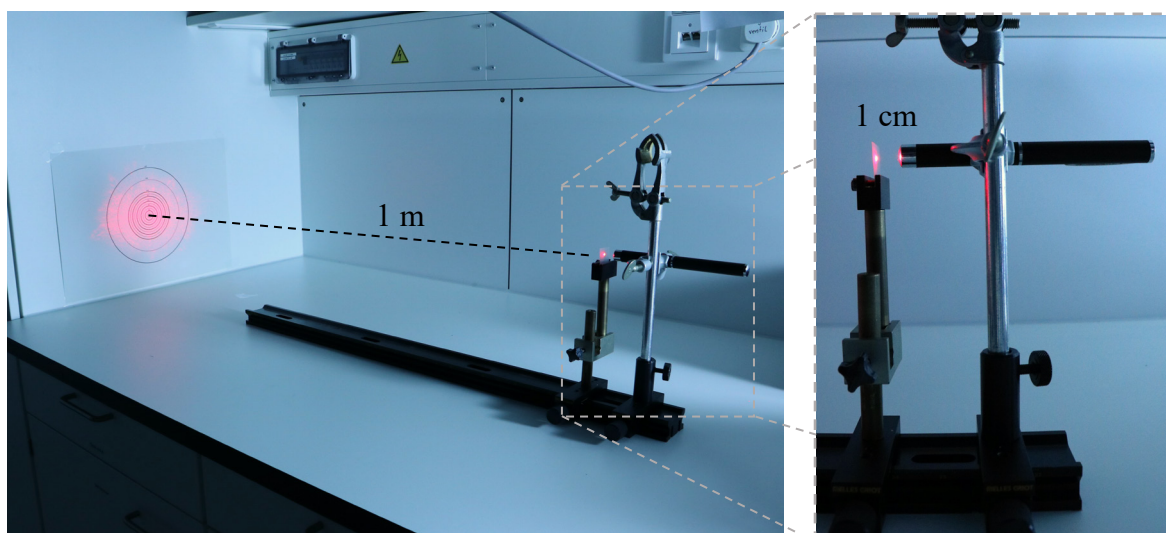

Figure 3.8. Overview of the experimental setup. The laser pointer is fixed at a distance of 1 cm from the sample. The target is at a distance of 1 m. Samples are held with a metal clamp. The camera is at a fixed position to obtain comparable images. Exposure time, aperture, and gain are set to fixed values.

The laser shining through the sample projects a speckle pattern on the target. By determining the size of the pattern, the haze of the sample can be qualitatively assessed: the bigger the pattern, the bigger the haze. Figure 3.9 gives a schematic view of the target pattern. At the target, circular lines indicate radii in 10 mm steps. With the recorded pictures, the haze angle α can be obtained via trigonometric calculation from the radius of the haze shape. At a distance of 1 m, the critical angle of 2.5° is reached by a pattern radius of 43.7 mm.
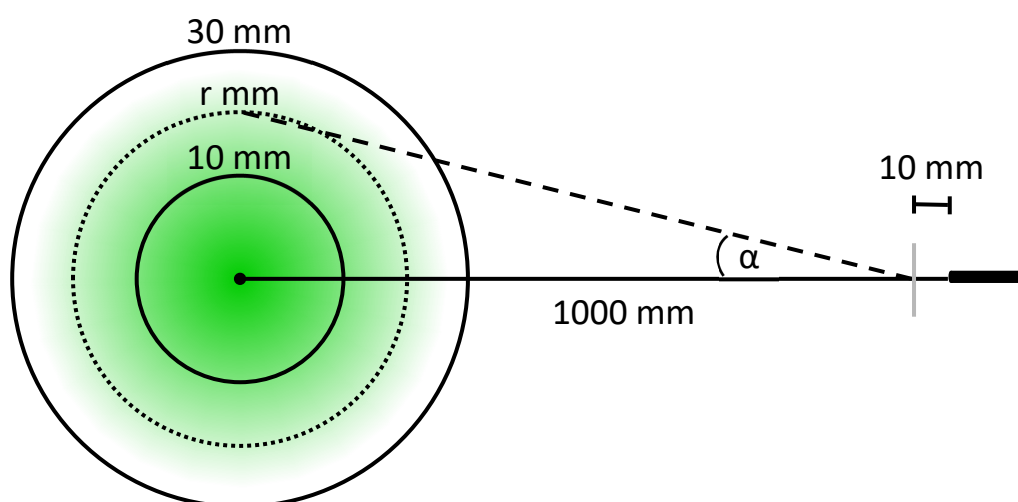

Figure 3.9. Schematic representation of the Haze setup. A laser pointer sends light through the sample which is scattered and projected onto a screen. From the radius of the projected light and the distance to the sample, the pattern angle can be trigonometrically calculated

Validation of the experimental setup was performed using different foil types. Slightly opaque polyethylene (PE), structured polypropylene (PP), and colored polyimine (PI) were analyzed with the three different wavelengths. Figure 3.10 gives the haze pattern radius, the haze angle, and the deviation from the reference angle, measured without a sample in the setup. The diffuse Mylar shows increased haze under all wavelengths with a haze angle of 2.9°. Surface structuration of the foil, as in the case of PP, significantly increases the haze as expected. Here an angle of 5.7° was observed. The clear Kapton exhibits a low haze angle of 1.7° for red and 0.8° for green light respectively. Since the orange foil absorbs the blue light, measurements could not be performed at 405 nm. One must note that the measurements for different samples are only comparable when performed with the same light source, as can be seen especially for the PI foil, for which transmission is highly dependent on the light color. Furthermore, measurements taken with blue light generally show larger haze angles, which is due to the optical brighteners used in many commercially available papers (used for the sighting disk).

This setup is by no means intended to replace an absolute haze measurement, as only a qualitative assessment of the haze is possible. However, these instructions allow building a simple setup using readily available laboratory equipment. As a further validation experiment, this setup was used in Chapter 4. Haze values of printed silver layers on glass and Polyethylenterephthalat (PET) were investigated.
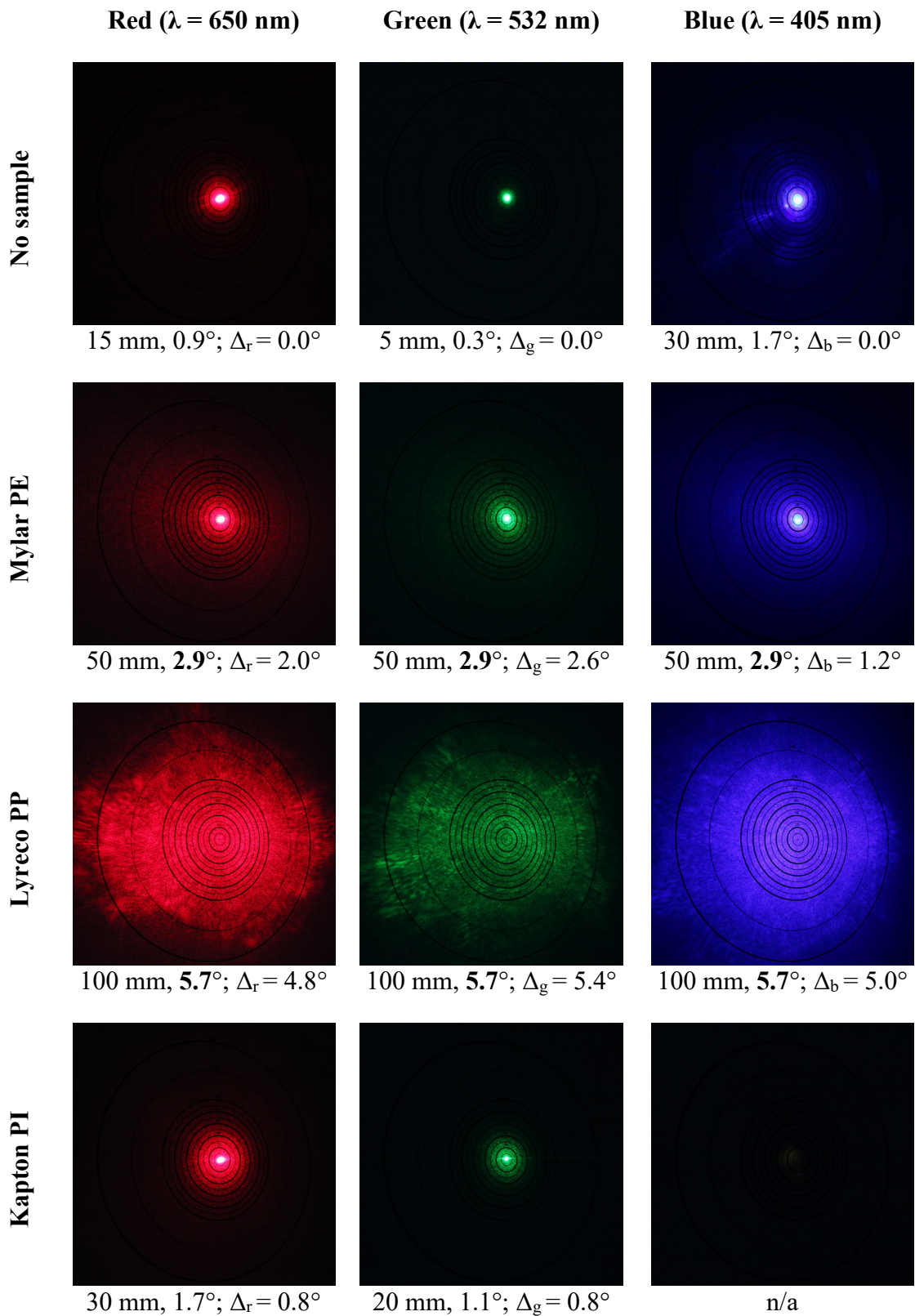
Figure 3.10. Haze quantification of different materials. From the pattern size, the haze angle was calculated. Given under each picture are the pattern radius, the haze angle, and the difference in the angle with no sample. As a yellow foil, the Kapton blocks most of the blue light. Haze angles greater than 2.5° are marked in bold.

3.2.9 Bending

For applications, where electrodes must be flexible, it is important to distinguish if the material properties change when the electrodes are bent. Materials should not fail i.e., show a large increase in resistance, when subjected to bending stress. Bending tests can be used to analyze stress behavior. Here a sample is bent to a known radius and its material properties are investigated before and after bending. An important parameter for these tests is the so-called bending strain ε,[125] which can be calculated as follows:

$$\varepsilon = \frac{d_s}{2r} \tag{3.23}$$

Where d_s is the thickness of the sample and r is the bending radius.

While automatic and more elaborated bending setups have been reported before,[125–127] in this work all bending tests were performed manually by bending the sample over a 3D-printed cylinder with a specific radius.

3.2.10 Electrical and Optical Device Characterization

To evaluate the performance of manufactured OLEDs, their electrical and optical characteristics have to be measured. As described in section 2.4.1 this includes an analysis of the current density versus the luminance as well as optical characterization in the form of electroluminescence spectra. For both measurements, a custom setup was built, and it is described in more detail in this section.

Current Density-Voltage-Luminance: JVL analysis was performed by connecting the OLED device to a two-channel Keithley 2612B SMU power source and measuring the flowing current over a predetermined voltage range. Luminance values at each voltage step are recorded with a Konica-Minolta LS160 luminance meter. A multiplexer board allows automatic pixel switching if a multipixel substrate is used. Pictures of the devices (under operation or inactive) can be taken with the help of an automatic ring light and a USB camera. Targeting of the luminance meter is done manually with an XY stage. While measuring, the specimen can be actively cooled to avoid overheating. Since the whole measurement is light-sensitive, the setup is enclosed in a dark box. The setup is made to be as automated as possible to enable long-term measurements.

The software controlling the setup was programmed fully in C#. It allows to control the measurement instrument and automatically analyzes and plots the OLED characteristics. Next to normal JVL quantifications, lifetime measurements (with different exit conditions), hysteresis analysis, and OLED preconditioning are included in the program. After finishing the measurement, important OLED parameters are calculated automatically as follows:

1. *Current Density:*
   The current density J is calculated from the OLED current I and the active area A of the OLED:

$$J = \frac{I}{A} \tag{3.24}$$

2. *Current Efficacy:*
   The current efficacy η_I of the OLED can be calculated by dividing the measured luminance L by the current density:

$$\eta_I = \frac{L}{J} \tag{3.25}$$

3. *Turn-on Voltage:*
   The turn-on voltage V_{on} is the voltage, at which the OLED is considered to be active. Most of the time, it is defined as the voltage at which the luminance first exceeds a value of $1\,\text{cd m}^2$. However, for low-light emission, a V_{on} of $0.1\,\text{cd m}^{-2}$ might be more appropriate. It is therefore crucial to define the turn-on voltage every time before using it. If the turn-on lies between two measurement points it is linearly approximated.

A copy of the setup is also built into a glovebox to enable measurements under inert conditions. Here the candelameter is replaced by a photodiode. This means that the luminance cannot be directly measured but has to be obtained via a calibration process. Since, in contrast to the candelameter, the photodiode has no internal integration time, the measurement process proceeds much faster.

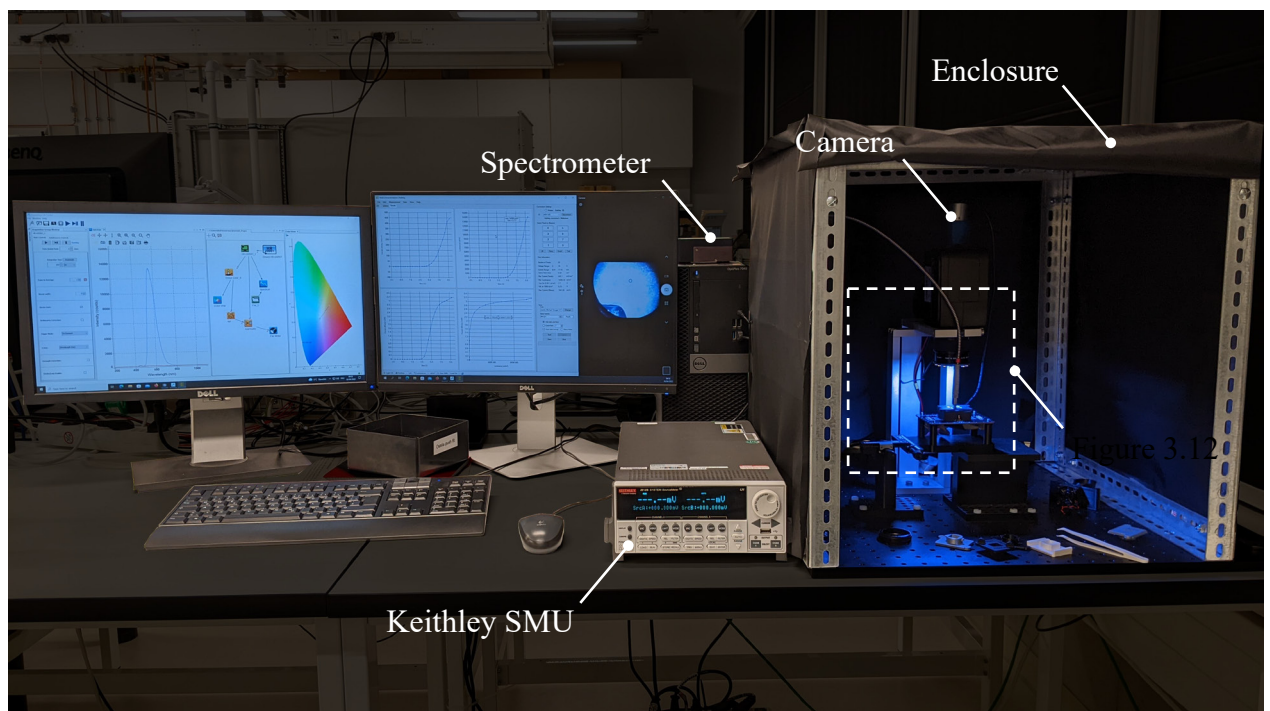

Figure 3.11. Overview of the JVL and EL measuring station. The light-sensitive parts are enclosed to protect from false readings due to stray light. The highlighted section in the enclosure is magnified in Figure 3.12.

Electroluminescence and CIE color: Electronic states in a semiconductor can be excited not only by activation with light (photoluminescence, see section 3.2.1) but also by electronic activation, then called electroluminescence (EL). When an organic semiconductor is connected to an electric current, charge carriers are injected according to the applied voltage. This injection results in the formation of excitons, which can recombine and radiatively or non-radiatively decay. [128] The radiative decay emits light, the wavelength of which is then measured by a detector. From the measured spectra, the CIE color coordinates can be calculated. Defined by the *Commission Internationale de l'éclairage* (CIE) in 1931 these coordinates were the first to define a quantitative link between a distribution of wavelengths in a spectrum and humanly perceived color.[129] In display and lighting technology the CIE coordinates are used to determine the color gamut of a display, meaning the subset of all colors that a display can accurately reproduce. The gamut is dependent on the subpixel wavelength and a wide gamut is preferable for natural-looking colors.[130] For a more detailed explanation of this topic see section 2.1.2.

Electroluminescence measurements were performed using an Ocean Optics CS2000 spectrometer in the custom-made setup shown in Figure 3.11 and Figure 3.12. An optical fiber is attached to the measurement setup by a 3D-printed lid and collects the light of the device. The CIE coordinates were calculated from the EL spectrum with the OceanView software as well as a custom Python script.
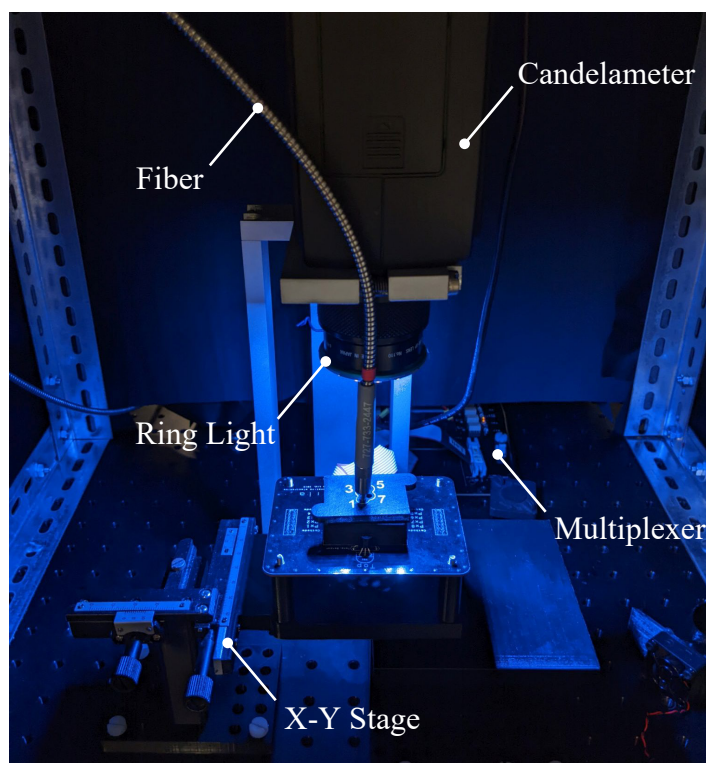

Figure 3.12. Close-up of the JVL measurement setup in the electroluminescence mode. The optical fiber is held in place by a custom-designed 3D-printed lid. For actual measurements, the ring light attached to the candelameter is turned off.

3.2.11 External Quantum Efficiency

As described in section 2.4.1 the external quantum efficiency (EQE) is an important factor when characterizing different OLED architectures. Oftentimes the EQE is not directly measured but calculated from the luminance recorded with a candelameter.[131,132] However, this method is only applicable if an even Lambertian emission pattern is assumed.[133] For correct measurements, an integrating sphere is required and only the forward direction of the emission has to be analyzed.[134,135] The EQE can then be calculated as described below.

Calculation: This section describes the measurement and calculation of the EQE using an integrating sphere. It is important to note that this section assumes that every measurement was recorded with an integration time of 1 s. Therefore, energy and power are not explicitly converted every time they are used. All spectra need to be scaled to a time of 1 s. Per definition the EQE η_{ext} is the ratio between the number of photons n_P emitted from the device and the number of electrons n_E injected into it:

$$\eta_{ext} = \frac{n_P}{n_E} \tag{3.26}$$

When attempting to measure the EQE it is necessary to know the responsivity of the detector used. This means knowing the ratio of generated current and incoming radiation. To achieve this, a calibrated lamp can be used. This lamp is provided with data on its spectral irradiance $E_{e,\lambda}$ measured in W m^{-2} nm^{-1}, meaning how much energy is reaching an area of a certain size, at any given wavelength. Taking into account the opening size of the integrated sphere, the spectral irradiance can be converted to the spectral flux $\Phi_{e,\lambda}$, measured in W nm^{-1}.

For the energy of a photon E_λ at a given wavelength, the following relation applies:

$$E_\lambda = \frac{hc}{\lambda} \tag{3.27}$$

Where c is the speed of light and h is Plank's constant. From this and the lamp power W (at any wavelength), the number of photons (per second) can be calculated:

$$n_P = \frac{W\lambda}{hc} \tag{3.28}$$

Using the following relation between the number of counts of the calibration lamp n_{cL} and device n_{cD}, as well as the number of photons calculated via (3.28) the number of photons (per wavelength) of the device can now be calculated:

$$\frac{n_{P_L,\lambda}}{n_{C_L,\lambda}} = \frac{n_{P_D,\lambda}}{n_{C_D,\lambda}} \rightarrow n_{P_D,\lambda} = \frac{n_{C_D,\lambda}}{n_{C_L,\lambda}} \cdot n_{P_L,\lambda} \tag{3.29}$$

Until now every calculation was done for individual wavelengths. To obtain the total number of photons of the device, the integral over all wavelengths in the data range has now to be calculated. Since the data is present in discrete values, all values can simply be summed up after multiplying them with the bandwidth $\Delta\lambda$ used for the calibration process:

$$n_P = \int_{\lambda_a}^{\lambda_b} n_{P_{D,\lambda}} \, d\lambda = \sum_{\lambda_a}^{\lambda_b} n_{P_{D,\lambda}} \cdot \Delta\lambda \qquad (3.30)$$

Next, the number of electrons has to be calculated. Since the definition of an electrical current is the number of charges per second, and since all timespans here are assumed to be one second, the number of electrons flowing into the device can simply be calculated by dividing the device current I_D by the elemental charge e:

$$n_E = \frac{I_D}{e} \qquad (3.31)$$

Finally, from this, the EQE can be calculated using equation (3.26).

Setup: The EQE setup was built in a dark laboratory to avoid light contamination through windows or other openings. Figure 3.13 shows an overview of all components. An integrating sphere was fixed to an optical table and connected to a spectrometer. For calibration of the sphere, a calibrated halogen lamp can be affixed to a metal bar. After the warmup period, the lamp's spectrum is recorded. An OLED or other device is then mounted to the sphere with a custom-built 3D-printed sample holder. A multiplexer board allows automatic switching of the eight substrate pixels. Controlling the setup and automatic calculation of the EQE value can be done with custom-made software.
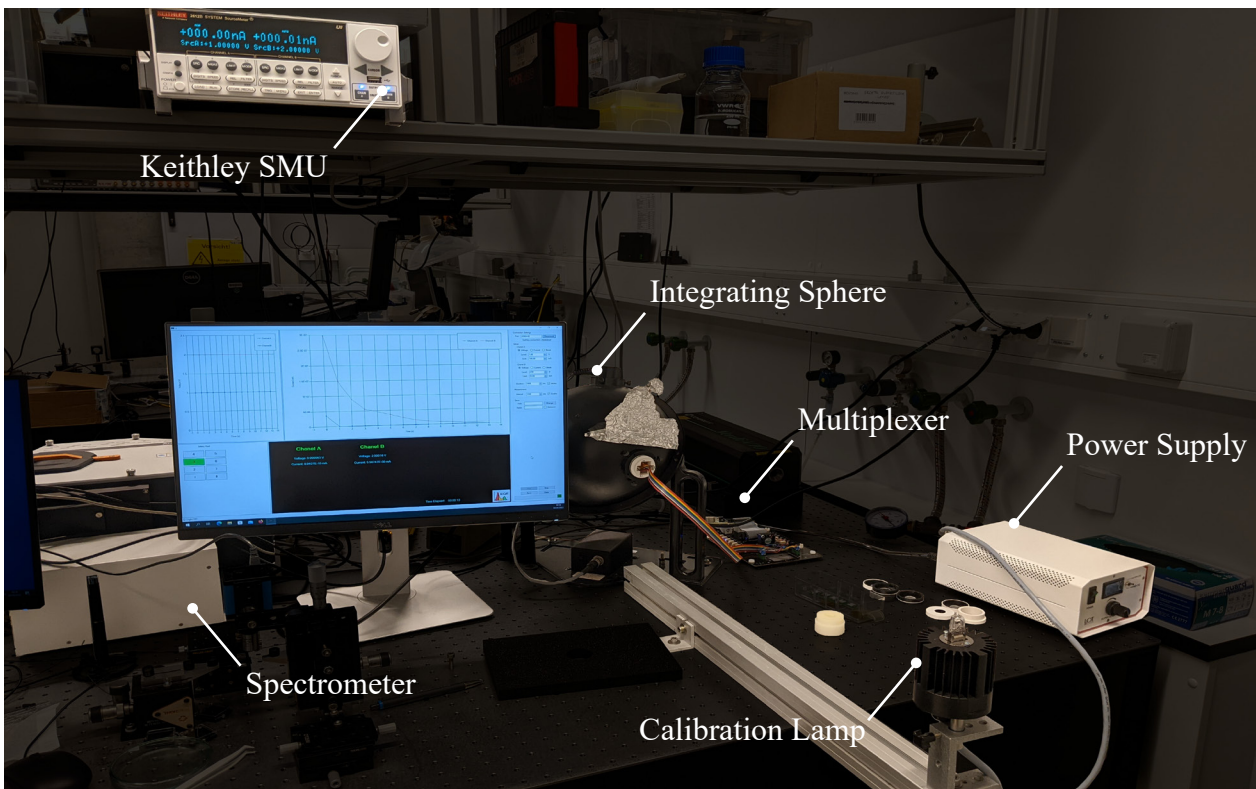

Figure 3.13. Overview of the custom-built EQE setup. An integrating sphere with an attached device mount is connected to a spectrometer. With a calibrated halogen lamp, the detector and sphere can be calibrated.

3.2.12 Laser Structuring of ITO Electrodes

When upscaling the process of OLED fabrication, the problem of scaling the substrates arises. Most substrates are bought pre-patterned and are therefore not easily adaptable to new device formats or sizes. Therefore, a method to structure the substrates as needed is an essential tool when experimenting with novel architectures. This section briefly describes different possible techniques and then focuses on laser structuring and the different important parameters to obtain good quality substrates.
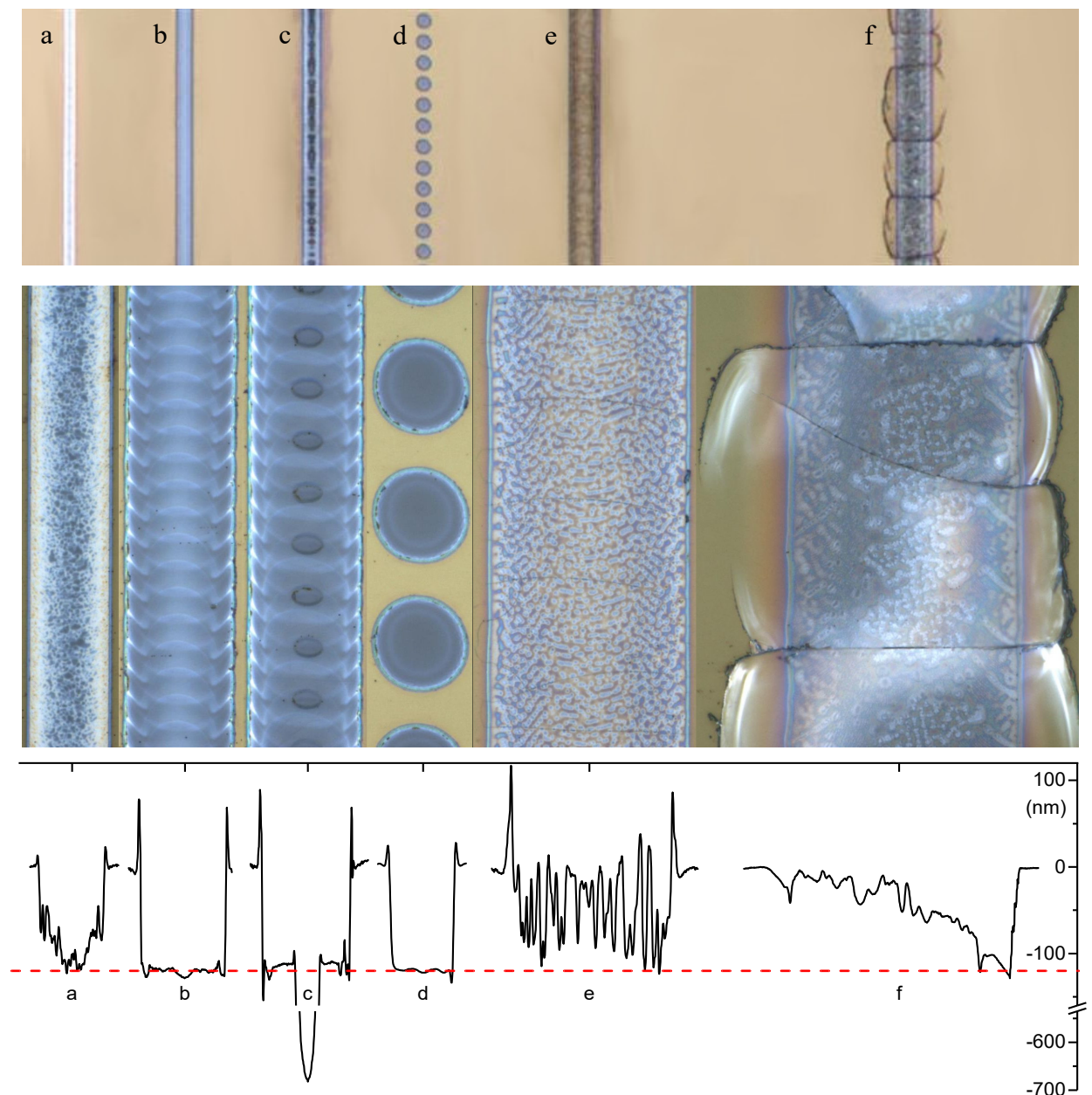
Figure 3.14. Influence of different laser parameters on the structure of a lasered line. The top row shows a 5x magnification of seven lasered lines with different parameters. In the middle row is a 100x magnification and the bottom row displays the line profiles. The red line marks the ITO thickness of 120 nm. Parameters are: (a) energy too low, (b) correct settings, (c) energy too high, (d) mismatch in firing frequency and printing speed, (e) focus too low, and (f) focus too high.

For the de-facto standard transparent electrode material ITO, there exist three main approaches to obtaining structured substrates. Using shadow masks when fabricating the ITO layer directly leads to the desired electrode pattern. However, not every facility has the capability to fabricate ITO electrodes. Hence, patterning an ITO layer by chemical or physical means is an alternative approach. Chemically, ITO can be structured using a combination of metallic zinc powder and hydrochloric acid in what is called a wet etching process.[136] Although not a complicated process, the areas where conductivity is desired must be masked in a time-consuming process to avoid accidental etching. The same applies to so-called dry etching processes, in which the ITO is removed with different gases in a plasma process.[137] The physical structuring of ITO utilizes a variety of different lasers and wavelengths to remove the ITO. Via the absorption of the laser energy, the ITO is vaporized or ablated from the substrate.[138,139]

A large number of different parameters can be adjusted during the lasering process in order to achieve optimal structuring results. Figure 3.14 gives an overview of the effects some of these parameters have. For this experiment, a line was laser-etched into a 120 nm ITO layer with a 1064 nm pulsed laser, varying the laser speed, power, firing frequency, and focus. A height profile of the lines was recorded after lasering. Too low an energy (as shown in Figure 3.14a) will result in the ITO layer not being completely removed, while too high an energy (c) can damage the underlying substrate. The correct energy setting (b) results in a clean line profile. As can be seen on most profiles, the edges of the lasered lines have high ridges caused by the high amount of melted material during laser exposure.[139] Kim et al. have found that these can be avoided using shorter lasering pulses in the range of pico- or femtoseconds.[140] If the laser frequency is too low or the laser speed is too high, the laser pulses do not overlap and no continuous line is formed (d). Setting the focus of the laser too low (e) or too high (f) results in a broadened line with only partial removal of the ITO layer. All of these parameters depend on the material used and can already be different for another batch of the same material. They must therefore be worked out experimentally.

With the right set of parameters, structures down to a width of 20 μm can be manufactured with the PiXDRO LP50 laser system. This is small enough not only to pattern the finger-electrodes used in the fabrication of upscaled OLEDs but also to allow intricate details to be inscribed. The capabilities of this process were investigated by inscribing the logo of Humboldt-Universität into an ITO substrate and producing an OLED from it. An overview of the process can be seen in Figure 3.15. Since bottom-emitting OLEDs were fabricated, the logo has to be mirrored prior to lasering. When analyzing the lasered pattern under an optical microscope, the rastering process is visible. Each pixel in the template is converted into a laser pulse (see Figure 3.15b). In order for the current to flow to every point on the substrate, it is important to note that closed loops must be avoided at all costs. Fabricating inverted, bottom-emitting OLEDs from the laser-etched substrates results in efficient OLEDs with an active area of 3.6 cm^{-2}.

Structuring of ITO is of course not the only material possible for laser patterning. In the course of this thesis, thin metallic layers as well as fluorine-doped tin oxide (FTO), an ITO alternative have been structured as well.
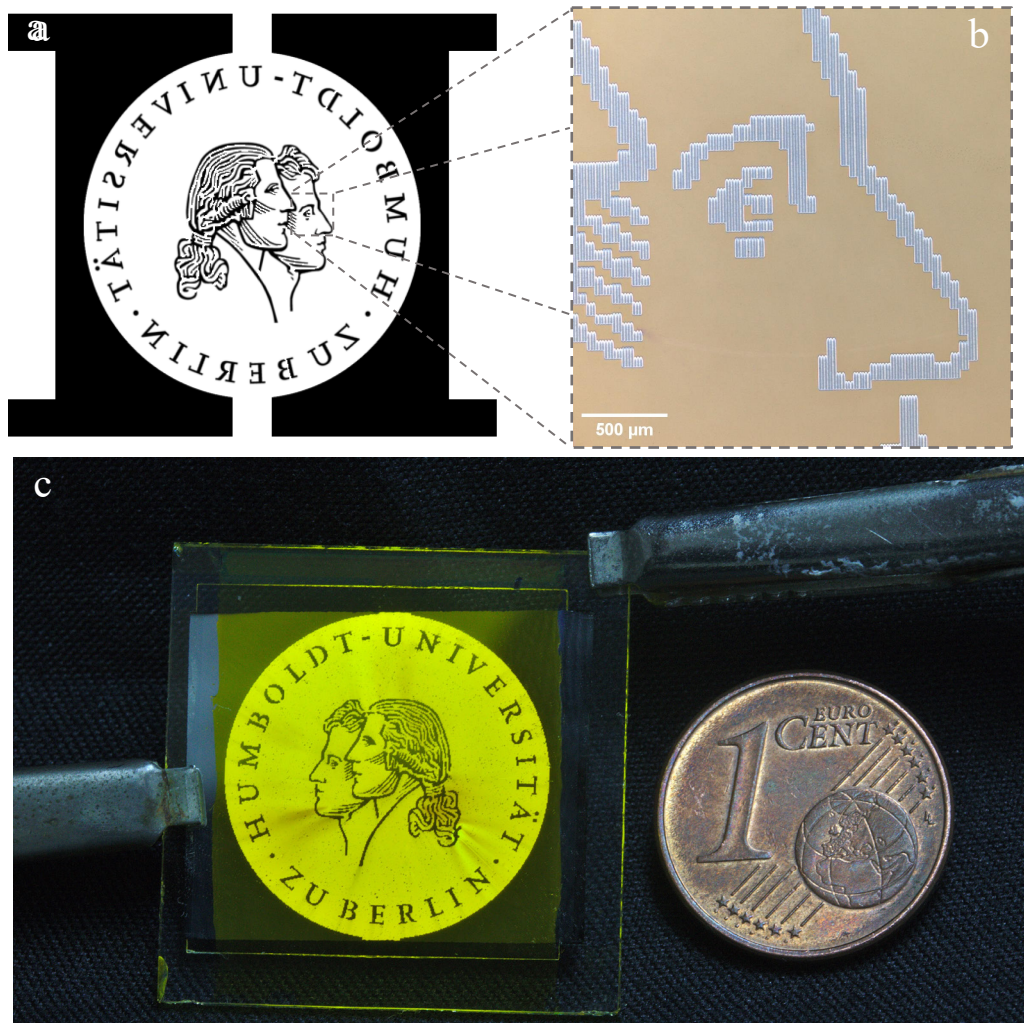
Figure 3.15. Overview of the laser structuring process. (a) the necessity of flowing current does not allow for closed "loops" like in the case of the letters "O" or "A". The current must be able to pass freely throughout the substrate. (b) shows a closeup of the resulting lasered substrate. The individual lasering lines are visible. (c) working OLED device with lasered structure. Since a bottom-emitting architecture is used, the pattern has to be lasered in a mirrored orientation to obtain a correct final OLED. The active area of the OLED is 3.6 cm^{-2}.

4 Solution Processing of Flexible Electrodes

Understanding the properties of electrodes in optoelectronic devices is essential for highly efficient applications. The first subchapter deals with OLEDs implementing printed silver electrodes while the second investigates the use of semitransparent gold electrodes for applications where silver is not suitable. The fabrication process of electrodes made from solution-processable materials is introduced in the beginning. Transparent electrodes are made from printed silver and doctor-bladed gold inks on rigid as well as flexible substrates. Both inks are particle-free, metal decomposition inks. The electrodes are analyzed in terms of optical and structural properties and are, as a proof of concept, applied in devices. For the silver and gold ink, organic light-emitting diodes were fabricated.

4.1 Printed Silver Electrodes for Flexible OLEDs

Parts of this section have been previously published.[141] Additional data has been included.

4.1.1 Introduction

As described in Chapter 2, OLEDs need at least one transparent conductive electrode to ensure functionality. With LEDs, the light-emitting chip is contacted with bonding wires, while with OLEDs, in contrast, planar electrodes are used to enable large-area light emission. The light generated must therefore pass through at least one of the electrodes to leave the device. To achieve this, an electrode needs to be transparent and able to conduct electricity. This implies, that high transparency, as well as conductivity, are required. Indium tin oxide (ITO), today's de-facto standard for most electronic appliances, meets these requirements.[142,143] However, the trend of moving to more and more bendable and flexible devices is causing issues for ITO electrodes due to its inherent brittleness. [144]

Thin metallic films have been a promising candidate as a replacement for ITO. These can be fabricated by two main approaches. Thermal evaporation (see also section 3.1.3) of thin metal films or dielectric-metal-dielectric compounds,[145,146] and solution-based methods such as roll-to-roll processing,[147] screen printing, spray coating,[45] or inkjet printing.[148] The latter method of inkjet printing is commonly used with metal nanoparticle inks, as well as metal-organic decomposition (MOD) inks.[147,149] MOD inks consist of oxidized metal precursors dissolved in suitable solvents and mixed with additives, or contain metal-organic complexes.[150] While the agglomeration of particles reduces the effective shelf-life in nanoparticle inks, MOD inks mostly do not suffer from agglomeration and are therefore considered more stable.[151]

To obtain transparent electrodes, metal inks can be processed into two different structures. A thin grid of opaque lines can conduct current while light can simultaneously pass between them, making the overall electrode highly transparent. Here, the factors affecting transparency are the line width and thickness. Different patterns such as lines or a hexagonal grid have been studied previously.[148] In contrast to those, semi-transparent electrodes can be produced by printing metal inks in a very thin layer, making the resulting electrode highly transparent as well as conductive. Metal nanowires are the material of choice here.[152–154] Both types of electrodes exhibit significantly higher resilience to bending stress when compared to ITO. The resistance (relative to the initial value) of these metal nanowires doubles only after several hundred bending cycles.[152,155]

In contrast to evaporated electrodes, which do not require post-processing to reach their full conductivity, most solution-based methods require a so-called sintering process. It aims to not only drive off any remaining solvents but also to remove stabilizing capping agents to allow particle agglomeration into a homogenous layer (for nanoparticle inks).[147] In MOD inks the metal precursors are reduced to form a metallic layer.[151] Sintering of nanoparticle inks happens mostly via heat transfer to the particle. A multitude of processes such as thermal, photonic, laser, electrical, or plasma sintering can be employed. [156–159] However, most substrate materials used for flexible applications are very temperature sensitive. Therefore, high sintering temperatures (commonly used temperatures are $\geq 150\ °C$) would not allow substrates such as PET to be used due to their low temperature stability (glass-transition temperature $T_g = 70\text{-}80\ °C$).[160]

Plasma treatment is a viable alternative that relies primarily on a low-pressure atmosphere to remove unwanted compounds after printing.[157] Additionally, the plasma can break down constituents with a longer chain into more volatile compounds.[161] While being mostly employed to rid the printed layer of unwanted chemicals, it can be directly used, in combination with a reducing gas, to reduce metal precursors in MOD inks.[162–164]

In this chapter, a silver MOD ink was utilized to produce highly transparent, conductive electrodes. An argon plasma is applied to the printed ink to reduce the metallic precursors. No reducing gas, such as H_2 is needed. The metallization process requires no additional heating and generates only a minimal amount of heat itself, making the procedure especially suitable for the production of flexible electrodes. These electrodes are then shown to be effective as transparent, flexible electrodes for OLEDs.

4.1.2 Materials and Experimental Setup

Metallization Ink: Inks were provided by OrelTech GmbH. The OTech T1053 plasma metallization ink consists of organic solvents to facilitate inkjet printing mixed with a metallic precursor, containing Ag^+ cations.[165] The viscosity of the ink was measured using an Ostwald (U-tube glass capillary) viscosimeter. Ink surface tension was evaluated by applying the drop weight method. This method uses the relation between the weight of a drop and the surface tension of a liquid that has just separated from a capillary. With the help of the known mass and surface tension of a drop of a reference liquid, the surface tension of the unknown liquid can be estimated.

Solution Preparation: The PDY-132 (Super Yellow, Sigma-Aldrich) light-emitting polymer was dissolved in toluene at concentrations of 5 mg ml^{-1}. Prepared solutions were stirred for several hours at 50 °C before being used. Zinc oxide (ZnO) nanoparticle solution (Genesink, 1% dispersion in isopropanol, particle size 12 nm) was used as received. A solution of polyethyleneimine (PEI) was prepared according to literature by dissolving PEI (Sigma Aldrich, $M_W = 25\ 000$ g mol^{-1}) in isopropanol to obtain a concentration of 0.4 wt%.[166].

Sample Preparation: Glass and PET substrates with patterned ITO (Psiotec Ltd.) for device preparation, quartz glass, Melinex PET and Kapton for spectral analysis, and soda-lime glass for thickness measurements were cleaned by thoroughly wiping them with acetone (for glass samples only) and isopropanol. Afterwards, a 7 s O_2 plasma treatment in a Femto plasma system

(Diener) at a gas pressure of 0.35 mbar and 50 W of power was used to activate the sample surface before solution deposition.

Inkjet Printing: Printing was done on a PiXDRO LP50 inkjet printer (Meyer Burger / Süss Microtec) with a Spectra S-Class printhead. This head has a nominal drop volume of 30 pl and was used at a resolution of 850 dpi. Samples were transferred back to the Femto plasma system after printing and dried using a vacuum until a pressure of less than 0.1 mbar could be reached in the chamber. By applying an Ar plasma with a gas flow of 20 sccm and a power of 250 W for 5 min, the samples were reduced to metallic silver. The size of the printed area influenced the drying time but not the curing time.

Thin Film Characterization: X-ray powder diffraction (XRD) experiments were performed using a Rigaku TTRAX III (18 kW) instrument with K_α radiation from Cu (1.54 Å) and parallel beam configuration. 2θ mode was used and the scanning angle was varied from 15° to 47° with steps of 0.025°. Since glass substrates would lead to unspecific broadband signals due to their partially amorphous composition, silicon was chosen as the substrate for the XRD analysis. Due to its very defined diffraction signature peaks, it is easily differentiable from the specimen signal. UV-Vis spectra were taken with a Perkin Elmer Lambda 950 double-beam spectrometer. The sample surface was analyzed using a scanning force microscope (Bruker FastScan) in tapping mode and a LEXT OLS4100 confocal laser microscope (Olympus). With a 4-point probe (Jandel) the sheet resistance was assessed. Qualitative haze evaluation was performed according to section 3.2.8.

Device Preparation: Pre-patterned ITO (on glass and PET) substrates, where the ITO only acts as the contact electrode (see Table 4.1), were prepared as described above. The electrode was then printed in the middle with the Ag ink and cured. A ZnO:PEI blend (2:1 by volume) was spin-coated on top of the printed silver at 2500 rpm and dried for 10 min on a hotplate at 120 °C for glass and 100 °C for PET. An 80 nm thick emitter layer of Super Yellow (SY) was spin-coated for 60 s at 2500 rpm in ambient conditions. Finally, a top electrode of 10 nm of MoO_3 and 200 nm of silver was evaporated thermally under vacuum with a base pressure of 10^{-6} mbar. Shadow masks were used to make devices with 0.04 and 0.49 cm^2 of active area. Encapsulation was done using glass slides and UV-curable resin (Ossila), cured at 365 nm for 10 min.

Device Characterization: Devices were characterized by measuring current density-voltage-luminance curves with a Keithley 2612B source meter and a Konica Minolta LS-160 luminance meter with a purpose-built setup (detailed description in section 3.2.10). Electroluminescence spectra were recorded on a CS 2000 spectrometer (Ocean Optics) using OceanView software.

4.1.3   Ink Development and Printing Process

Development of the utilized ink was done at OrelTech GmbH. The ink is specifically tailored to suit the inkjet fabrication process in this work. Multiple iterations have been done to perfect the adhesion on glass as well as flexible substrates. At room temperature, the final ink (OTech T 1053) had a viscosity in the range of 10-12 cP and surface tension in the range of 25 to 30 mN m^{-1}. Curing conditions for the ink were established by preliminary experiments. Ag ink was spin-coated on simple glass slides and subsequently dried and cured with different gas flows and power levels.

Electrodes from the Ar plasma then directly reduced the metal precursors to a thin metallic layer. Although higher power levels led to a reduction in the necessary curing time, it was found that rapid drying was the more relevant parameter. Even with plasma-assisted activation of the sample surface prior to solution deposition, de-wetting, especially from the edges or impurities of the samples, was found to be an issue. This was lead to holes or a not fully closed metallic layer in the final film. Therefore, after solution processing, the samples had to be transferred to the plasma chamber as fast as possible. When vacuum-drying the samples, it could be shown that the solution was sufficiently immobilized (by evaporation of volatile ink components) when reaching a base pressure below 0.4 mbar.

When transferring the process to printing the same challenges persisted. A high resolution (more material) of 850 dpi had to be chosen to get closed films and to counteract the strong coffee-ring effect.[167] Since printing was done with a particle-free MOD ink, clogging of the printhead was not an issue. An overview of the whole production process can be seen in Figure 4.1, device production and characterization will be discussed later.
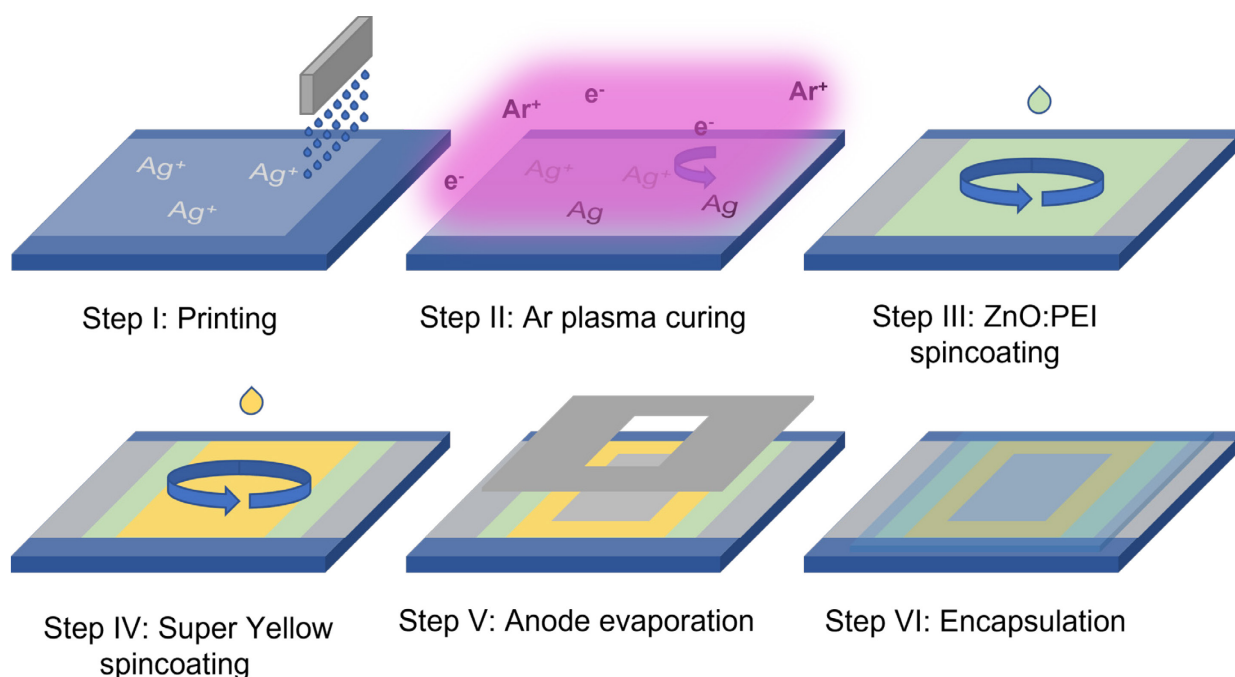

Figure 4.1. Schematic overview of the device fabrication steps. Silver ink is printed on cleaned samples and cured in an argon plasma. The organic layers are spin-coated on top, and a MoO_3/Ag electrode is evaporated by a shadow mask. Finally, the devices are encapsulated for protection.

An XRD diffractogram of the printed layer was recorded (see Figure 4.5a) and shows no other peaks than the expected silver (111), (200), and (220) peaks. Thus, it can be concluded that the plasma process is able to eradicate all residual organic compounds and turn the ink into metallic silver.

4.1.4 Characterization of Printed Electrodes

Printing of samples was performed on different substrate types. Standard samples were produced on glass and flexible Melinex PET and Kapton. As can be seen from the optical microscope images in Figure 4.2, glass samples show a highly crystalline surface of the silver layer with almost no holes or other impurities. For PET less crystallinity but many more defects could be observed. When increasing the brightness of the picture, it is visible that imperfections that are already present in the substrate, translate to imperfections in the printed layer. Kapton, with a much smoother surface, was therefore also investigated as a possible substrate and was shown to yield more crystalline films with a greatly reduced number of defects. However, Kapton has a strong coloration and is therefore not suitable for OLED applications where a good color rendering is required. Melinex PET was therefore chosen as a smooth substrate material.
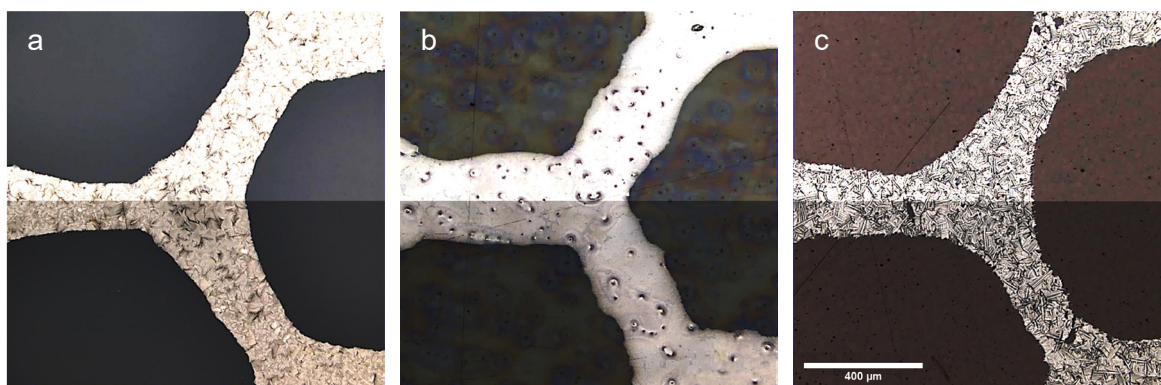

Figure 4.2. Printed grid on different substrates. (a) Glass, (b) PET, and (c) Kapton. The brightness of the top halves of the images was increased to illustrate the effect of the substrate features on the printed structures.

UV-Vis measurements were carried out on glass and PET samples with a printed silver layer and compared with standard samples containing an ITO electrode. Figure 4.3a shows that both electrode materials on glass have a high transmission over the full visible spectrum between 350 and 800 nm. While ITO reaches up to 98% of transmission printed Ag can achieve 75% to 80%. The Ag electrode also exhibits a very even transmission over the full spectrum, enabling accurate color representation in OLED devices. However, especially for printed silver, there is a tradeoff between transparency and conductivity. Both are highly dependent on the film thickness. A higher conductivity is achieved with thicker films while the transmission simultaneously decreases. For flexible PET substrates, Figure 4.3b displays the same curves. Printed silver still shows transmittance values > 50% over the full visible spectrum, while the ITO electrode has a higher transmission. Linearity though is better in printed samples.

To determine which properties of the silver lead to the high transmittance, the surface of prints was further investigated. SFM as well as optical microscopy pictures were taken and are displayed in Figure 4.4. When the silver ink is drying, it forms a highly crystalline structure that is maintained even after the plasma curing process. As can be seen in Figure 4.4a and b, this structure is not fully even, the thin parts of it allowing more light to pass through, while the

thicker parts conduct the electricity better. The SFM picture shows that these features are present even on a lower micrometer scale. From the profile extracted from the SFM picture (see Figure 4.4c) it can be determined that the layer thickness for prints with 580 dpi is between 15 nm and 38 nm. With an average transmittance of 77% and a sheet resistance (determined via 4-point measurement) of 16 Ω sq^{-1}, the printed Ag on glass demonstrates a good compromise between conductivity and transparency.
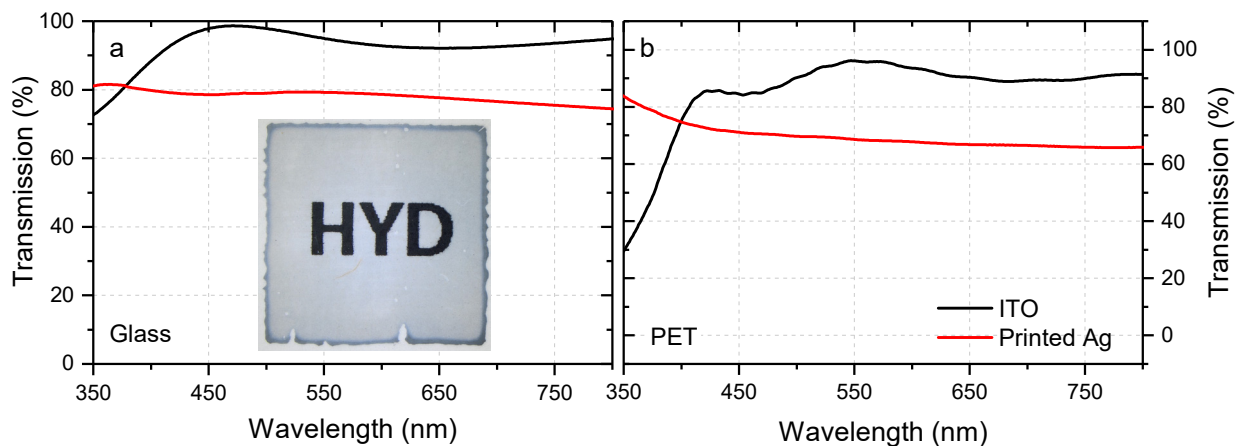

Figure 4.3. Optical characterization of the printed layer in comparison to ITO on different materials. (a) Glass sample. Ag shows good transmission (> 70%) over the whole visible spectrum. (b) PET sample. Transmission of Ag on PET decreases for higher wavelengths.

For flexible electrodes, there is another important parameter to take into account. When utilizing these samples in bent applications, the electrodes are under constant or momentary bending stress. In good electrodes, bending should not result in a significant increase in sheet resistance. This behavior was investigated by performing bending tests on PET substrates with printed silver as well as on PET/ITO samples. Samples were subjected to 150 bending cycles with a bending radius of 5 mm, corresponding to a cyclic strain of 2%, according to the formula stated in section 3.2.9. The results in Figure 4.5 illustrate a clear difference between ITO and printed silver in terms of relative resistance (resistance divided by the initial value). While Ag electrodes exhibit next to no change in resistance (23% increase after 150 cycles) ITO resistance doubles already after five cycles and increases to over 100 times the initial value after 15 bends. Total failure (no measurable conductivity) occurs after 80 bending cycles. This is to no surprise, as the brittleness of ITO is well known and has been discussed in the introduction to this chapter.

For electrodes used in display or lighting applications, it is important to know how the electrode scatters the light. This so-called haze was qualitatively investigated with a custom-built setup. Section 3.2.8 describes the setup and its capabilities in more detail.
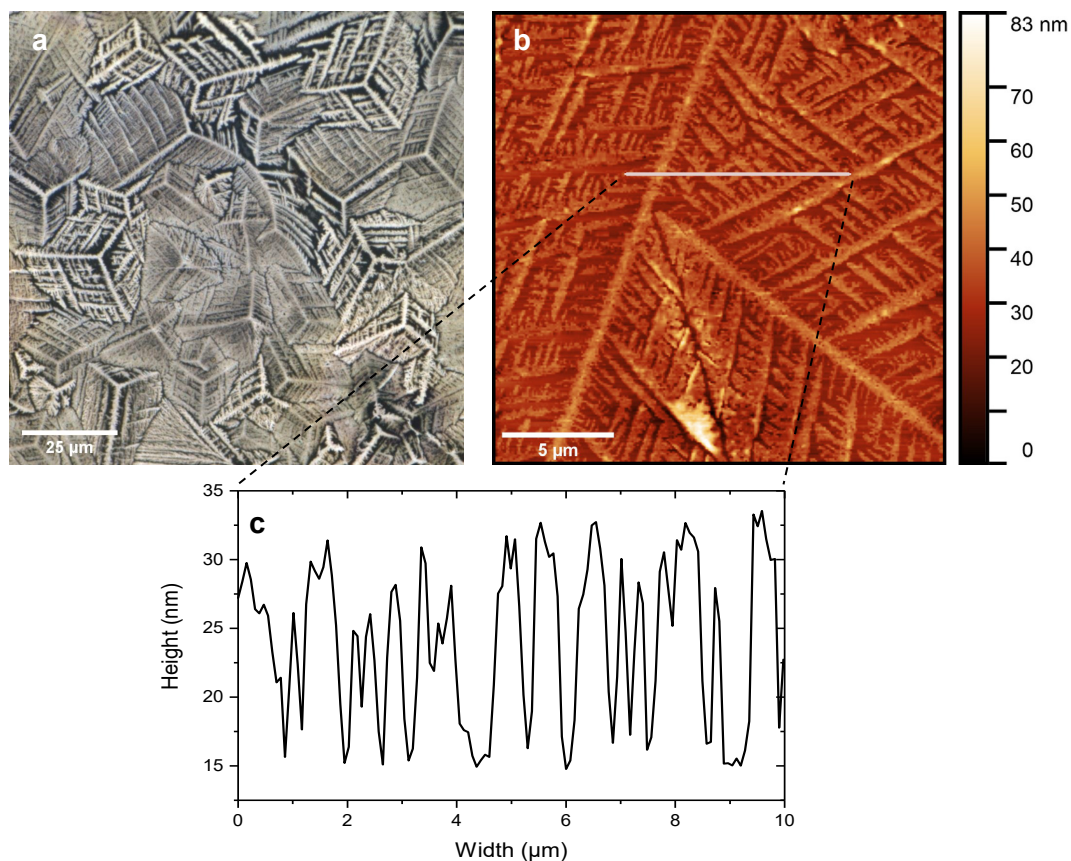
Figure 4.4. Characterization of a printed silver layer. (a) The optical microscope image shows the high crystallinity of the sample. Gaps between the crystal structure are responsible for good optical transmission. (b) The same structures are visible in the SFM images on a smaller scale. (c) height profile extracted from (b).
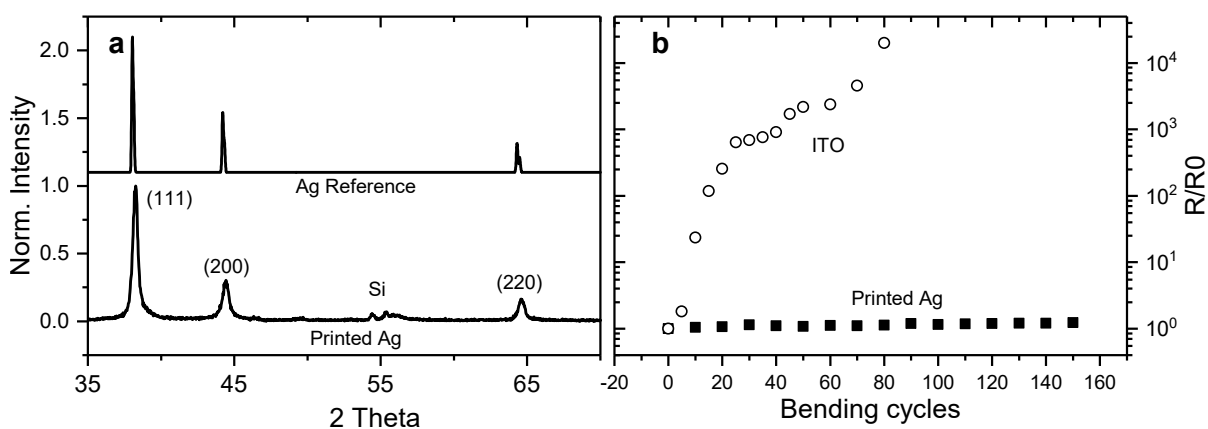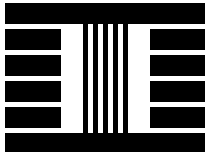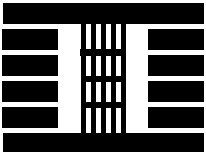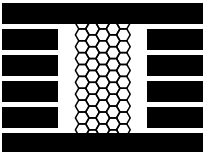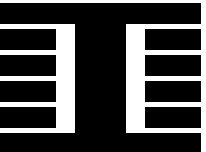
Figure 4.5. Elemental and mechanical characterization of printed Ag. (a) XRD diffraction pattern on silicon shows no other peaks than the expected (111), (200), and (222) peaks (except the Si substrate peak). An Ag reference from literature is shown above.[168] (b) Bending tests performed on flexible Ag and ITO electrodes. While printed Ag retains its low relative resistivity over 150 bending cycles, ITO resistance increases rapidly after a few bends.

It was found that the haze of printed layers on glass as well as on PET is just marginally larger than that of the plain substrates. Since there is more roughness in the PET sample, a larger haze was observed here than with the glass substrate. Melinex PET and glass were analyzed with and without printed silver. The haze pattern radius, the haze angle, and the deviation from the reference (no sample) are shown in Figure 4.6. Pure glass exhibits almost the same haze angle as the reference with a maximum deviation of $\Delta_b = 0.6°$ for measurements at 405 nm. For plain PET the largest difference in the haze was measured for the green light with $\Delta_g = 0.3°$. Haze angles were always below the critical angle of 2.5°. Printing silver on glass did not alter the haze for any of the investigated wavelengths. In the case of printing on PET, the haze was slightly increased with $\Delta_r = 0.8°$, $\Delta_g = 0.8°$, and $\Delta_b = 0.3°$ while again, staying below a haze angle of 2.5° for all three light sources. The higher values on PET can be attributed to the higher roughness of the sample, causing more scattering of the incident light.

4.1.5 Electrode Pattern

As discussed in the introduction to this chapter, not only the electrode material but also its pattern can highly influence the performance of the finished printed electrode. While full-area layers have to use semi-transparent materials to achieve adequate transmission, grid-like patterns rely on the spacing in-between lines to allow light to pass. The lines can be printed in different patterns. Linear grids are fast and easy to print, while hexagonal patterns allow alternative current routes in case of a defect.[148] For the OrelTech ink used here, all three electrode patterns (full area, lines, hexagonal grid) were investigated. Additionally, line patterns with horizontal busbars were fabricated to combine the advantages of linear and hexagonal patterns. Table 4.1 gives an overview of the electrode structures manufactured as well as the area covered by the print and the resistance of the electrode (measured between diagonal corners). While the addition of a busbar to the linear electrodes substantially reduced the resistance, hexagonal patterns still exhibited lower resistance and were therefore used for further experiments. Since the ink is semi-transparent when fully cured, full-area samples were further investigated as well and showed the lowest resistance.

Table 4.1. Overview of the manufactured electrode patterns. Resistance was measured between diagonal corners. Due to their favorable properties, hexagonal and full substrates were used for further experiments. The contacting fingers of the substrates were made from pre-patterned ITO.

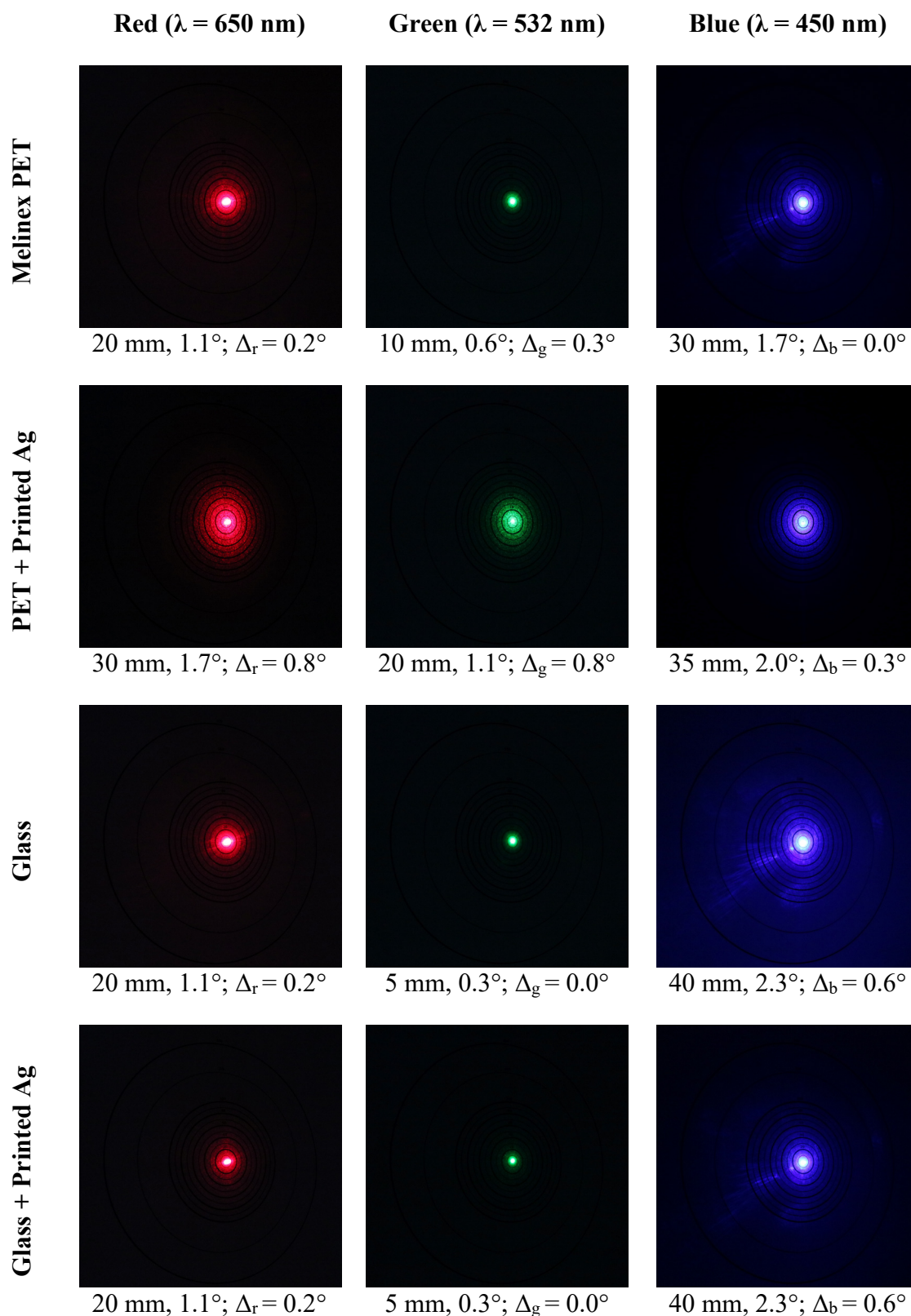|	Lines	Lines + Busbar	Hexagon	Full
Image				
El. Area	50%	57%	25%	100%
Resistance	390 Ω	132 Ω	119 Ω	100 Ω

Figure 4.6. Haze quantification of printed samples compared to blank substrates. The inclusion of the printed layer does not alter the haze significantly on glass as well as on PET. Pictures of the haze pattern, the haze radius and angle calculated from it, and the difference to the haze angle without a sample are shown. For more details on the setup and evaluation, see section 3.2.8.

As can be seen in Figure 4.7a, well defined structures could be achieved, especially for the very thin lines in the hexagonal pattern. To test the functionality of the electrodes, a batch of SY OLEDs was fabricated. Figure 4.7b and c show working devices at a voltage of 4 V utilizing a hexagonal grid (b) and a full-area electrode (c). While in the hexagonal case only the grid and areas very close by are lighting up, the full pixel is active in the case of full-area OLEDs. This can be attributed to the very low conductivity of the utilized ZnO layer in inverted OLEDs. Other research has shown that hexagonal patterns are a valid electrode option for OLEDs.[148] Due to the fact that the investigations in this chapter focus on inverted OLEDs, the full-area electrode was utilized in all further experiments.
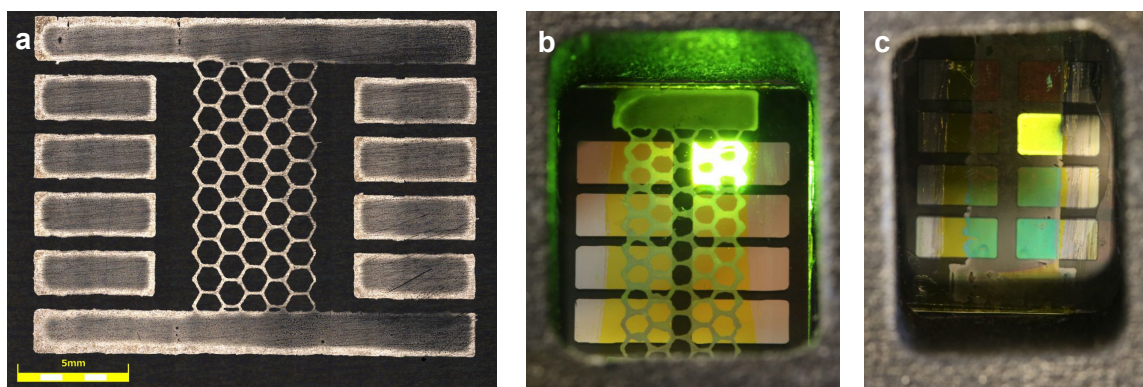

Figure 4.7. Images of printed electrodes. (a) Fully printed electrode structure. (b) Hexagonal pattern. (c) Full-square pattern. Devices are driven at 4 V. Due to the lower conductivity of the zinc oxide layer in comparison to the silver, in (b) only the near vicinity of the hexagon lines and the lines themselves light up.

4.1.6 Functional Device Characterization

After the basic characterization of the electrode was finished, bottom-emitting OLEDs with an active area of 0.49 cm^2 were produced to compare them with ITO. As substrates glass, as well as flexible PET, was used. For electrical quantification, JVL curves were recorded for OLEDs containing a printed electrode as well as OLEDs with a classical ITO one. The results of these measurements are shown in Figure 4.8 and Table 4.2.

Regarding the rigid devices (Figure 4.8a-c) it was found that while the current density is similar for both electrodes at first, printed silver electrodes surpass the ITO ones quickly. This can be attributed to the lower sheet resistance of the Ag electrodes which was measured to be around 16 Ω sq^{-1} for printed Ag and 20 Ω sq^{-1} for ITO. The luminance curves (Figure 4.8b) show a similar trend with printed silver exceeding ITO. The turn-on voltage (voltage at $L = 1$ cd m^{-2}) was found to be equally at $V_{on} = 2.5$ V for both electrodes. This suggests that there is no additional electronic injection barrier introduced when switching from ITO to Ag. Although silver electrodes are able to surpass ITO in terms of luminance in the shown voltage range, ITO can achieve higher absolute luminance values as can be seen in Table 4.2. However, since a lower operating voltage is advantageous in most applications, this is not an issue. Current efficacies, as can be seen in Figure 4.8c, show printed Ag OLEDs to be more efficient in the given voltage range.

In terms of electroluminescence, both OLED devices show a similar spectrum (inset in Figure 4.8b, measured at L = 1 000 cd m^{-2}) with a spectral maximum λ_{max} at 550 nm resulting in CIE1931 coordinates shown in Table 4.2.
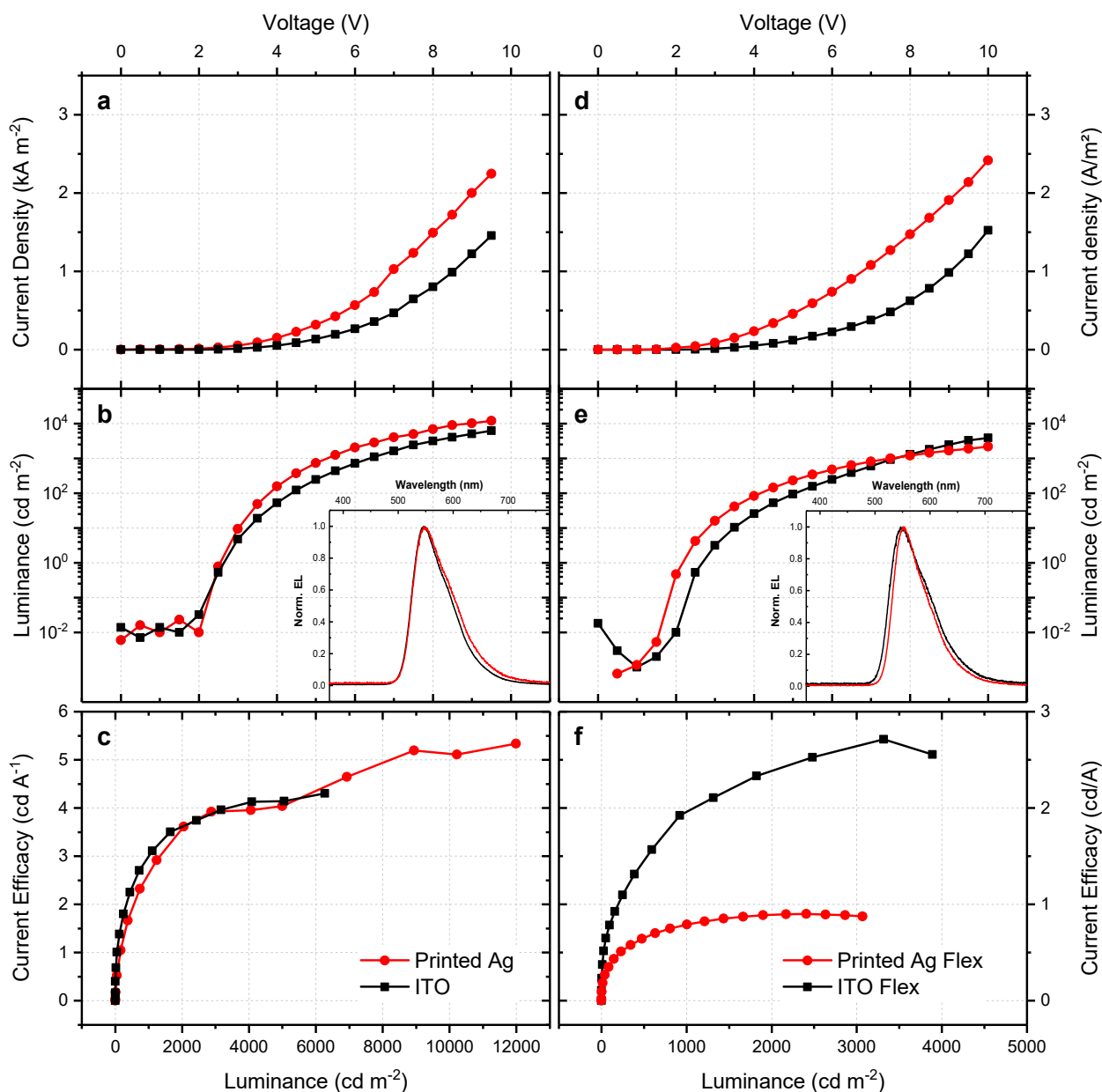
Figure 4.8. JVL characterization of printed Ag vs. ITO OLEDs. OLED substrates are made of glass (a-c) and PET (d-f). A steeper increase in current density is visible in the JV curves for printed silver (a, c). Luminance is increased for printed Ag on glass (b), but maximum luminance is larger for ITO on PET (e). For glass samples, higher efficacies can be reached with printed silver electrodes (c). On PET, Ag decreases the efficacy roll-off (f).

For flexible devices (Figure 4.8d-f) the same trend was observed in terms of current density. Both electrode types have similar densities at first, but printed Ag has a faster increase. The more linear shape of the current density curve of Ag compared to ITO hints at the presence of ohmic shorts which could be also seen as a larger current when plotting in the reverse direction

of the diode. The influence of these shorts could be minimized by preconditioning the device at -20 V prior to the measurements. Luminance values (Figure 4.8e) show similar behavior to rigid electrodes. Although the transmission of the printed silver is lower compared to ITO, higher luminance values could be achieved. While the device performance would be expected to be negatively affected by the lower transmission, the higher conductivity of the printed silver achieves increased injection of charge carriers into the emission layer. Thus, more recombination is taking place and the light output is increased. However, the current efficiencies (Figure 4.8f) are hampered here by the sharply increasing current density resulting in a decreased efficacy for printed flexible devices. This is most likely caused by the overall higher roughness of the PET substrate compared to glass. Combined with the high crystallinity of the printed silver, this can result in more shorts in the device, reducing the efficiency. EL spectra of both device types were again recorded (inset Figure 4.8e) and show no substantial difference between Ag and ITO. Again, the electroluminescence maximum λ_{max} was found to be at 550 nm, corresponding to the CIE coordinates in Table 4.2.

Table 4.2. Turn-on voltage V_{on}, luminance L, current efficacy η_c, and CIE coordinates of glass and PET OLEDs.

Electrode	V_{on} (V)	Peak L (cd m^{-2})	η_C (cd A^{-1}) @ L (cd m^{-2})			Peak η_C (cd A^{-1})	CIE1931	
			100	1000	10 000		x	y
ITO	2.5	16 636	0.78	3.00	4.43	4.54	0.41	0.55
Silver	2.5	11 983	1.26	2.63	5.13	5.34	0.42	0.53
Flex ITO	3.0	3890	0.52	1.92	-	2.71	0.42	0.53
Flex Ag	2.5	2170	0.43	0.79	-	0.89	0.43	0.55

4.1.7 Flex-to-Install Application

Bending tests were carried out to verify the possible application of printed electrodes in flexible electronics. While the electrodes themselves have already been subjected to bending stress in section 4.1.4, devices also are required to exhibit a certain degree of flexibility for flexible applications. As most failures in bent devices occur due to cracking of the ITO layer,[169] OLED devices were fabricated, implementing pre-bent electrodes. For this, electrodes were subjected to 10 bending cycles with a 2% cyclic strain prior to device fabrication. The JVL characterizations in Figure 4.9a and b represent the results of these bending tests. Compared to OLEDs with fresh ITO layers, the ones utilizing pre-bent electrodes show a nearly ohmic behavior with highly increased current density values, hinting at the creation of shorts during the bending procedure. Ag devices were able to retain their functionality with only a minor increase in current density. While the brightness of the Ag devices does not change significantly as well, ITO devices lose up to 99% of their maximum luminance when pre-bent electrodes are used.

However, not every flexible application requires the electrodes to endure repeated bending stress. In so-called flex-to-install applications, the device is bent only once during the fabrication or installation process.

To compare the printed silver and ITO electrodes under this aspect, completely manufactured devices were subjected to increasing bending angles during operation. ITO devices were bent until total failure to determine the "critical angle of operation". This was found to be approximately at 30°. In a second step, OLEDs with printed silver electrodes were characterized and subsequently bent to this angle (see inset in Figure 4.9d). Compared to ITO, printed Ag devices retained full functionality. After bending JVL characterization of the OLED was repeated. Figure 4.9c and d compare the characteristics of an Ag OLED before and after bending to the critical angle of ITO. As can be clearly seen no significant change in behavior was observed with only a 2% loss in terms of maximum luminance.
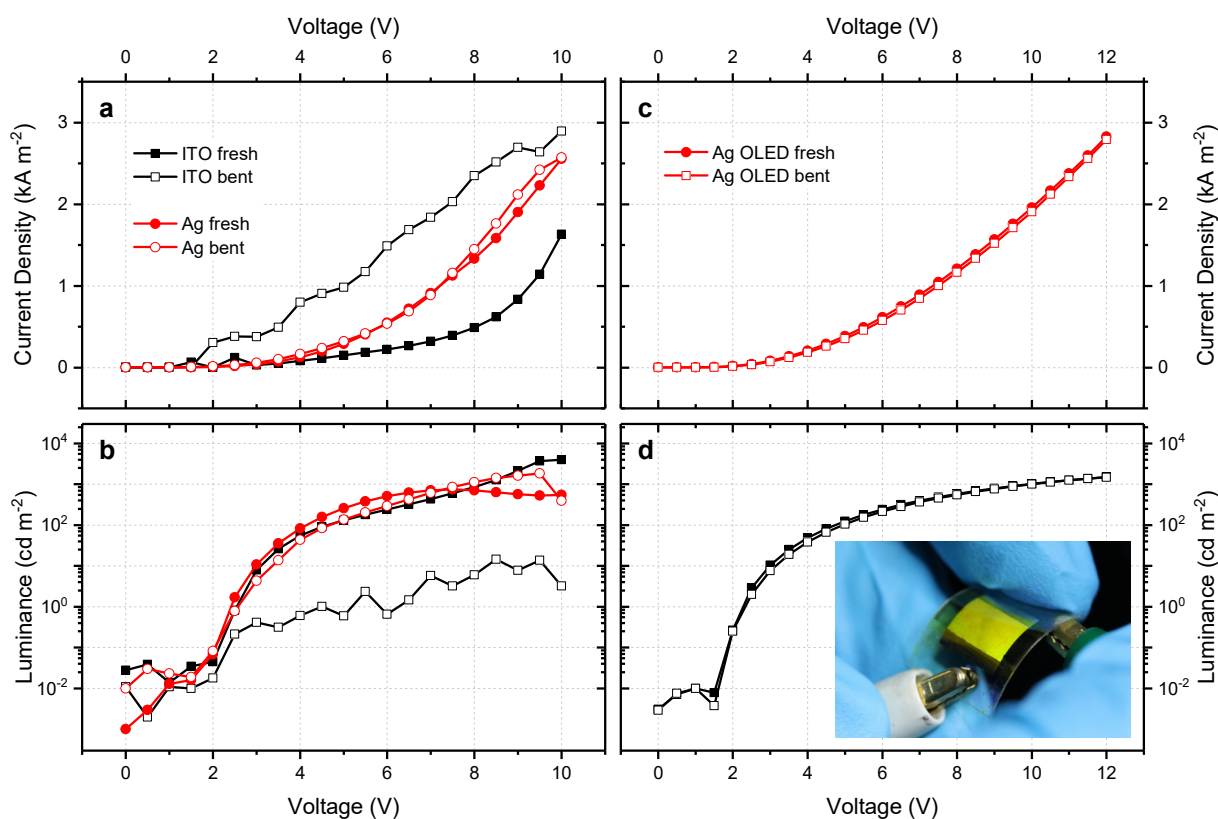
Figure 4.9. JVL characterization for bending tests. OLEDs made with pre-bent substrates (a, b) and bending finished devices (c, d). In contrast to ITO, which loses over 99% of its maximum luminance, pre-bent silver electrodes preserve their performance. At an approximate bending angle of 30° ITO devices fail, while Ag OLEDs at the same bending angle keep working with minimal performance loss of 2% in terms of luminance.

4.1.8 Conclusion for Printed OLEDs

To conclude, it could be shown that printed silver electrodes can be a viable alternative to the standard ITO substrates. A particle-free MOD ink was used to obtain semi-transparent silver layers exhibiting a good compromise between transparency (> 75% over the whole visible spectrum) and conductivity. When subjected to bending tests, these electrodes show highly resilient behavior compared to the brittle ITO.

Organic light-emitting diodes could be fabricated utilizing these electrodes and were shown to surpass ITO-based diodes reaching luminance values up to 10 000 cd m^{-2}. Fabricating silver electrodes on flexible substrates yielded OLEDs showing comparable characteristics to ITO reference devices. However, when bending both OLED types, superior bending stability could be shown for printed electrodes. This fact makes them highly interesting for flexible or flex-to-install applications.

So far, in this chapter, only printed silver electrodes have been implemented in OLEDs. As not all materials are compatible with this type of electrode due to ion migration or due to their high acidity which would attack the silver electrode, alternatives were next investigated.

4.2   Solution-Processed Gold Electrodes

As shown in the last section, thin layers of silver can be a suitable approach to replace ITO as a transparent conductive electrode. However, silver as a material has some disadvantages as it is very prone to oxidation. The oxides are not only known to exhibit a decreased conductivity compared to pristine silver but are considered semiconductor materials and thus not suitable as an electrode material. [170] Therefore solution-processed gold has been investigated as an alternative, more resistant electrode material.

A particle-free MOD ink was again used as the starting material for the production of the gold electrodes. Due to the ink's elevated acidity, it could not be used with the inkjet without damaging the printhead but was instead processed by doctor blading. The inks were again provided by OrelTech GmbH. After solution processing, the samples were dried in a vacuum chamber and reduced to metallic silver by applying an Ar plasma with a gas flow of 30 sccm and plasma power of 150 W for 10 min. All other processing and characterization steps were performed according to the descriptions in section 4.1.2.

By varying the processing parameters, gold films with a thickness of 28 nm and 48 nm were produced. Optical characterization via UV-Vis shows a decreased transmission when compared to the silver layers from the previous section. Layers with 28 nm film thickness exhibit a transmission maximum of 70% and an average transmission of 65% over the whole visible spectrum. At a thickness of 48 nm, these values change to 55% maximum and 50% average transmission as can be seen in Figure 4.10a. Compared to the printed silver layer, the gold transmits light not as linearly over the visible spectrum. Due to the yellowish color of the gold, visible in the optical image in Figure 4.10b, the blue wavelengths get more attenuated.

Electrical properties were tested by measuring the sheet resistance which was found to be a good value of 26 Ω sq^{-1} for the 48 nm film but strongly decreased for the 28 nm film with a sheet resistance of 10 MΩ sq^{-1}. This comes as no surprise, as the electrical conductivity of gold is 4.11·10^7 S m^{-1} while the previously used silver is the best conducting metal with a conductivity of 6.30·10^7 S m^{-1}.[171]
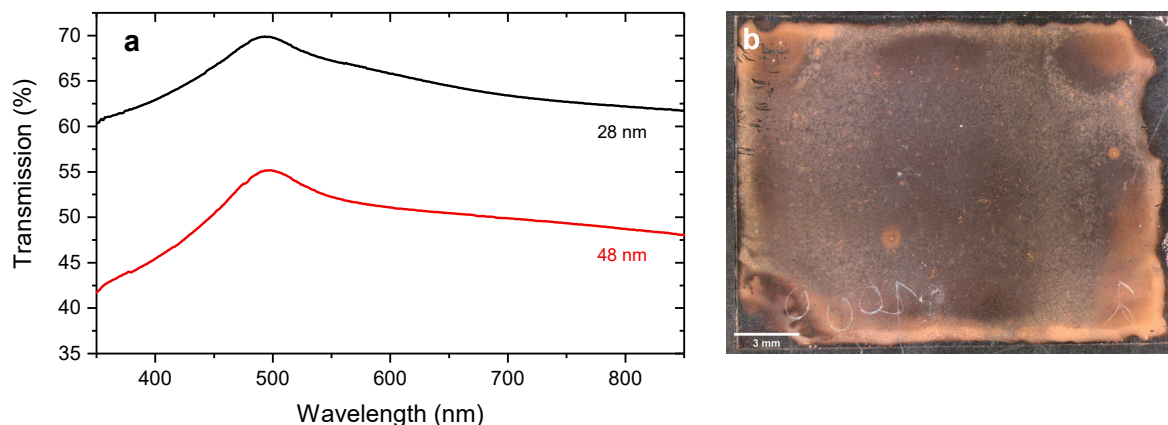
Figure 4.10. Optical characterization of the gold layer. (a) UV-Vis measurement of samples with different thicknesses. With increasing layer thickness, the transparency rapidly decreases. (b) Optical image of a doctor-bladed sample.

Figure 4.11. Morphological characterization of a doctor-bladed gold layer. (a) The optical microscope image shows individual gold crystals with a strongly increased height compared to the silver layer. (b) SFM image displays the same structures. The overall higher layer thickness improves conductivity but reduces the optical transparency of the sample. (c) height profile extracted from (b).

Similar to the silver layer produced previously, the morphology of the gold layer was examined more closely in order to be able to draw conclusions about the gold's optical and electrical properties. SFM as well as optical microscopy pictures are displayed in Figure 4.11. The crystalline structure is again clearly visible. However, in contrast to the silver layer, the gold exhibits a more densely packed, closed crystal structure that lets less light pass through. In more detail, the SFM image reveals very high ridges and a more uneven profile. The roughness R_a of the sample with a thickness of 48 nm was found to be 8 nm and the 28 nm sample showed a roughness of 6 nm. SEM images displayed in Figure 4.12 support these findings, showing a very crystalline, closed surface in the top view as well as the cross-section view.
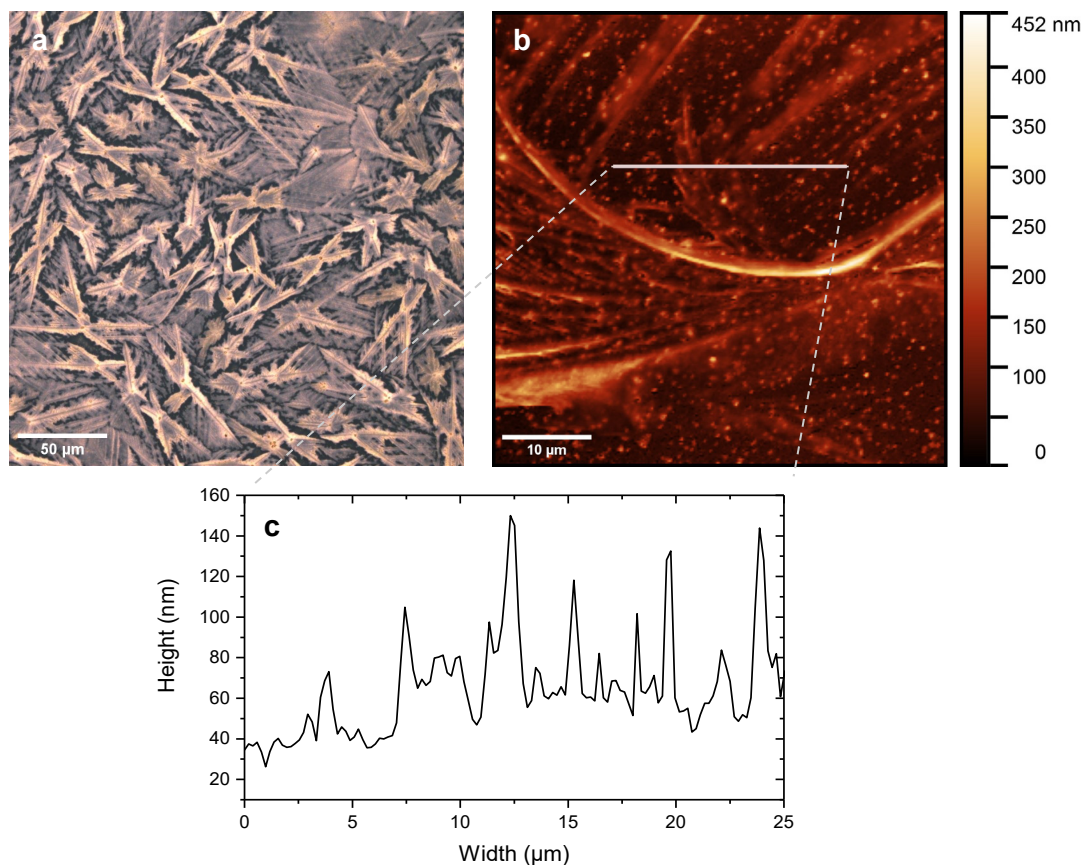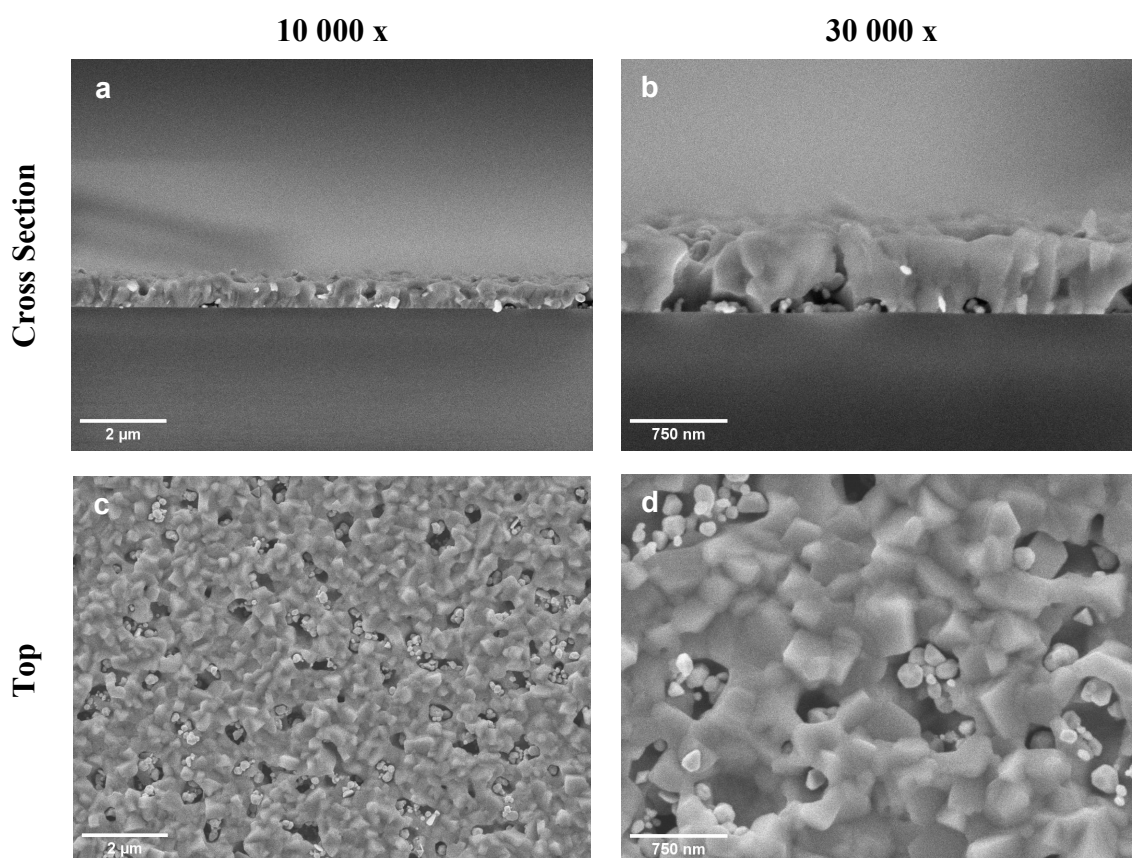

Figure 4.12. SEM images of a doctor-bladed gold layer with a thickness of around 750 nm. The crystalline structure of the gold is visible. The top row (a, b) shows a cross-section in different magnifications while the bottom row (c, d) displays a top view.

As a proof of concept, bottom-emitting inverted OLEDs were fabricated. Electrodes were manufactured by doctor blading the gold MOD ink. Standard JVL and EL characterizations were performed as previously described. The results of these measurements are presented in Figure 4.13.

Compared to OLEDs containing silver electrodes, gold OLEDs exhibited a lower current density. Regarding the lower conductivity of gold in comparison to silver, this is an expected effect. In terms of luminance, the OLEDs were able to obtain a maximum brightness of 1200 cd m^{-2}, significantly less than their silver counterpart. This can be attributed to the lower

transparency of the gold electrode. The electroluminescence spectrum in Figure 4.13b, however, exhibits no shift or broadening compared to silver, the spectral maximum remains at 550 nm. The turn-on voltage remained at 2.5 V, again indicating that no additional injection barriers are present. Since the luminance was lower, the current yields were also significantly reduced with a maximum of only 0.94 cd A.

It must be mentioned that although working OLEDs were obtained, many of the devices produced showed resistive behavior. The high spikes in the gold layers most likely were causing short circuits in the devices, severely degrading their performance, or causing device failure.
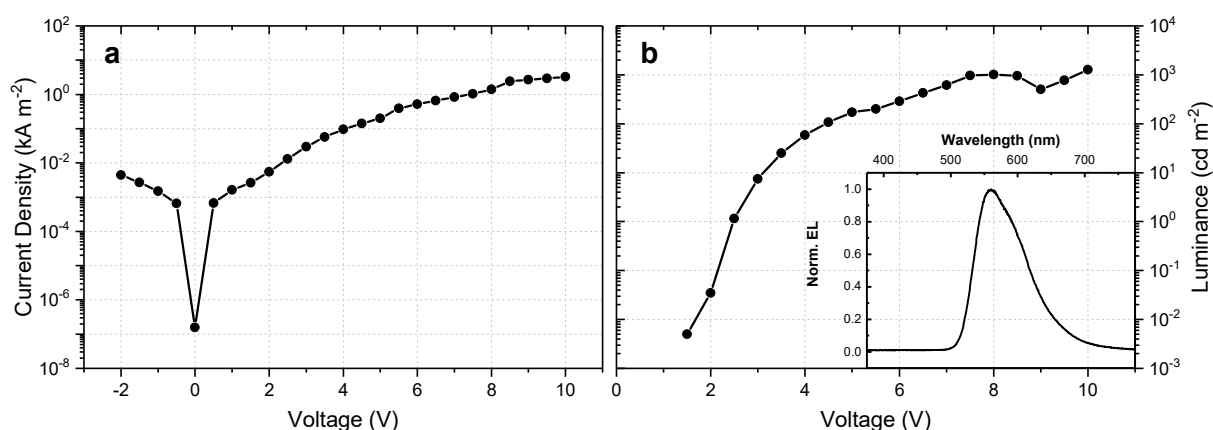
Figure 4.13. JVL characterization for an OLED with a proof-of-concept gold electrode. (a) As can be seen in comparison to the results of silver OLEDs (see Figure 4.8), less current flows. (b) Combined with the lower transparency of the gold, the luminance is reduced by about an order of magnitude. Nevertheless, functioning OLEDs are possible with gold electrodes. The inset in (b) shows the EL spectrum. No difference in the EL could be observed here.

4.2.1 Conclusion for Gold Electrodes

To conclude, it could be shown that it is possible to use gold as an alternative electrode material for OLEDs. As with silver, a particle-free MOD ink was employed to obtain conductive, transparent electrodes. While doctor-bladed films showed decreased transparency (50% over the whole visible spectrum) and conductivity compared to silver, they could be still successfully incorporated into OLEDs.

Devices showed promising first results with luminance values up to 1200 cd m^{-2} and efficacies of around 1 cd A. However, improvements have to be made while fabricating the electrodes to avoid the presence of high features in the gold electrode which otherwise results in lowered device performance.

While the proof-of-concept OLED with a gold electrode could be shown in this work, the next step of incorporating the electrode into OLEDs or solar cells, containing materials not compatible with silver, was unfortunately not possible in the limited timeframe of this thesis.

5 Enhancement of Surface Properties by Injection- and Interlayers

Optoelectronic devices can have a rather simple composition of just an emission or absorption layer sandwiched between two electrodes. However, this architecture yields devices of low efficacy due to multiple loss mechanisms. Injection layers, to facilitate the injection of charge carriers, as well as interlayers, to enhance transport or improve surface properties, can significantly increase device performance. In this chapter, these two different strategies are discussed.

Firstly, an injection layer made from a zinc oxide and polyethylenimine mixture is characterized. The influence of different processing parameters on device efficacy is investigated by fabricating OLEDs with differently manufactured interlayers.

Secondly, two novel molecules are analyzed as possible interlayer candidates to improve he surface properties of substrates. Their chemical, optical and electrical properties are evaluated and their ability to enhance surface properties is assessed by fabricating perovskite solar cells.

5.1 ZnO:PEI Blends for Interlayer Functionalization

5.1.1 Introduction

Organic light-emitting diodes usually employ top electrodes made via physical vapor deposition of metals. Since the top electrode is responsible for injecting electrons into the emissive layer in a standard (non-inverted) OLED structure, low work function materials such as calcium, magnesium, or lithium fluoride have to be employed.[172,173] However, the oxygen and moisture sensitivity of these materials would lead to quick degradation of the device.[174,175] Therefore, calcium and lithium fluoride are covered by less sensitive metals like silver. Finished devices are encapsulated and device fabrication is usually performed under an inert atmosphere.

Changing the device structure to an inverted architecture can alleviate some of these issues by removing oxygen-sensitive materials. In this structure, the top electrode injects holes into the device, therefore, high work function buffer materials such as the oxides of tungsten, vanadium, or molybdenum have been employed in combination with a silver top layer.[176–178]

With that, however, the issue of electron injection on the cathode side of the device does not get resolved. Electrons still need to be injected, now from the ITO electrode which has a relatively high work function, varying between 4.1 eV and 5.5 eV.[179] An electron injection layer (EIL) or a method of lowering the work function of ITO is therefore highly beneficial to increase the device performance. Recent studies have shown that polymer materials and self-assembled monolayers can be used as an efficient work function modifier, lowering the work function of ITO by introducing interface or molecular dipoles on the surface.[180] Zhou et al employed the polymer polyethylenimine (PEI) to successfully reduce the work function of ITO to 3.5 eV.[166] Metal oxide films such as zirconium, titanium, and zinc oxides have been used as EIL.[181–183] A combination of the two approaches has also been investigated before, resulting in highly efficient inverted OLEDs.[184]

In his bachelor thesis, Andreas Mai investigated mixing the two materials to facilitate the production of inverted OLEDs.[185] This chapter is a continuation of his findings. Although the blending of zinc oxide (ZnO) and PEI has already been previously reported in literature,[186] a thorough investigation of the processing parameter is still lacking, which shall be provided here.

5.1.2 Materials and Experimental Setup

Solution Preparation: A solution of the PDY-132 Super Yellow (SY) light-emitting polymer (Sigma-Aldrich) was prepared by dissolving the polymer at a concentration of 5 mg ml^{-1} in toluene. Zinc acetylacetonate hydrate (Zn(acac)$_2$, Sigma-Aldrich) was dissolved at a concentration of 20 mg ml^{-1} in ethanol. Prior to application, these solutions were stirred for several hours on a hotplate at 50 °C. The Zn(acac)$_2$ solution was filtered before being used. Zinc oxide (ZnO) nanoparticle solutions (Genesink, 1% ZnO nanoparticles, dispersed in isopropanol, variable particle sizes) were used as received. PEI (Sigma Aldrich, $M_W = 25\,000$ g mol^{-1}) was dissolved in toluene to achieve a 0.4 wt% solution according to literature.[166]

Sample Preparation: Patterned ITO substrates (Psiotec Ltd.) for device preparation and glass substrates for energy level analysis were cleaned by thoroughly wiping them with acetone and isopropanol. Afterwards, a 5 min O_2 plasma treatment in a Femto plasma system (Diener) at a gas pressure of 0.35 mbar and 500 W of power was used to activate the sample surface before solution deposition. For the PYS analysis, PEI, ZnO, and mixtures were spin-coated at different speeds and annealed on a hotplate at 100 °C for PEI and 120 °C for ZnO and mixtures.

Ionization Potential Analysis: An AC2 photoelectron yield spectrometer by Riken Keiki was used to determine the ionization potential of the prepared samples with photon energies between 4.2 and 6.2 eV. Data evaluation was done manually by linear fitting the data.

Device Preparation: ITO substrates were prepared as described above. PEI, ZnO, or mixtures of both were then spin-coated at different speeds and dried on a hotplate at 100 °C for PEI and 120 °C for ZnO and mixtures. The SY emitter was spin-coated at 2500 rpm, resulting in an 80 nm film. All solution processing was performed in ambient conditions. The top electrode of 10 nm of MoO_3 and 200 nm of silver was evaporated thermally under vacuum with a base pressure of 10^{-6} mbar. The usage of a shadow mask resulted in devices with an active area of 0.04 cm^2. Finally, devices were encapsulated using glass slides and UV-curable resin (Ossila) and cured at 365 nm for 10 min.

Device Characterization: Electrical characterization was performed by measuring current density-voltage-luminance curves with a Keithley 2612B source meter and a Konica Minolta LS-160 luminance meter with a purpose-built setup (detailed description in section 3.2.10). EL spectra were recorded with a CS 2000 spectrometer (Ocean Optics) using OceanView software.

5.1.3 ZnO Fabrication, Particle Size, and Volumetric Ratio

Mostly, ZnO nanoparticles have been prepared from zinc precursors in a vast range of different shapes and sizes.[187,188] As a first step it was tested if good device performance could be achieved with a ZnO layer made from the $Zn(acac)_2$ precursor as described in literature.[189] OLEDs with a ZnO layer and a separate PEI layer were produced and analyzed. JVL analysis resulted in low luminance values of only 500 cd m^{-2} and current efficacies of 0.06 cd A^{-1} as is displayed in Table 5.1. Therefore, a commercial ZnO nanoparticle (NP) suspension in isopropanol was investigated for further experiments.

To demonstrate the influence that injection and interlayers made from ZnO nanoparticles and PEI can have on the OLED efficacy, OLEDs were produced including one or multiple of these layers. Devices with no interlayer between the ITO and the SY emitter were tested as well but these devices did not result in working devices, demonstrating the importance of appropriate energy levels. The resulting current density and current efficacies for four different EIL combinations can be seen in Figure 5.1 and Table 5.1. With only a layer of zinc oxide nanoparticles, higher current densities could be reached, resulting from a lowered injection barrier). However, higher leakage currents (suggesting an insufficient hole blocking of ZnO) were observed in the devices at negative voltages. The turn-on voltage for this device type was measured to be 2.5 V, as expected for the SY material (which has a bandgap of 2.4 eV).

The leakage current is greatly reduced when only a thin PEI layer is included demonstrating its ability to not only modify the work function of materials but also to block unwanted charge carriers. Zhong et al attribute this to the presence of tertiary amine groups in the PEI backbone.[190] However, due to its insulating nature, the turn-on voltage is shifted to 4.0 V and the whole current density curve is lowered. With a maximum of only 825 cd m^{-2}, the luminance values of the pure PEI devices, are significantly lower compared to all other combinations. Adding both a ZnO and PEI layer subsequently (denoted as ZnO/PEI) returns the turn-on to 3.0 V while keeping the leakage currents lowered. Using a blend of ZnO and PEI (denoted as ZnO:PEI) returns the turn-on to its desired value of 2.5 V, again, retaining the lowered leakage current. For all EIL combinations tested, the EL signal remained constant with a maximum at a wavelength of 560 nm (see inset in Figure 5.1b).
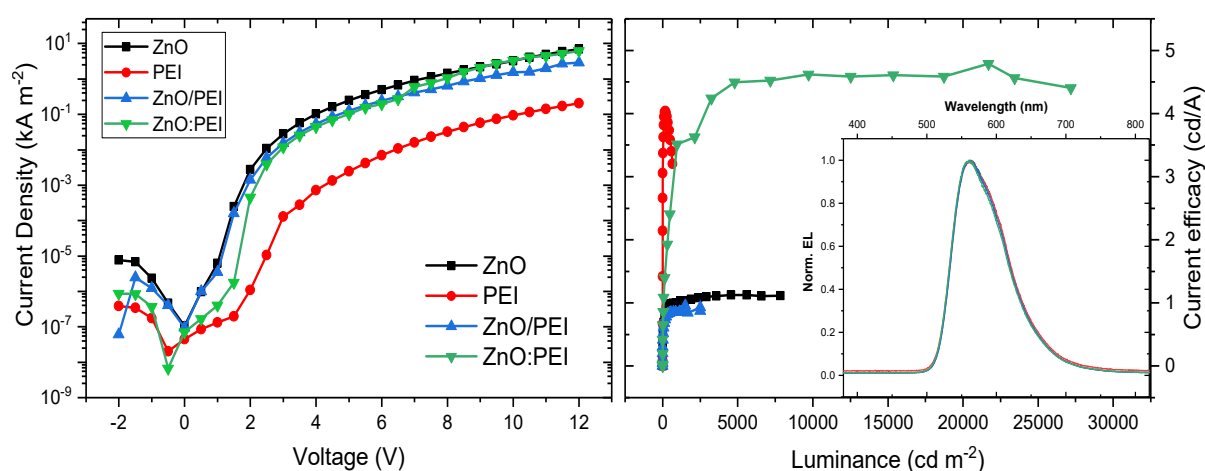

Figure 5.1. JVL characteristics of inverted OLEDs with different EIL material combinations. (a) Current Densities. (b) Current Efficacies. As can be seen, the efficacy is highly increased when a ZnO:PEI blend is utilized. The inset in (b) shows EL spectra recorded at 1000 cd m^{-2}. No shift in emission color could be determined.

Regarding the efficacies of the fabricated devices in Figure 5.1b, pure ZnO devices exhibit low efficacies with a maximum of 1.12 cd A^{-1}. In contrast, using a PEI layer leads to significantly increased efficiencies with values of 4 cd A^{-1} which can be attributed to the improved minority charge carrier injection into the emitter by the PEI. However, pure PEI devices show an immediate efficacy roll-off after the maximum at 4 cd A^{-1} hinting at a strong charge carrier imbalance at higher luminance values. For ZnO/PEI devices a low efficacy of only 1 cd A^{-1} was found. Surprisingly, this is even lower than the pure ZnO devices. A possible explanation is the partial dissolution of the underlaying ZnO layer by the isopropanol PEI solution which leaves a ZnO and PEI layer with an undefined thickness. This is a well-known problem with multilayer devices fabricated by solution processing and will be further investigated in chapter 6. Blending ZnO and PEI (2:1 by volume) results in the best performing OLEDs. Efficacies of up to 4.5 cd A^{-1} could be achieved suggesting good electron injection as well as hole blocking abilities of the composite material with a vastly improved efficacy roll-off, due to an improved charge carrier balance in the emitter material. External quantum efficiencies exhibit the same trend with the ZnO:PEI blend outperforming other EILs, reaching an EQE of 0.96%.

Table 5.1. Turn-on voltage V_{on}, maximum luminance L, current efficacies η_c, external quantum efficiencies η_E measured at 1 and 10 mA, and CIE coordinates of OLEDs containing different electron injection layers. All JVL values are averaged over at least four pixels.

EIL	V_{on} (V)	Peak L (cd m^{-2})	Peak η_C (cd A^{-1})	EQE η_E (%) @ I (mA)		CIE1931	
				1	10	x	y
none	-	-	-	-	-	-	-
ZnO	2.5	8 952	1.12	0.23	0.29	0.47	0.51
PEI	4.0	825	4.00	0.59	0.64	0.47	0.51
ZnO/PEI[a]	3.0	2354	1.00	0.18	0.24	0.47	0.51
ZnO:PEI[b]	2.5	26 800	4.54	0.78	0.96	0.47	0.52
Zn(acac)$_2$/PEI[a]	3.0	495	0.06	0.04	0.03	0.46	0.52

[a] Subsequently fabricated layers; [b] Single layer from a binary 2:1 mixture

Up to this point, the ratios of ZnO and PEI (2:1) in the composite mixture have been chosen based on the assumption that the insulating PEI should result in only a very thin film, while the ZnO should improve the electron transport. To validate this hypothesis a series of OLED devices with different ZnO:PEI ratios were fabricated and characterized. The turn-on voltage (dependent on the injection barrier), maximum luminance, and maximum current efficacies (influenced by the charge carrier balance and the hole-blocking ability of the EIL) were compared and are displayed in Figure 5.2.
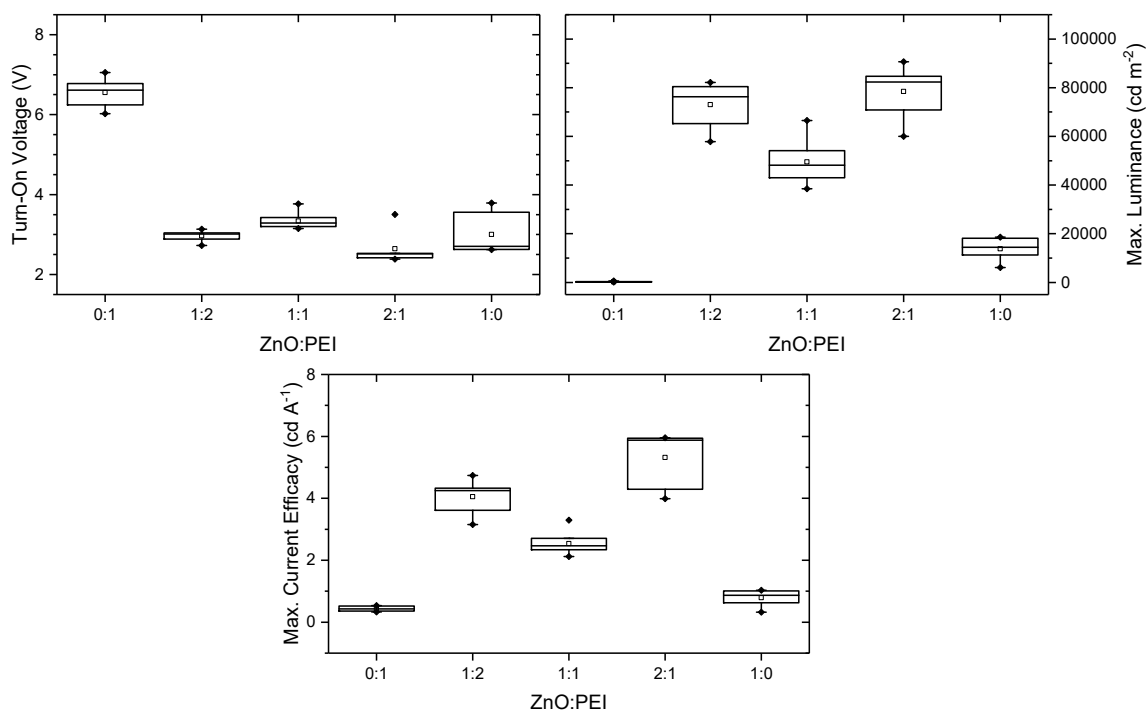

Figure 5.2. JVL evaluation of OLEDs prepared with different ratios of ZnO:PEI. Combining ZnO and PEI in an OLED results in a significant increase in luminance as well as current efficacy. The OLED turn-on is strongly decreased when adding a ZnO electron injection layer. Square points indicate the mean values.

In accordance with the previous results, a pure PEI layer leads to a very high turn-on voltage, while the addition of any ZnO lowers it significantly. Luminance values of ZnO:PEI mixtures display greatly improved values over pure ZnO or PEI layers. Efficacies follow the same trends exhibiting the best results for the 2:1 mixture with an average of 5.5 cd A^{-1}. Higher percentages of ZnO were tested as well, however, no further gain in efficacy could be achieved. It was therefore concluded that the previously only assumed optimal ratio of 2:1 by volume ZnO:PEI was indeed ideal for the employed device architecture. To investigate if different ZnO:PEI ratios change the ionization potential of the sample, PYS measurements were carried out. All interlayers displayed a reduction of the ITO ionization potential (Φ_{ITO} = -4.8 eV) with pure PEI showing the strongest effect (Φ_{PEI} = -5.4 eV) while the 1:1 mixture exhibits the weakest effect ($\Phi_{1:1}$ = -4.9 eV).

The ZnO-to-PEI ratio is not the only parameter thought to have an impact on device performance. Since films should preferably have a smooth surface with an even distribution of nanoparticles, the particle size can be another important fabrication parameter. The commercial ZnO nanoparticle suspension used in this work is available with different NP sizes ranging from 8 nm to 30 nm. In a second test, the experiments from the aforementioned ratio series were repeated, this time with a constant ZnO:PEI ratio of 2:1 by volume, using different NP size suspensions. Figure 5.3 gives the results for the turn-on voltages, the maximum luminance values, and maximum efficacies.
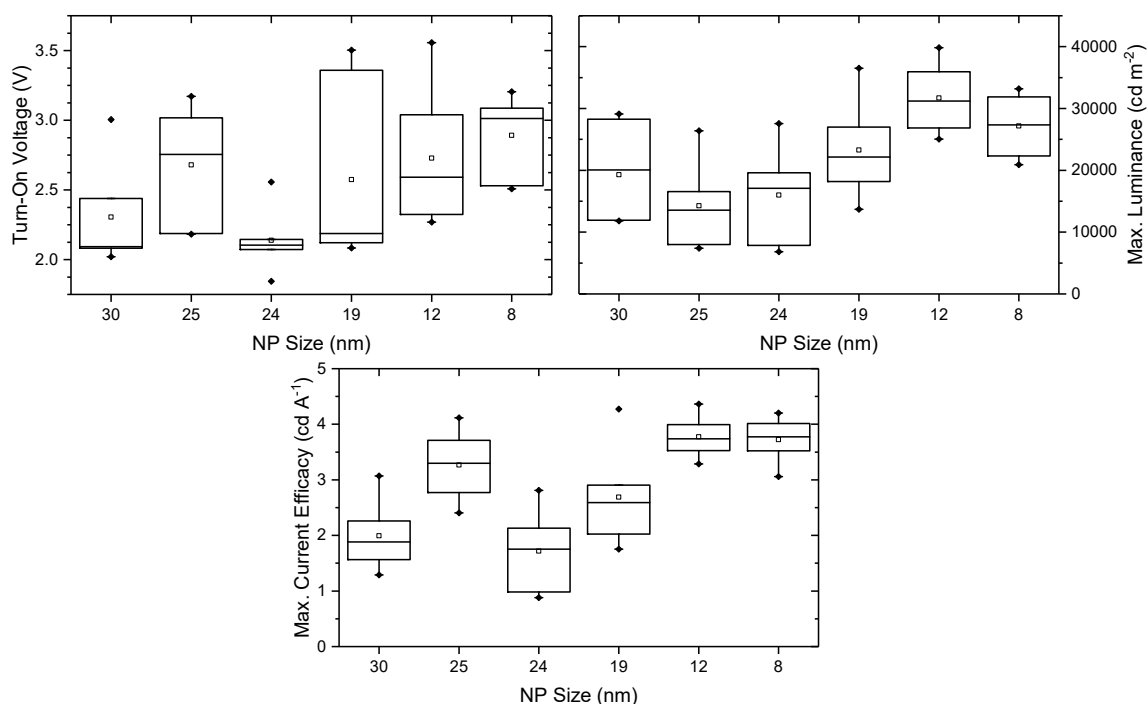

Figure 5.3. JVL evaluation of OLEDs prepared with varied sizes of ZnO nanoparticles in the ZnO:PEI layer. Lower nanoparticle sizes result in more efficient OLEDs. ZnO:PEI ratio was 2:1 by volume.

Since now the 2:1 mixture was used, the turn-on voltages show a significantly lower range of values. For all NP sizes they were found to be between 2.0 V and 3.5 V. In contrast to that, the luminance values fluctuate significantly with varying NP sizes. Generally, smaller NP sizes seem to lead to brighter OLEDs. However, the smallest size of 8 nm exhibits lower luminance values of up to 3200 cd m^{-2} than the 12 nm ZnO (luminance up to 4000 cd m^{-2}). Pu et al. also studied the shape and size of ZnO nanoparticles and found that, up to a certain size, smaller NPs show better device performance, consistent with the results presented here.[183] This is attributed to the fact that larger nanoparticles lead to a rougher surface morphology, which consequently results in poorer electrical contact with neighboring layers. Regarding the efficacies, it again can be seen that lower NP sizes lead to an improvement in efficacy. The 12 nm device slightly outperforms the 8 nm device. From these experiments, it was therefore concluded that a ZnO nanoparticle size of 12 nm was optimal for the utilized device structure.

As a final step, the ZnO layer thickness was also examined. This parameter is directly influenced by the spin coating speed (see also section 3.1.2) which was therefore varied between 1500 rpm and 5500 rpm. Again, the turn-on voltages, the maximum luminance values, and maximum efficacies were recorded and compared. The results are shown in Figure 5.4
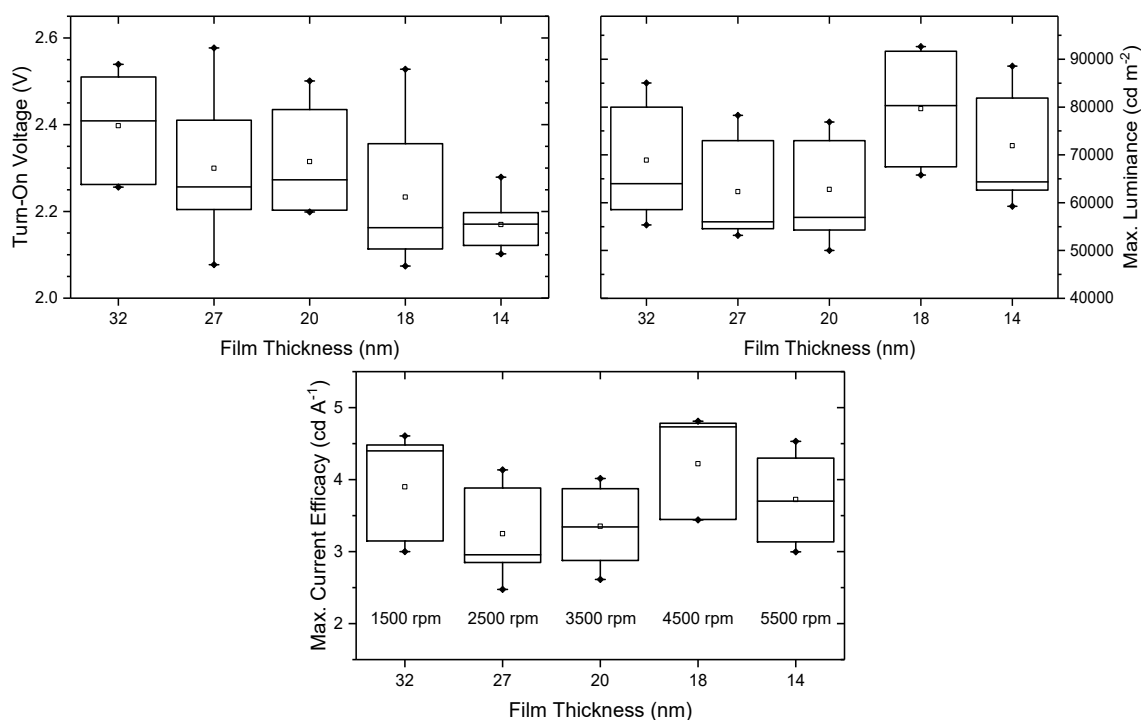

Figure 5.4. JVL evaluation of OLEDs prepared with different spin coating speeds when fabricating the ZnO:PEI layer. A higher spin speed and consequentially lower film thickness led to higher-performing devices. A film thickness of 18 nm (speed of 4500 rpm) could be determined as the optimum. The spin speeds of the different layers are added to the efficacy diagram.

The turn-on voltages showed a decreasing trend as the spin speed was increased. This makes sense since the EIL including the insulator PEI also decreases in thickness. The thickness values were determined for each spin speed and are shown in Figure 5.4. For the maximum luminance, a thickness of 18 nm results in the highest values of 9200 cd m^{-2}. The reduced luminance at 14 nm (max. 8200 cd m^{-2}) is most likely caused by an interlayer that is too thin and is now no longer able to sufficiently modify the interface work function. In the case of the device efficacies, the same trend is visible where an 18 nm thickness (rotation speed of 4500 rpm, respectively) yields the best results with a maximum value of 4.8 cd A^{-1}. From these experiments, it was concluded that 18 nm is the optimal interlayer thickness.

5.1.4 Conclusion for ZnO:PEI

In this section, the production parameters for spin coating a ZnO:PEI layer were investigated. It was found that solution processing from a composite solution results in OLEDs with better performance. Nanoparticle ZnO solutions were able to outperform solutions produced from a Zn(acac)$_2$ precursor, reaching up to 4.5 cd A^{-1} in terms of efficacies. For the manufacturing parameters, it could be determined that a ratio of 2:1 ZnO:PEI, a ZnO particle size of 12 nm, and an 18 nm layer thickness (fabrication speed of 4500 rpm) resulted in the best-performing OLEDs.

5.2 Novel Molecules for Improved Wetting

5.2.1 Introduction

Interlayers between the electrodes and emitter materials are crucial ingredients for highly efficient OLED devices. As could be demonstrated for the case of a ZnO:PEI layer in the previous section, luminance values and efficacies were significantly increased. But not only OLEDs but also solar cells benefit from interlayers, in this case, to maximize the extraction of charge carriers from the active material. In perovskite solar cells (PSC) the active layer, also called the light-harvesting layer, is usually made from a compound, lead-organic-based perovskite structure.[191,192] As previously described (see section 2.4.1) for OLEDs, the simplest approach of an active layer between two electrodes is, although functional, not very efficient, due to energy level mismatches of the layers. Hole and electron transport layers as well as charge extraction layers can be included in the solar cell structure to drastically enhance device performance. These additional layers need to be matched in their energy levels to those of the perovskite to facilitate charge carrier extraction. They can be made out of different materials like organic molecules, polymers, or metal oxides.[193–195]

The de-facto standard material for hole transport in perovskite devices has long been the conductive polymer PEDOT:PSS.[196,197] However, due to its better energy level alignment with the perovskite layer, Poly[bis(4-phenyl)(2,4,6-trimethylphenyl)amine (PTAA) has replaced

PEDOT:PSS in more recent research.[198] Although this change was able to improve the open-circuit voltage of solar cells, owing to more suitable energy level alignment and better charge carrier transport, the fill factor was lowered. [199]

Unfavorable perovskite growth with smaller grains, leading to more recombination at grain boundaries is thought to be one of the reasons for the decrease in fill factor.[200] This can be caused by improper wetting of the perovskite when processed on the PTAA. Since PTAA is a strongly hydrophobic polymer, as a result of it being nonpolar with low surface energy, the polar solvents used to process the perovskite (mostly N,N-dimethylformamide, dimethyl sulfoxide, or mixtures of both) are unable to adequately wet the PTAA layer.[201,202] Especially when scaling the production methods from small-scale spin coating to more scalable techniques such as roll-to-roll processing or inkjet printing, this quickly becomes the limiting factor in terms of perovskite film quality.[203]

Multiple solutions for this problem have been proposed. Wetting can be improved by the addition of surfactants such as aluminum or silicon oxide nanoparticles.[204,205] UV-Ozone plasma treatment was applied as well to improve the wetting of perovskites on PTAA.[206] However, this process can easily degrade the PTAA and change its optical and electrical properties.[207] Mixing PTAA with other, more polar molecules or polymers has been suggested as well.[208]

The ongoing search for materials with better wettability, while maintaining suitable energy levels for perovskites, has also led to the development of novel materials. In this section, two novel molecules are discussed. These molecules were synthesized by Prof. Milan Kivala and his group at Ruprecht-Karls-Universität Heidelberg. Starting from the well-known molecules triphenylamine (TPA) and trinaphthylamine (TNA), polyethylene glycol (PEG) has been attached, resulting in the two molecules PEG-TPA and PEG-TNA (chemical structures are shown in Scheme 5.1). These were analyzed using a variety of different techniques to determine their electrical, optical, and wetting properties. Finally, perovskite solar cells were fabricated and characterized to evaluate their feasibility as a replacement for PTAA.
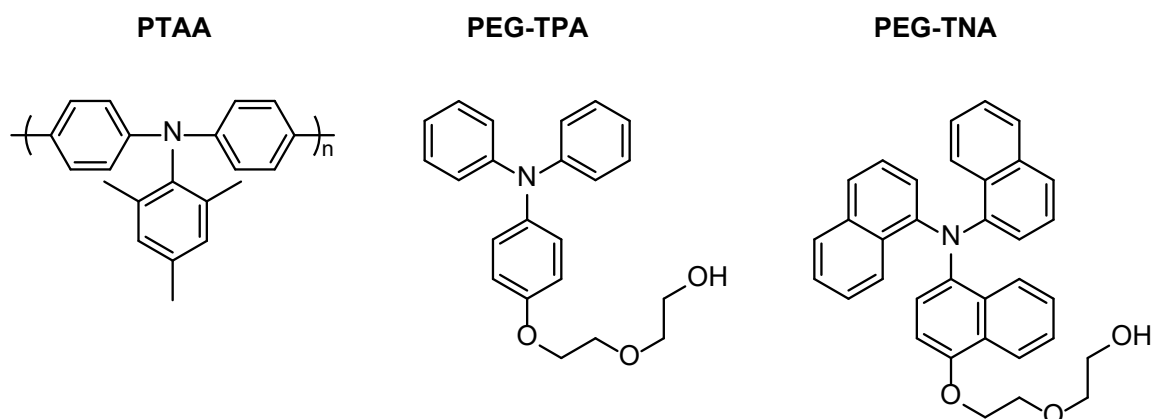
Scheme 5.1. Chemical structures of the utilized polymer PTAA and the two novel small molecules PEG-TPA and PEG-TNA.

5.2.2 Materials and Experimental Setup

Solution Preparation: Solutions of PTAA (Ossila, $M_W = 55\,000$ g mol^{-1}), PEG-TNA, and PEG-TPA were prepared by dissolving them at a concentration of 5 mg ml^{-1} in toluene. Solutions were stirred for 30 min at 60 °C prior to any processing step. Precursors for the triple cation perovskite were dissolved in a 4:1 mixture of N,N-dimethylformamide and dimethyl sulfoxide and stirred at 60 °C overnight. Perovskite solution was prepared by mixing the precursor solutions.

Sample Preparation: Glass substrates for SFM and contact angle analysis, quartz samples for optical characterization, and ITO substrates for energy level, morphology, and mobility measurements were prepared by cleaning them by sonication for 10 min with acetone and isopropanol. Before use, the sample surface was activated by a 5 min O$_2$ plasma treatment in a Femto plasma system (Diener) at a gas pressure of 0.35 mbar and 500 W of power. For all experiments, thin films were fabricated via spin coating at 2500 rpm with subsequent drying at 60 °C for 10 min on a hotplate. Printing of the perovskite ink was performed on a PiXDRO LP50 inkjet printer (Meyer Burger / Süss Microtec) using a Spectra S-Class printhead with a nominal drop volume of 30 pl.

Sample Analysis: Prepared samples were optically analyzed via a LEXT OLS4100 laser scanning microscope (Olympus). SFM images were recorded on a Bruker FastScan SFM in tapping mode. UV-Vis spectra were taken with a Perkin Elmer Lambda 950 double-beam spectrometer. Scanning electron microscopy images were recorded by the HZB SEM service.

Chemical and Energy Analysis: Chemical analysis was performed via XPS, and the energy levels of the samples were analyzed by UPS. Both measurements were made on a JEOL JPS 9030 photoelectron spectrometer. Ionization energy was determined by PYS on an AC2 photoelectron yield spectrometer by Riken Keiki with photon energies between 4.2 and 6.2 eV. Contact angle measurements were carried out on a Krüss DSA100 Drop Shape Analyzer and fitted using the OWRK method.

Device Preparation: Hole-only devices were prepared by firstly cleaning the samples as described above. PEDOT:PSS was then spin-coated on top at 1000 rpm for 12 s and then 2000 rpm for 30 s. Films were dried subsequently on a hotplate for 10 min at 220 °C. Thin films of PTAA, PEG-TNA, PEG-TPA, and mixtures were spin-coated at different speeds and annealed for 10 min at 60 °C. A top electrode of 7 nm of MoO$_3$ and 150 nm of gold was finally thermally evaporated before encapsulating the samples using glass slides and UV-curable resin (Ossila), which was cured for 10 min under 365 nm light. Solar cells were produced at the HZB HySPRINT labs by spin coating perovskite precursor solution (5 s acceleration to 3500 rpm, 35 s rotation at 3500 rpm). An anti-solvent drip of 250 µl of Anisole was applied after 25 s. Afterwards, the sample was annealed at 100 °C for 30 min. 23 nm of fullerene and 8 nm of bathocuproine were thermally evaporated on top, followed by an electrode consisting of 200 nm of copper. Devices were encapsulated with a glass slide and UV-curable resin (BLUFIXX).

Device Characterization: JV characterization was performed with a Keithley 2612B source meter with a purpose-built setup (detailed description, see 3.2.10). Solar Cells were measured with a sun simulator (Abet Technologies) at an illumination of 1 sun with an AM 1.5 filter.

5.2.3 Molecular Properties

Both novel molecules were received in powdered form. Since all characterization in this section relies on thin films, PEG-TPA was dissolved in toluene at a concentration of 5 g l^{-1} to fabricate solution-processed layers. However, it was determined that spin coating pure PEG-TPA did not result in fully closed films. Therefore, PTAA was added in varying concentrations hoping that its polymeric nature would allow hole-free layers to be processed. PTAA percentages of 5% or more resulted in closed surfaces as can be seen in Figure 5.5. A 95:5 (by volume) mixture of PEG-TPA:PTAA was therefore used for all further experiments. PEG-TNA was dissolved in toluene as well but resulted in closed films without further addition of PTAA. However, to be able to compare the two molecules, a mixture with 95:5 PEG-TNA:PTAA was also analyzed. All further experiments were performed on both molecules.
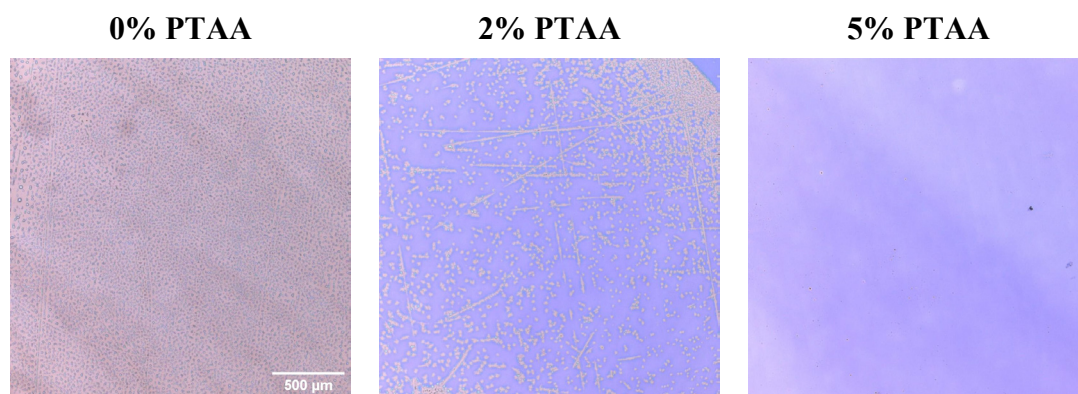
0% PTAA	2% PTAA	5% PTAA

Figure 5.5. Optical microscope images of PEG-TPA layers with different percentages of PTAA mixed in. Pure PEG-TPA samples and samples with 2% of PTAA added show no closed surfaces. This was confirmed by SFM measurements. The goal was a homogeneous film, as can be seen in the 5% sample.

Since the molecule to be examined is a newly synthesized one, a chemical analysis was first carried out via XPS. Thin films of the 95:5 mixture and a pure PTAA film were examined. For the pure PTAA sample only a signal at a binding energy of 284 eV and one at 400 eV could be found in the broad survey scans (see Figure 5.6). These two signals correspond to the carbon 1s (C1s) and nitrogen 1s (N1s) orbitals. Due to the PEG group in the PEG-TPA, an additional oxygen peak at 553 eV could be observed in the mixture sample. The carbon and nitrogen peaks were analyzed in more detail. As can be seen in Figure 5.7b and c, the nitrogen peak consists of a single signal, a result of the C-N bonds to the central nitrogen atom. In the PTAA sample, the carbon peak displays two contributions, a strong C-C/C-H signal as well as an expected weaker C-N signal. In the case of the mixture, deconvolution of the carbon peak revealed three contributing signals (Figure 5.7c): the same C-C/C-H and C-N signals as for PTAA and the additional C-O contribution from the PEG group. The deconvolution of the oxygen peak can be found in Figure 5.6. No additional signals from other elements were found, so it can be concluded that no by-products of the synthesis remain.
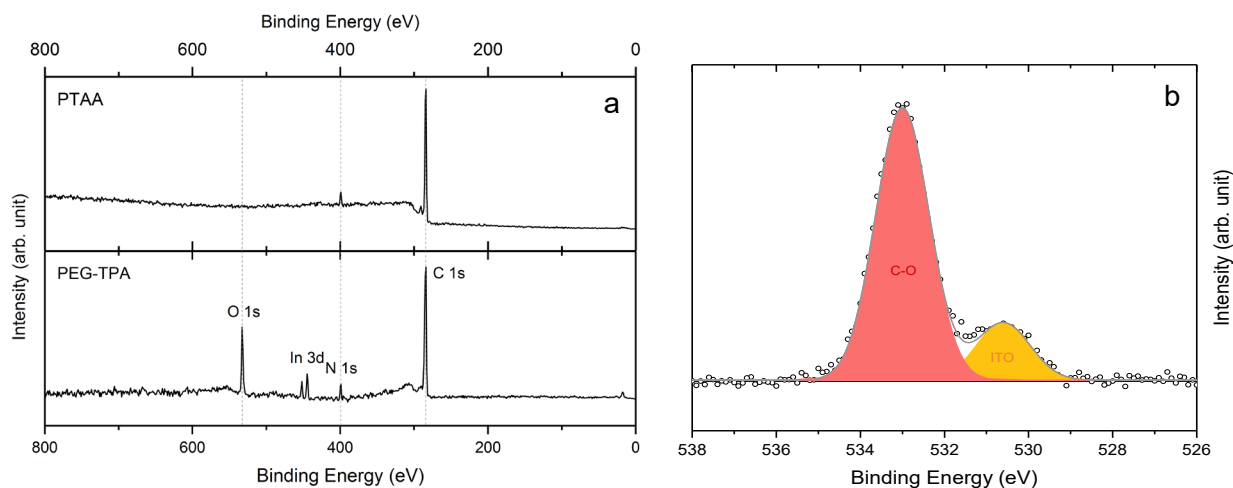
Figure 5.6. XPS elemental analysis. (a) Survey scans of PTAA and PEG-TPA. (b) Fine scan of the oxygen peak for a 95:5 mixture of PEG-TNA:PTAA. In the survey, only the expected signals were found. A carbon-oxygen signal from the PEG group as well as a contribution from the underlying ITO substrate could be identified in the fine analysis.
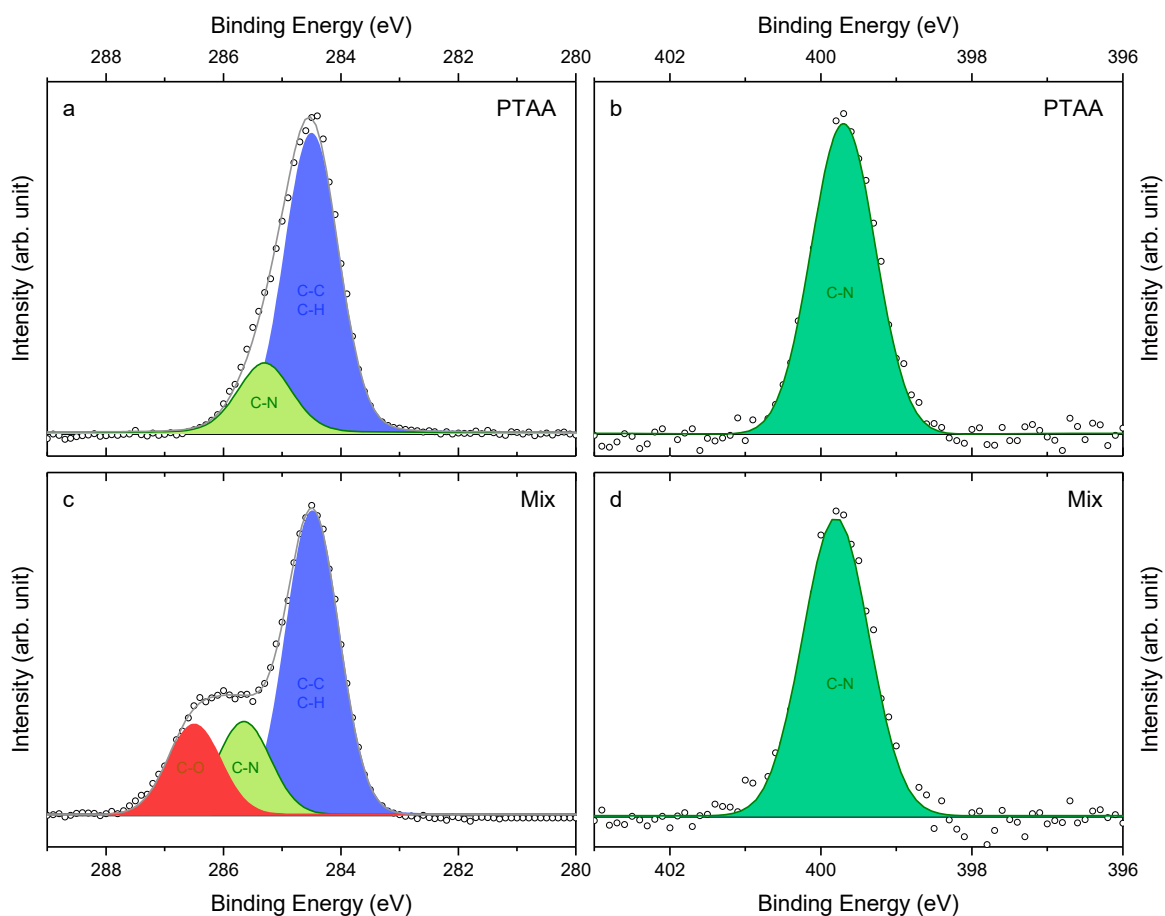
Figure 5.7. XPS elemental analysis of pure PTAA (a,b) and a 95:5 mixture of PEG-TPA:PTAA (c,d). Shown are the fine scans of the carbon peak (a,c) and nitrogen peak (b,d). The mixture includes an oxygen signal in the carbon peak which can be associated with the PEG group. Colored regions depict the area determined by a Voigt fit.

After the chemical analysis, optical characterization via UV-Vis spectroscopy was performed. As can be seen in Figure 5.8, mixtures of the molecules with PTAA show the expected blend of peaks from PTAA and the pure molecules. For PEG-TNA the absorption peaks exhibit a shift towards shorter wavelengths. From the absorption onset of these measurements, the bandgap was estimated. A bandgap of 2.9 eV was found for pure PTAA and the PTAA mixtures, while pure PEG-TNA showed a larger bandgap of 3.1 eV. In combination with the ionization potential, analyzed via PYS measurements on thin films, the energy levels of the used molecules and mixtures could be assessed (Figure 5.8b). Both mixtures of PEG-TPA and PEG-TNA with PTAA and the pure PTAA show lower HOMO levels, which is expected to facilitate charge carrier extraction in solar cells.
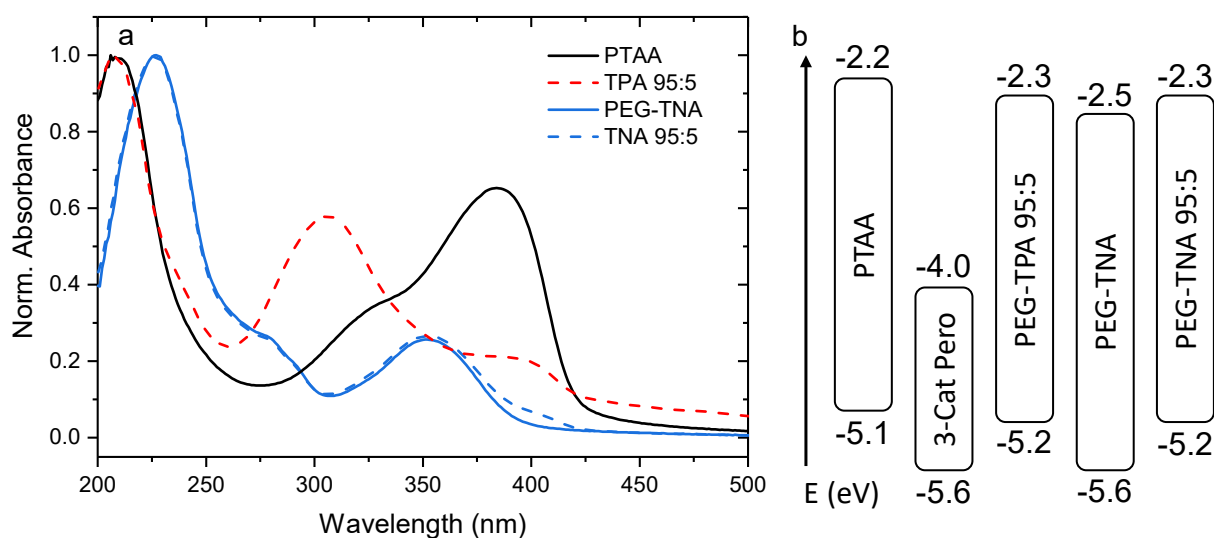

Figure 5.8. Optical/electrical characterization. (a) Normalized UV-Vis spectra of thin films of PTAA, PEG-TNA, and the 95:5 mixtures. (b) Energy levels of the same materials. The optical bandgaps were estimated from the absorption onsets. Ionization potential was measured via PYS. Perovskite levels are taken from literature.[209]

As mentioned in the introduction, suitable energy levels are not the only goal for the two novel molecules. Improved wetting should also be achieved for the subsequent perovskite layer. In order to analyze the performance of the substances with regard to this property, a morphology analysis was carried out. In the first step, SFM images were recorded, which are presented in Figure 5.9. All molecules and mixtures revealed closed, pinhole-free surfaces. Concerning the roughness, all samples were evaluated over a length of 50 µm. PTAA showed the lowest roughness with a R_a value of 0.6 nm. As can be also seen in the SFM image for pure PEG-TNA, some higher surface features are present which consequentially also increase the surface roughness to 0.7 nm. Mixing with PTAA results in a decrease in roughness to $R_a = 0.4$ nm. All in all, all layers show a smooth, closed surface.

In the next step, contact angle measurements were performed to evaluate the wetting properties of the samples. As shown in Figure 5.10. for the case of water, contact angles could be significantly decreased when using the mixtures or pure PEG-TNA compared to PTAA. The contact angle decreased from 82° for neat PTAA to 48° for the TPA blend and 35° for the TNA blend, a decrease of up to 58%. Contact angles recorded with diiodomethane displayed the same trend. The surface free energy was then calculated according to the OWRK model. An increase

from 47 mN m^{-1} for pristine PTAA to 66 mN m^{-1} for TPA 95:5, 70 mN m^{-1} for TNA 95:5, and 71 mN m^{-1} for pure PEG-TNA could be measured. This was attributed to the higher polarity of the PEG-TPA and TNA molecules compared to PTAA (for the pure polar parts of the surface free energy, see Table 5.2). Wetting envelopes also display the much higher wettability of fluids with a vast range of surface tensions on PEG-TNA and the mixtures compared to pure PTAA.
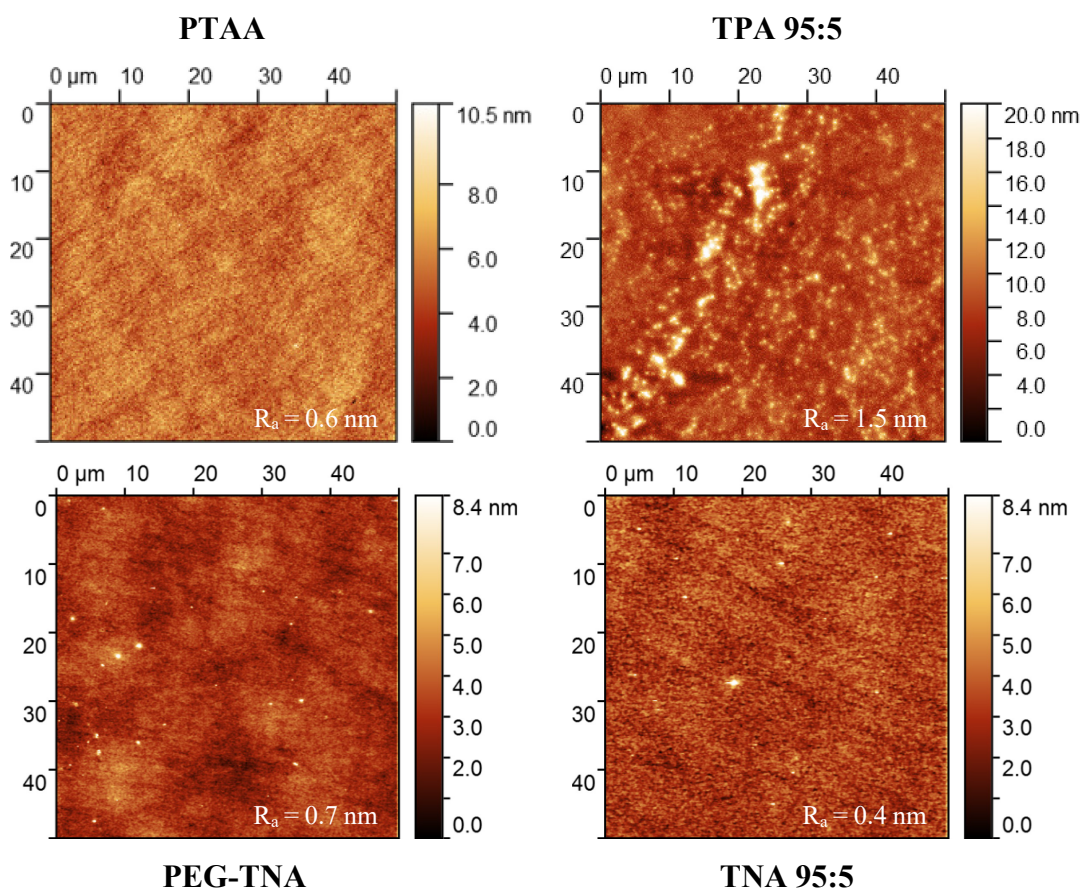
Figure 5.9. SFM images of PTAA, PEG-TNA, and the 95:5 mixtures. All films show a smooth, closed, pinhole-free surface. The 95:5 mixture of PEG-TNA shows some higher features in the layer. Roughness values are measured over a length of 50 μm.

In order to replace PTAA in solar cells, novel materials must have a good ability to transport holes. Therefore, the hole mobility of PEG-TNA (pure and 95:5 mix with PTAA) and a 95:5 mixture PEG-TPA:PTAA was determined through space charge limited current measurements of hole-only devices. These devices sandwich the layer to be analyzed between two materials with very low electron conductivity. This enables mostly holes to be responsible for the flowing current. Thus, by analyzing the current-voltage curve, the hole mobility can be assessed. Hole-only devices were fabricated, and the JV curves displayed in Figure 5.11a were recorded. It is immediately noticeable that PTAA devices exhibit the highest current flow. Fitting the curves and extracting the hole mobility according to the Mott-Gurney square rule (see Figure 5.11b) resulted in a hole mobility of $2.3 \cdot 10^{-7}$ cm^2 V^{-1} s^{-1} for PTAA, $4.8 \cdot 10^{-8}$ cm^2 V^{-1} s^{-1} for TPA:PTAA, $6.8 \cdot 10^{-8}$ cm^2 V^{-1} s^{-1} for TNA:PTAA and $3.9 \cdot 10^{-8}$ cm^2 V^{-1} s^{-1} for pure PEG-TNA. While there

are no reference values for the new molecules, it must be noted that the value for PTAA is two orders of magnitude lower than reported in the literature. Ko et al. have reported that the hole mobility of PTAA is 3-4·10⁻⁵ cm² V⁻¹ s⁻¹ depending on the PTAA thickness,[210] and even higher reported values can be found.[211]

Since PTAA is known to degrade in oxygen and water-containing atmospheres,[212] it is believed that this contributed to the low conductivity measured here. Still, the conductivity of PTAA is at least one order of magnitude higher than those of the other molecules and mixtures. Before proceeding to integrate the PEG-TNA into a perovskite solar call, Table 5.2 again gives an overview of the determined morphological, optical, and electronic properties.
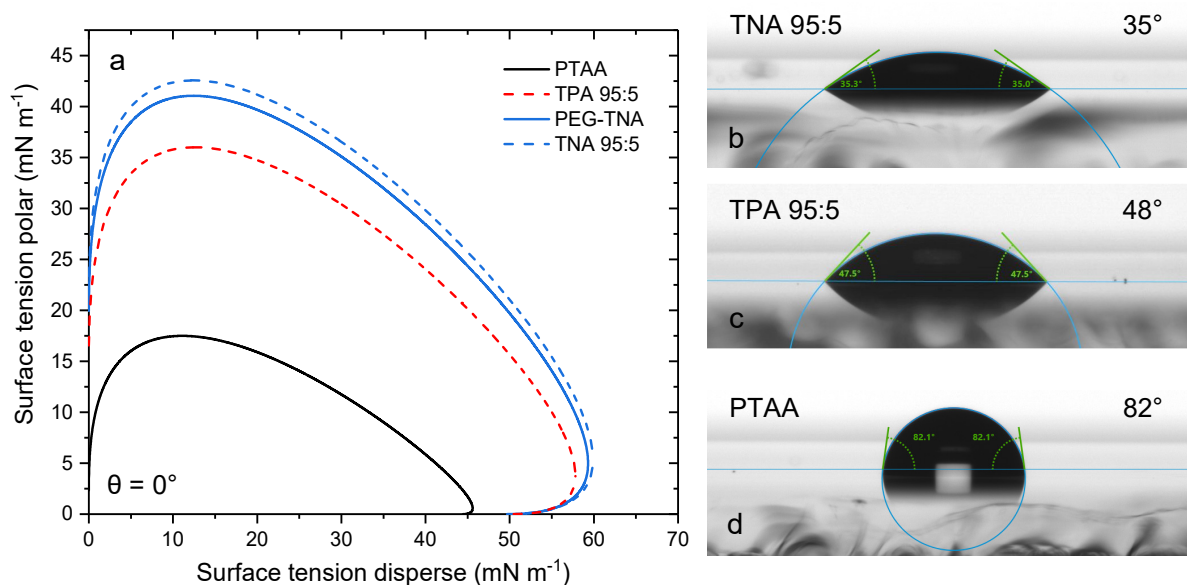
Figure 5.10. Wetting behavior. (a) Wetting envelope of different mixtures. (b-d) contact angles of water on PTAA, PEG-TNA, and the 95:5 mix. Pure PEG-TNA and the mixtures exhibit significantly improved wetting when compared to PTAA. The contact angle of water was reduced by more than 50%.
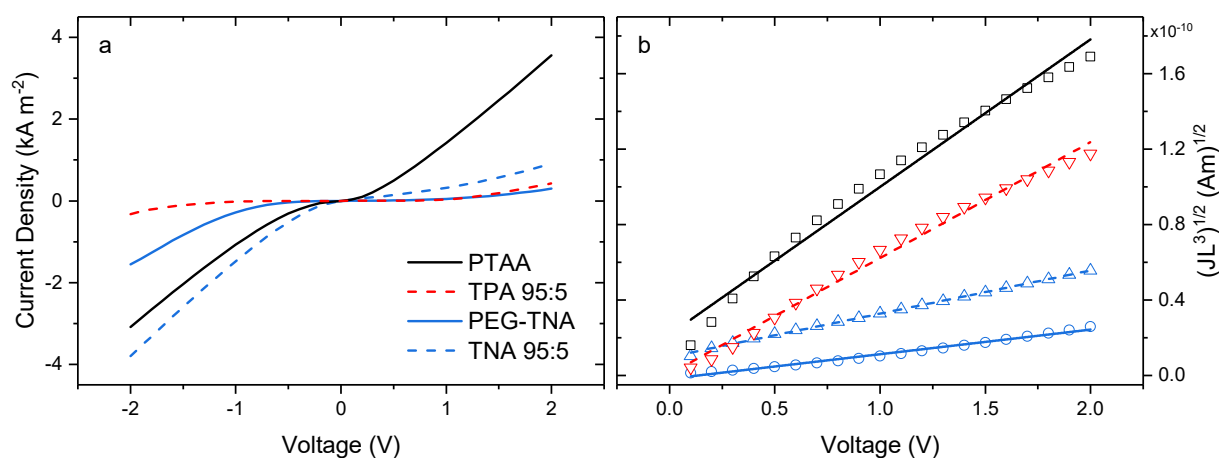
Figure 5.11. Mobility analysis via hole-only devices. (a) JV curves of PEG-TNA, PTAA, and a 95:5 mixture. (b) fits to determine the hole mobility via the Mott-Gurney square rule. PTAA shows the highest conductivity and hole mobility of the analyzed molecules.

93

Table 5.2. Overview of the properties of PTAA, PEG-TNA, and the 95:5 mixtures. Shown are the transmission, roughness, surface free energy, energy levels, and hole mobility.

	Transmission [a] (%)	Roughness (nm)	Surface Free Energy polar (mN m^{-1})	disperse (mN m^{-1})	Energy Levels HOMO (eV)	LUMO (eV)	Hole Mobility (cm^2 V^{-1} s^{-1})
PTAA	95	0.6	2.3	44.4	-5.1	-2.2	$2.3 \cdot 10^{-7}$
TPA mix	92	1.5	15.2	50.5	-5.2	-2.3	$4.8 \cdot 10^{-8}$
TNA mix	98	0.7	20.0	49.8	-5.2	-2.3	$6.8 \cdot 10^{-8}$
PEG-TNA	99	0.4	21.4	49.7	-5.6	-2.5	$3.9 \cdot 10^{-8}$

[a] Averaged over the visible spectrum

5.2.4 Application in Perovskite Solar Cells

The efficacy of perovskite solar cells is highly dependent on the perovskite film morphology. Closed, pinhole-free layers with larger grain structures highly benefit the device's performance. To investigate if a perovskite layer of sufficient quality can be produced on the novel molecules, triple cation perovskite was processed by different means onto layers of PTAA, PEG-TNA, and the 95:5 mixture. Figure 5.12 presents an overview of samples with spin-coated and inkjet-printed perovskite. As can be clearly seen spin coating is possible on all three investigated samples. However, the film quality is vastly improved when PEG-TNA or the 95:5 mixture is used to pre-treat the substrate. Fewer pinholes and a more homogeneous film coverage can be achieved.
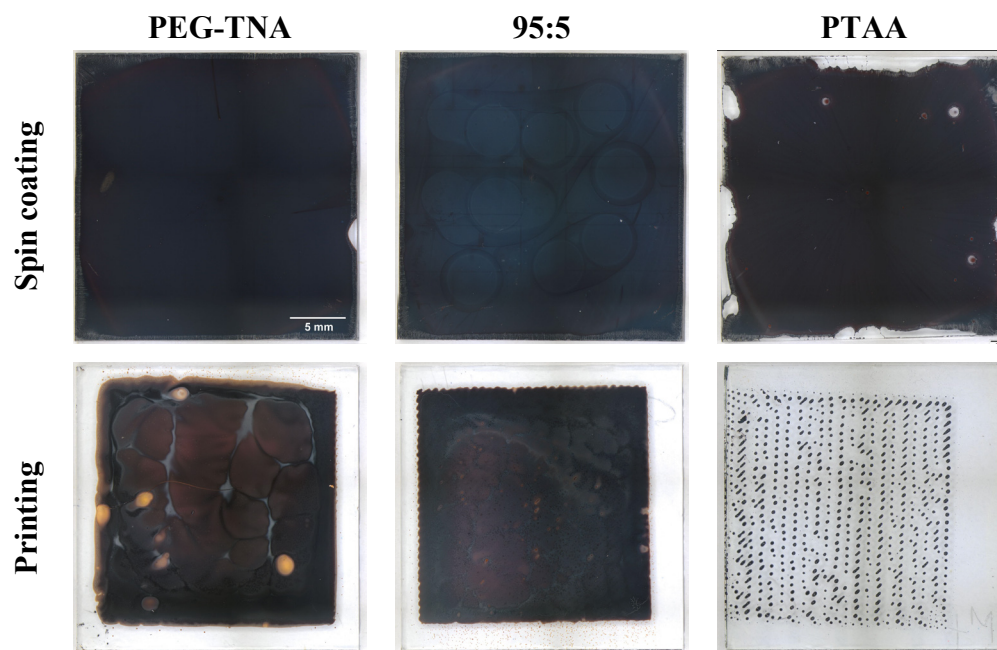

Figure 5.12. Spin-coated (top) and printed samples (bottom) of perovskite on the three different films. While spin coating on PTAA is possible, adding the PEG-TNA molecule enhances surface quality. In the cases of printing, PEG-TNA allows for closed films.

Printing the perovskite further demonstrates the superior wetting properties of PEG-TNA compared to PTAA. While it is possible to obtain a closed perovskite surface on PEG-TNA and the mixture, the printed drops do not merge into a homogenous layer on PTAA. As stated in the introduction, the nonpolar and therefore hydrophobic PTAA does not allow sufficient wetting by the polar solvents used for perovskite preparation. In contrast, completely covered films can be obtained on PEG-TNA. Mixing the two substances makes it possible to adjust the wettability and thus not only obtain complete wetting but also defined structures. This can be seen in Figure 5.12 for the printed samples (bottom row). For all three, a square pattern was printed. In the case of PTAA the printed surface is not closed (wetting too low) and for pure PEG-TNA the edges of the square are washed out (wetting too high). The 95:5 mixture gives a good compromise and results in a well-defined, closed shape.

Further investigations of the perovskite layers, spin-coated on different molecules or mixtures, were performed by recording the SEM images displayed in Figure 5.13. Microscopically, all layers exhibit a closed-grain structure with no visible pinholes. However, the grain size of the novel molecules and their mixtures with PTAA is notably smaller than those of PTAA. In principle, larger grains, such as those in Figure 5.13a, are expected to show better performance when integrated into PSCs. The long, needle-like structures in Figure 5.13a, c, and d are most likely lead iodide. The black dots in Figure 5.13d are presumably caused by prolonged electron beam exposure while recording the SEM image.
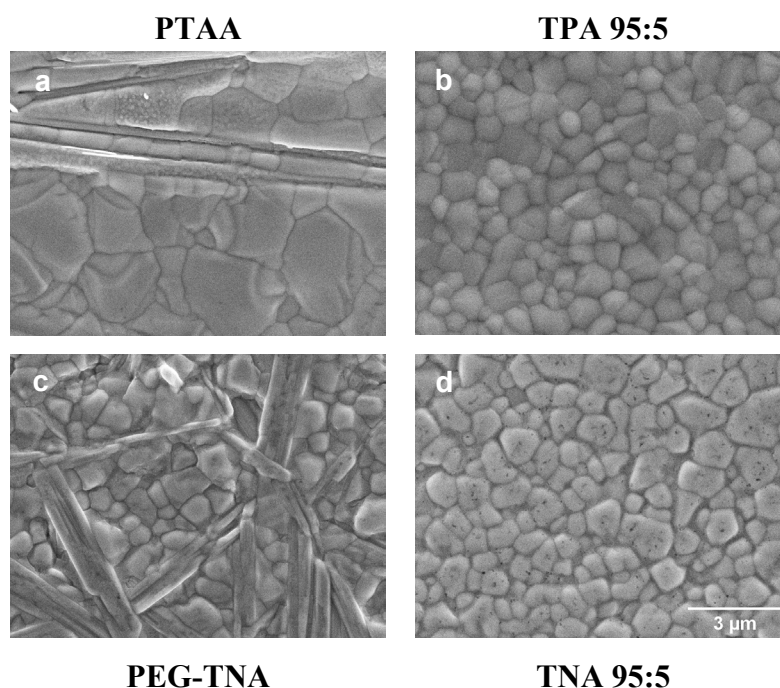
Figure 5.13. SEM analysis of PEG-TNA, PTAA, and the 95:5 mixture. (a) On pure PTAA the perovskite crystallizes in larger crystals. (b) A 95:5 mixture with TPA shows small crystallites. (c) The needle-like structures in pure PTAA and PEG-TNA are most likely lead iodide. (d) Black dots are not pinholes but defects due to the high SEM energy. Measurements courtesy of Carola Klimm, HZB SEM service.

In a final step, to assess the performance of the novel molecules in working devices, perovskite solar cells, including the novel materials or PTAA were fabricated. JV characteristics were recorded and the open-circuit voltage V_{oc}, the short-circuit current J_{sc}, the area-normalized

series and parallel resistances R_s, and R_p, the fill factor *FF* and the power conversion efficiency *PCE* were calculated. The results are shown in Table 5.3. It can be seen that the series resistance of all new material combinations is higher than that of PTAA. This was to be expected given the previously measured lower mobilities of these materials. As a higher series resistance reduces the fill factor, the overall power conversion efficiency of the solar cell is likewise reduced. Regarding the shunt resistance, lower values are observed for the novel materials, especially for PEG-TNA. Since these are mostly caused by manufacturing defects such as internal shorts that create an alternative path for the generated photocurrent, structural properties of the perovskite on the novel molecules are most likely the cause of the lowered values.

As seen before, the microscopical structure of perovskite on PTAA reveals larger grains. Huang et al. have found that grain boundaries are often rich in defects and thus favor undesired recombination of charge carriers.[200] Smaller grains (and thus more grain boundaries), as can be seen in Figure 5.12 for the new materials, can therefore limit the fill factor and hence also the efficiency of the cell. The novel materials could therefore not improve the efficiency of the employed PSC types.

Table 5.3. Overview of the solar cell parameters. Shown are the open-circuit voltage V_{oc}, the short-circuit current J_{sc}, the area-normalized series and shunt resistances R_{ser}, and R_{sh}, the fill factor *FF* and the power conversion efficiency *PCE*. All values are averaged over at least 10 devices.

	V_{oc} (V)	J_{sc} (mA cm^{-2})	R_{ser} (mΩ cm^2)	R_{sh} (Ω cm^2)	*FF* (%)	*PCE* (%)
PTAA	1.08	21.76	5.45	5.58	74.68	17.59
TPA mix	1.09	21.74	9.88	4.73	68.43	16.16
TNA mix	0.93	21.79	6.45	1.31	66.15	13.58
PEG-TNA	0.89	21.68	7.17	1.22	64.55	12.64

5.2.5 Conclusion for Novel Molecules

In this section, two novel materials were analyzed as possible replacements for PTAA in perovskite solar cells. Better wetting for perovskites as well as better device performance due to more favorable energy levels was expected. Closed films could not be obtained for pure PEG-TPA. PEG-TNA together with 95:5 mixtures of both molecules with PTAA showed closed films with appropriate film morphologies. The hole conductivity was found to be significantly lower than that of PTAA. While films of the blends and PEG-TNA greatly improved wetting for spin-coated perovskites and enabled inkjet printing, no improvement in device performance could be achieved.

From these experiments, it can be concluded that PEG-TNA, as well as PEG-TPA, should be analyzed for their potential as possible wetting promoters, used as additives with polymers such as PTAA. Our collaborators in Heidelberg further plan to polymerize both molecules as well as additionally alter their structure to achieve the goal of improved device performance in PSCs.

6 Crosslinking for Multilayer Devices

In the previous chapter, it has been shown that multilayer OLEDs exhibit significantly improved characteristics when compared to single-layer ones. However, processing these additional layers is not always an easy task when utilizing solution processing methods. One approach is to utilize crosslinking to insolubilize underlaying layers prior to further processing. This chapter deals with crosslinking as an alternative approach to finding an orthogonal solvent system. The concept of crosslinking is introduced first before a novel material is used as an additive crosslinker to facilitate the production of inverted Super Yellow OLEDs with additional interlayers.

Parts of this chapter have been previously published.[213] Additional data has been included.

6.1 Introduction

As described in section 2.4.1, OLEDs can consist of an emissive layer sandwiched between two conductive electrodes. However, in this most basic OLED structure only very low current efficacies can be reached since charge carriers can pass through the active material without recombination; carriers might face an injection barrier when traversing into the emitting layer or are not confined in the middle of the emitter layer with the possibility of emission-quenching at the electrodes. In more complex architectures, these issues can be counteracted by inserting additional injection, blocking, and transport layers around the emitter. These multi-structures can be fabricated by a variety of processes. The industry standard of thermal evaporation, while in principle being able to fabricate multilayers, quickly reaches its limit, since not all material classes are suitable here. Polymer materials, a class of materials of great research interest, tend to degrade when exposed to elevated temperatures. Only a few polymers have been successfully processed by thermal evaporation.[214,215] According to a review by Gritsenko and Krasovsky,[216] in the majority of cases, polymer layer fabrication by physical vapor deposition happens via thermal decomposition and subsequential repolymerization of the polymer on the substrate. Solution processing as an alternative method brings its own problems. Base materials have to be dissolved in suitable solvents and are then deposited by a variety of different techniques such as spin coating, spray coating, blade coating (doctor blading, slot-die coating), roll-to-roll processing, or inkjet printing. While finding an appropriate solvent can be challenging on its own, special care must be taken to ensure that the solvent chosen does not redissolve the previously deposited layer. This leads to what is known as an orthogonal solvent system, where each layer is not soluble in the subsequent solvent (an exemplary stack is shown in Figure 6.1). Since many molecules and polymers have similar solubilities in "standard" solvents like toluene or tetrahydrofuran, this can be a difficult task.

As will be seen later in this chapter, reducing the contact time between a layer and the subsequent solvent can be a viable way to solve this problem. This is, however, not a suitable approach for all the above-mentioned fabrication methods, since especially for blade coating the resulting layer thickness strongly depends on the coating speed. Therefore, the contact time cannot easily be adjusted here. Another method to reduce solubility is thermal stabilization. Here a polymer is subjected to prolonged heat treatment, resulting in strongly reduced solubility. This has been widely used with the common hole-transport material poly(9,9-dioctylfluorene-*alt-N*-(4-sec-butylphenyl)-diphenylamine) (TFB),[217] and should, according to literature, also be applicable for other polymer materials.[218] Since heat treatment is known to reduce the quantum yield of polymer emitters,[219] this is not a suitable approach for all OLED layers. The first technique is based on endowing the polymer side chains with reactive functional groups. Crosslinking can be a suitable alternative. Here polymer chains are linked together by additives, forming a less soluble network. Some important crosslinking specimens should be briefly discussed with their positives and drawbacks:

Silanes can be converted into silanols via hydrolysis, which then can link small molecules by condensation furnishing siloxanes.[220,221] No specific activation such as temperature or light is needed. However, the crosslinking method is not suitable for water-sensitive materials or devices as water is a side product of the condensation reaction. In any case, this water might also need additional removal steps.

Styrenes have been used to link small molecules as well as polymers via a thermally initiated radical reaction.[222] No side products are formed, however, the materials that are being linked need to be thermally stable over a longer period and the selectivity of radical reactions remains an issue.

Acrylates, like styrenes, are immobilized by a radical mechanism, but an additional initiator is needed, which itself can be activated thermally or via light.[223,224] As with silanes, side products (here from the initiator) can be an issue.

Oxetanes usually use acids as an initiator to start the rapid polymerization reaction. Photoacids are commonly used, which can lead to side products or mobile ions which might have to be removed.[225,226]

All of these specimens are usually added as functional side groups. However, this makes them highly selective. More universal crosslinkers can be added to a solution and are able to crosslink multiple classes of polymers. Particular care is required specifically when crosslinking the active layer of an OLED. While the polymer should be rendered insoluble, the process must not disturb the material's π-electron system, which could result in reduced light emission or conductivity.
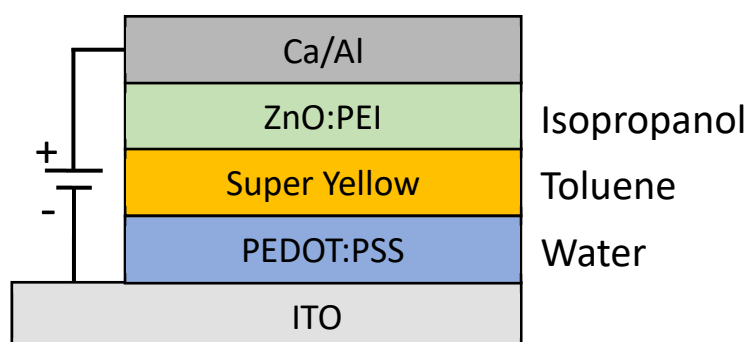
Figure 6.1. Exemplary OLED stack utilizing an orthogonal solvent system where a solvent is not able to dissolve the previously deposited layers. On the right side, the solvents are listed for each layer.

In this chapter, the polyphenylene-vinylene polymer (PPV) Super Yellow (SY) is crosslinked via the addition of a novel bisazide additive. Different crosslinking conditions are investigated and optimized. A multi-layer OLED containing an electron blocking layer (EBL) is then produced to assess the crosslinking effectivity. Different EBL materials and deposition methods are examined resulting in a highly efficient, solution-processed OLED.

6.2 Materials and Experimental Setup

Crosslinker Synthesis: The bisazide crosslinker was synthesized according to Scheme 6.1 by the group of Jan Freudenberg at Universität of Heidelberg. Details of the synthesis process can be found elsewhere.[227]
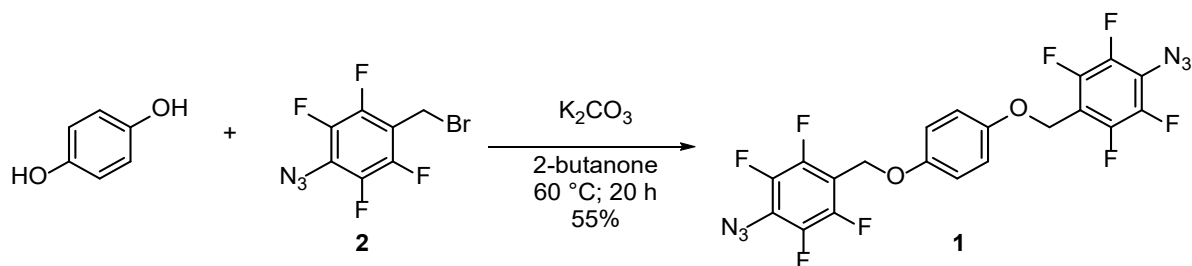
Scheme 6.1. Reaction scheme of the synthesis of the azide crosslinker 1 from hydrochinone and 1-azido-4-(bromomethyl)-2,3,5,6-tetrafluorobenzene.

Solution Preparation: The PDY-132 (Super Yellow, Sigma-Aldrich) light-emitting polymer and the crosslinker were dissolved in toluene at concentrations of 5 mg ml^{-1} and combined via mixing in the desired ratios. Prepared solutions were stirred for several hours at 50 °C before being used. Zinc oxide (ZnO) nanoparticle solution (Genesink, 1% dispersion in isopropanol, particle size 12 nm) was used as received. A solution of polyethyleneimine (PEI) was prepared according to literature by dissolving PEI (Sigma Aldrich, $M_W = 25\,000$ g mol^{-1}) in isopropanol to obtain a concentration of 0.4 wt%.[166] Poly[bis(4-phenyl)(2,4,6-trimethylphenyl)amine (PTAA) (Ossila, $M_W = 55\,000$ g mol^{-1}) was dissolved in toluene at a concentration of 5 mg ml^{-1} for 8 nm films and 1 mg ml^{-1} for 4 nm films.

Sample Preparation: Glass substrates with patterned ITO (Psiotec Ltd.) for device preparation, quartz glass for spectral analysis, and soda-lime glass for thickness measurements were cleaned by thoroughly wiping them with acetone and isopropanol. Afterwards, a 5 min O$_2$ plasma treatment in a Femto plasma system (Diener) at a gas pressure of 0.35 mbar and 500 W of power was used to activate the sample surface before solution deposition.

Crosslinking Procedure: Super Yellow thin films were produced from a toluene solution, with or without a crosslinker, spin-coated at 2500 rpm for 60 s. Samples were subsequently transferred to a vacuum oven which was flushed multiple times with nitrogen before evacuation. Crosslinking (CL) was performed under vacuum at different temperatures and durations. After crosslinking, the oven was allowed to cool down slowly to room temperature before it was vented with nitrogen gas.

Thin Film Characterization: The film thickness was determined via a DektakX Stylus Profiler (Bruker) as well as a LEXT OLS4100 confocal laser microscope (Olympus). A washing test was performed prior to thickness measurements of crosslinked samples: For this purpose, 40 µl of pure toluene was spin-coated on the sample. Samples were then dried for at least 15 min on a hotplate at 120 °C before any thickness measurements. The sample surface was analyzed using a scanning force microscope (Bruker FastScan) in tapping mode. UV-Vis spectra were taken with a Perkin Elmer Lambda 950 double-beam spectrometer. An FS5 and an FLS980 fluorescence spectrometer (Edinburgh Instruments Ltd.) were used for photoluminance measurements and quantum yield measurements respectively.

Device Preparation: Pre-patterned ITO substrates were prepared as described above. A blend of ZnO and PEI was then spin-coated at 2500 rpm and subsequently dried on a hotplate for 10 min at 120 °C. The SY/Crosslinker emitter was doctor-bladed with a speed of 10 mm s^{-1} on a 60 °C substrate plate, where it was also dried for 10 min. The fabrication parameters of the EBLs are described in the main text.

All solution processing was carried out in ambient conditions. Finally, a top electrode of 10 nm of MoO_3 and 200 nm of silver was evaporated thermally with a base pressure of 10^{-6} mbar. Shadow masks were used to make devices with 0.04 and 0.49 cm^2 of active area. Encapsulation was done using glass slides and UV-curable resin (Ossila), cured at 365 nm for 10 min.

Device Characterization: Devices were characterized by measuring current density-voltage-luminance curves with a Keithley 2612B source meter and a Konica Minolta LS-160 luminance meter with a purpose-built setup (detailed description in section 3.2.10). Electroluminescence spectra were recorded on a CS 2000 spectrometer (Ocean Optics) using OceanView software.

6.3   Optimization of the Crosslinking Process

Since the bisazide crosslinker (shown in Scheme 6.1) has not been described in literature before, it is not known what crosslinking parameters are best suited to obtain sufficiently insolubilized films. It is to be expected that longer durations, as well as higher proportions of crosslinkers in the polymer material, will lead to more resistant films. This section is a summary of the work of Paul Hänsch, published in his Master Thesis: "Azide-based cross-linker for multilayer solution processed organic light-emitting diodes".[228] As he has performed the crucial optimization experiments on which the further experiments of this chapter are based, his results on crosslinking of Super Yellow shall be briefly summarized here.

Temperature and crosslinker percentage series were carried out to determine at which temperature the crosslinking process is the most efficient and what crosslinking times are needed. The results are shown in Table 6.1. To determine the percentage of the remaining film, a washing test was performed as described above. The expectations of higher film retention at longer durations could be confirmed. Up to 98% of the initial thickness remained when crosslinking for 8 h but even durations as low as 1 h lead to 87% of remaining film. Higher crosslinker concentration was shown to have a positive influence on the film, a weight percentage of 5% of crosslinker led to thicker remaining films than 1%.

Table 6.1. Crosslinking parameters for Super Yellow. Shown are the crosslinking duration at a temperature of 140 °C, the crosslinker concentration, and the remaining film thickness after a washing test with toluene. Long curing times ($\geq$ 4 h) led to a high proportion of residual film. A low concentration of 1 wt% at 1 h of crosslinking gives adequately insolubilized films.

Duration	8 h		4 h	1 h
CL concentration (wt%)	5	1	5	1
Remaining thickness (%)	98	94	93	87

Higher temperatures up to 180 °C, longer durations up to 20 h, and concentrations up to 50 wt% were also investigated. However, since Super Yellow is known to degrade under prolonged exposure to higher temperatures it was concluded that a good compromise between film retention and crosslinking parameters was 1 h of crosslinking at 140 °C, with 1 wt% of crosslinker. Additionally, this enables the future application of the crosslinker on temperature-sensitive substrates such as PET or other flexible materials. It is worth mentioning that the

crosslinker was initially intended for crosslinking polyfluorenes. However, it was quickly determined that crosslinking could only be achieved in a few selected materials. Contrary to the expectation that PPV materials are not compatible with this crosslinker, Super Yellow could be successfully crosslinked.

6.4   Characterization of Crosslinked Films

Preliminary work suggested that crosslinking sufficiently happens at 140 °C. At this temperature, singlet nitrene generation is expected to happen at both azide groups of the crosslinker. To support this claim, thermogravimetric analysis (TGA) measurements were performed. The curves are shown in Figure 6.2a. A mass loss of 11.7% could be observed starting at 140 °C and ending at 204 °C. This is in good agreement with theoretical calculations which suggest a loss of 10.9% due to the cleavage of nitrogen from the molecule. The disappearance of the signature azide peak at 2125.17 cm^{-1} in the FTIR spectrum (Figure 6.2b) after annealing further supports this evidence.

To determine whether the crosslinker interferes with the optical properties of the Super Yellow emitter material, absorption and emission spectra were carried out on crosslinked and non-crosslinked thin films. UV-absorption spectral shape and maximum remain constant under the addition of different crosslinker percentages (see Figure 6.3a) with a maximum at 447 nm. The same holds true for the photoluminescence at low crosslinker percentages. Increasing the amount of crosslinker leads to a broadening of the PL spectrum as the intensity of the emission peak at 550 nm decreases. PL signal and quantum yield (Figure 6.3b) are likewise reduced when increasing the crosslinker concentration. For all further experiments, 1 wt% of crosslinker is added if not stated differently. Since no blue-shift was observed for either absorption or emission, it can be concluded that the crosslinking mechanism involves CH insertion of nitrenes into the side chains of the emitter, as described in literature,[229] while the PPV backbone/chromophore remains intact.
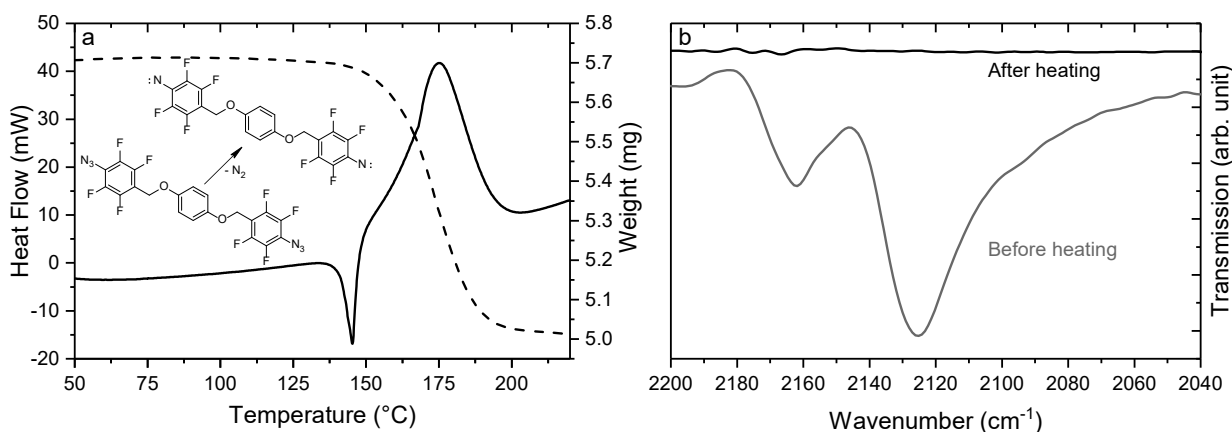
Figure 6.2. Crosslinker analysis. (a) TGA/DSC curves. The curve shows a weight loss starting at 140 °C and ending at 204 °C with a total mass loss of 11.7%. Theoretical calculations give a total weight loss of 10.9%. (b) FTIR spectrum. The typical azide peak is present at 2125.17 cm^{-1} before heating. After heating, a strong reduction of the azide peak is visible, indicating nitrogen cleavage from the bisazide. TGA/DSC and IR measurements were performed at University of Heidelberg by Daniel Ehjeij.
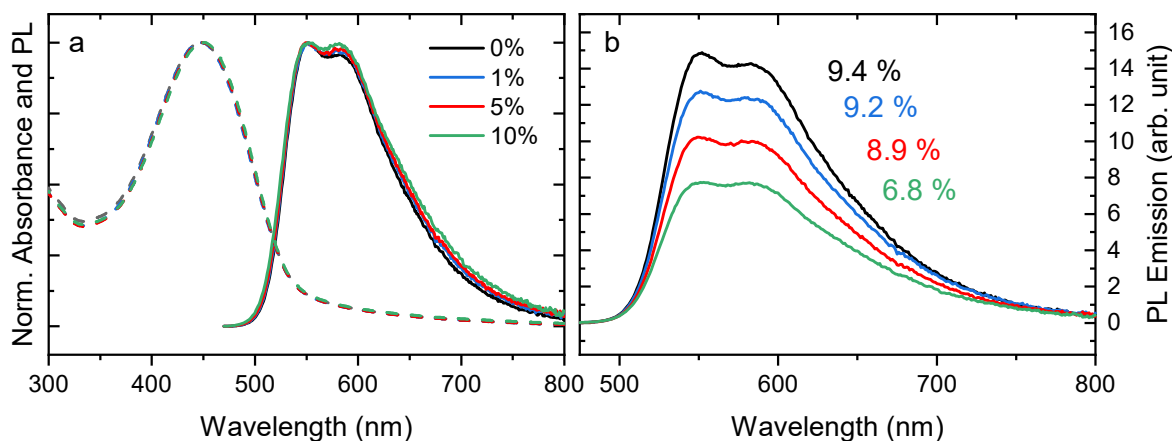
Figure 6.3. Spectral characterization of films with different crosslinker concentrations. (a) Normalized absorbance and PL emission. At low crosslinker concentrations, no shift in absorbance or the PL signal peak could be observed. High concentrations shift the PL and lead to a broadening of the spectrum. (b) PL emission and quantum yield. The quantum yield only decreases significantly at high crosslinker concentrations.

6.5   Influence of the Electron-Blocking Layer

To further judge the effectiveness of the crosslinking procedure, inverted bottom-emitting OLEDs were produced. An additional electron blocking layer is solution-processed from toluene onto the Super Yellow emitter. As described before, an electron blocking layer prevents charge carriers (in this case electrons) to pass through the emitter layer without recombination. In this case, the energy level of the blocking layer must be matched to that of the emitter to achieve effective blocking of the electrons. The EBL LUMO has to lie higher than the LUMO of the EML. However, its HOMO should be close to the EML HOMO to facilitate hole injection into the emitter. A schematic stack of the inverted OLED can be seen in Figure 6.4a.
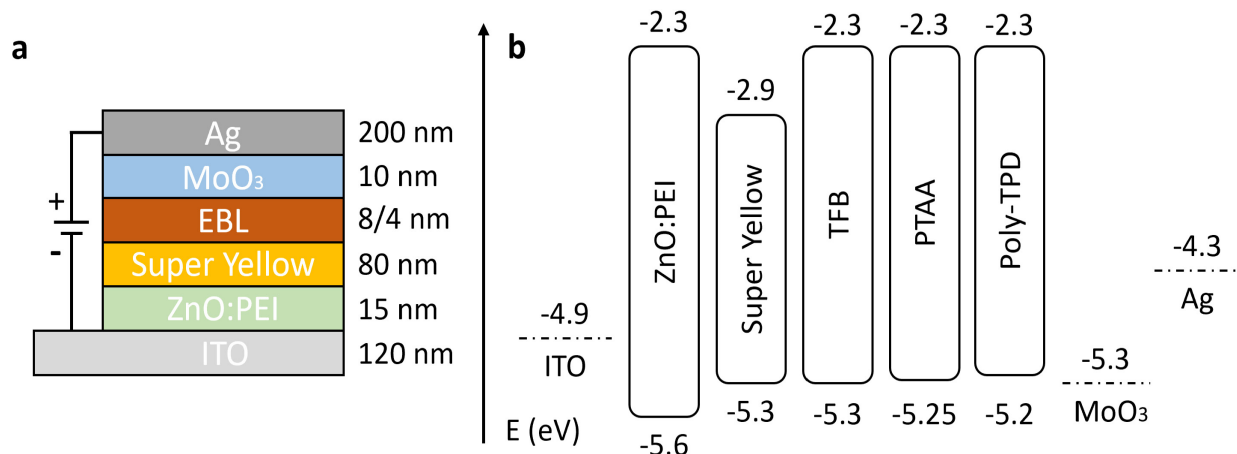
Figure 6.4. Overview of the OLED architecture. (a) Schematic representation of the inverted OLED stack with layer thicknesses. (b) Energy levels of the used materials.[230,231] Dotted lines indicate work function levels. No interfacial effects were taken into account and all levels were regarded as being vacuum aligned.

In Figure 6.4b the energy levels of all employed materials are displayed. TFB, PTAA, and Poly(N,N'-bis-4-butylphenyl-N,N'-bisphenyl)benzidine (Poly-TPD) were investigated as

possible candidates for the EBL. All three materials have been previously applied as an electron blocking layer either in OLEDs or solar cells.[232–234]

If no crosslinker is added to the Super Yellow, the partial dissolution of the emitter from the additional solution processing can be expected to reduce the effectiveness of the device. As a first step, OLEDs with an active area of 0.04 cm^{-2} were fabricated. The EML was hereby crosslinked in half of the devices and the different EBL materials were included in part of the crosslinked and non-crosslinked OLEDs. In Figure 6.5 a comparison between a reference (reference always denotes a device without EBL) and two devices with TFB and PTAA is shown in terms of current efficacy. It can be seen that the addition of crosslinker to a reference device reduces the current efficacy by 19% from 3.2 to 2.7 cd A^{-1}, following the previous results for PL and Photoluminescence Quantum Yield (PLQY). When adding the EBL to non-CL devices efficiency decreases as well (6% for TFB and 10% for PTAA). On CL-SY the EBL can help to recover previously lost efficacy. However, only a slight increase compared to the reference is visible, reaching 95% of the reference value for PTAA and 109% for TFB. Experiments with Poly-TPD did not yield favorable results and were not continued after a first survey.
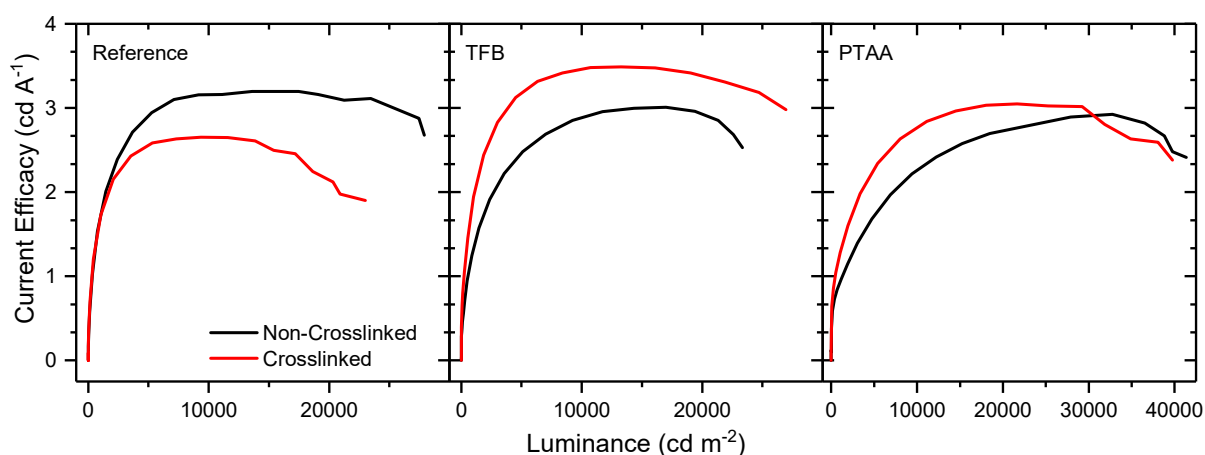
Figure 6.5. Comparison of different EBL materials. The addition of crosslinker lowers the efficacy of reference devices. TFB on CL-SY surpasses the reference slightly while PTAA does not.

Not only the efficacy of an OLED is affected by introducing an additional layer. Given that electrons should effectively be prevented from passing through to the anode by the blocking layer, the leakage current is expected to decrease as well. The leakage current is the current that flows against the blocking direction of a diode, in this case current that flows at negative voltages. Since EBL materials oftentimes exhibit a good conductivity for holes, they normally have a secondary function, as a hole transport layer, in devices. Transport, however, is dependent on the layer thickness,[235] which was studied next. OLEDs with different PTAA thicknesses were produced and measured. As can be seen in Figure 6.6a, the leakage current is significantly reduced by more than two orders of magnitude when a thin EBL is added.

Counterintuitively, a thicker PTAA layer does not result in a lower leakage current. The efficacy of crosslinked devices with a thinner, 4 nm layer of PTAA can reach 4.9 cd A^{-1} (see Figure 6.6b), an increase from the reference of 53%.

Figure 6.6. Influence of layer thickness on device efficiency. (a) Current densities show that devices with an EBL exhibit lower leakage current. (b) Efficacies. For PTAA, a thinner EBL with a thickness of 4 nm was found to increase the device efficiency by more than one with 8 nm.

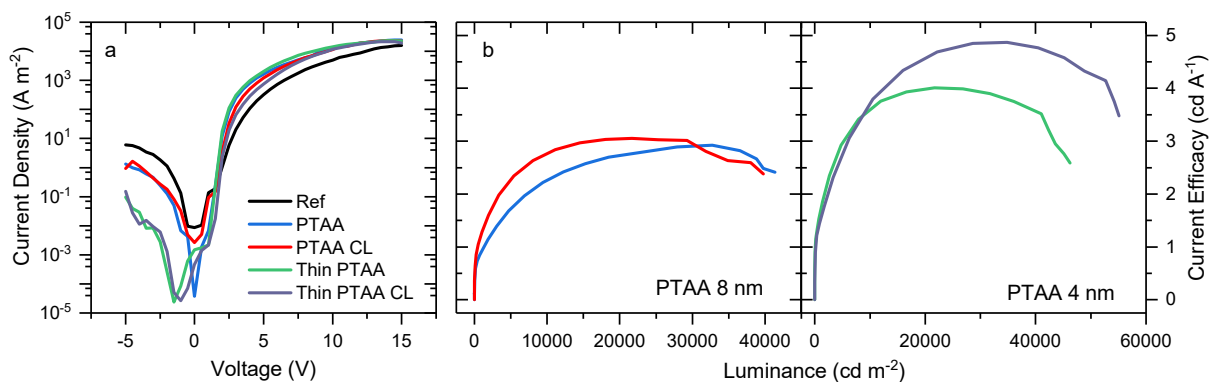Since the pure crosslinking process slightly affected the efficacy of the device, it also needs to be investigated whether the electroluminescent emission properties change when crosslinking Super-Yellow or adding an EBL. From the PL data, it was expected that no change in emission would be visible for crosslinked OLEDs. This could be confirmed by taking the EL spectra presented in Figure 6.7a. The EL shape stays constant with a maximum emission at 554 nm. When adding an EBL however, the EL spectrum exhibited a bathochromic shift, especially in the case of TFB where the maximum shifts to 586 nm. This effect is well known in literature, where the formation of radiative exciplexes near the interface or microcavities have been suggested as an explanation.[236] Faria et al. in fact use this effect to tune the color of green OLEDs. The same redshift could be observed for PTAA where the emission maximum shifts to a wavelength of 590 nm. For both materials, crosslinking the underlying layer reduces the shift in wavelength.
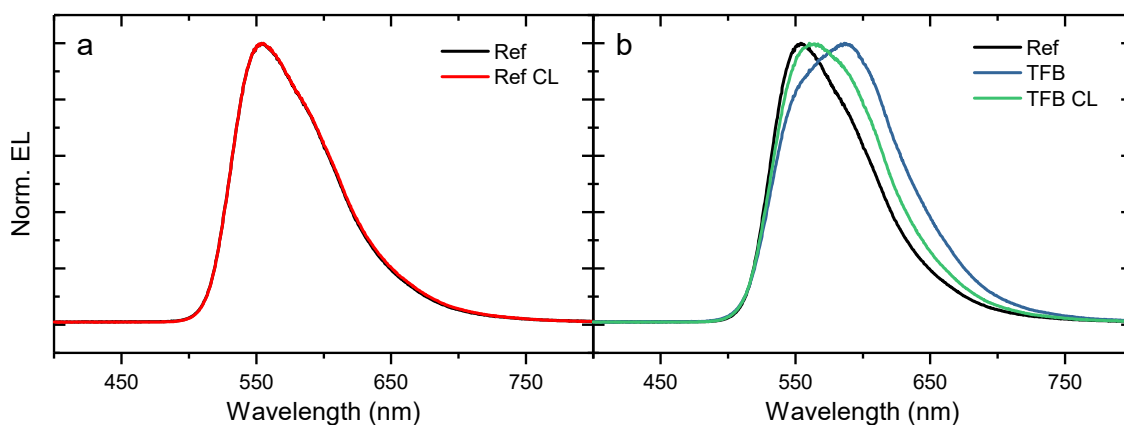
Figure 6.7. EL spectra. (a) comparison between a crosslinked and a non-crosslinked device. No difference in EL is visible. (b) TFB shifts the EL emission stronger on non-crosslinked devices.

As discussed earlier, the dissolution of previously deposited layers does not only depend on the solubility of the layer but also on the contact time between layer and solvent. Therefore, it is suggested that faster processing can lead to more effective devices. This was investigated by spin coating an EBL of TFB onto (CL-)SY at different processing speeds. However, this does not mean that the rotation speed of the spin coater was increased, but rather that the spin coating

process was started as fast as possible after the deposition of the solution. Compared to previous results with TFB, the addition of the EBL to the device now exhibits an increase in current efficacy for both, the crosslinked and non-crosslinked device as can be seen in Figure 6.8. While the reference reaches 3.2 cd A^{-1}, 4.1 cd A^{-1} was achieved with CL-SY plus EBL and 4.2 cd A^{-1} on non-crosslinked SY. This means that reducing the contact time can be more beneficial than introducing a crosslinker.

Figure 6.8. Influence of processing speed on device efficacy. If TFB is processed more quickly, the efficacy can be increased even on non-crosslinked devices. This is only possible for some fabrication techniques.

Yet not all fabrication systems allow faster processing. Mainly for blade coating techniques, the thickness of the resulting layer relies on the blade speed, which therefore cannot be easily changed. As these are more scalable techniques and are thus more industry-relevant, crosslinking becomes an even more valuable procedure to obtain solutio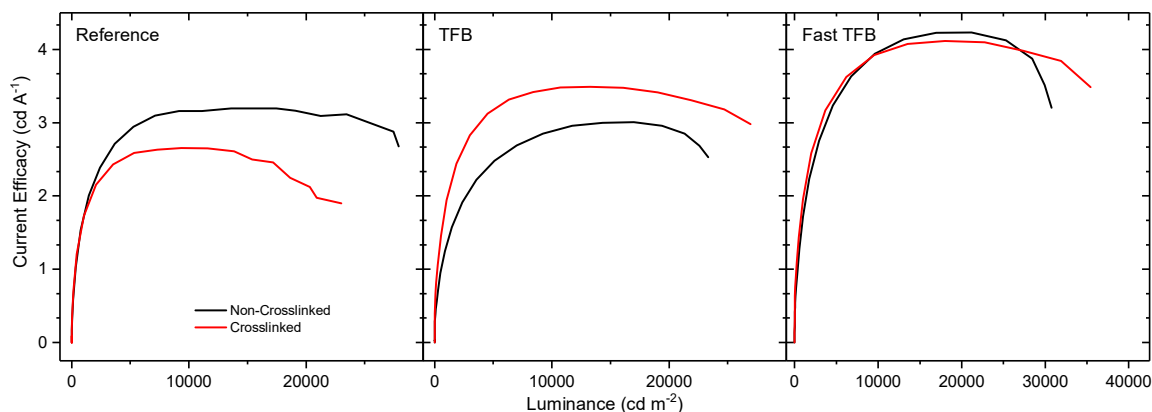n-processed multilayers. This was further investigated by fabricating devices with a 0.49 cm^2 active layer with the EBL being doctor bladed. Referring to the previous EL results, it was decided to use PTAA as the EB material due to its smaller shift in wavelength.

The results comparing spin-coated and doctor-bladed devices can be seen in Table 6.2 and Figure 6.9. Current densities of reference, non-crosslinked devices show the fastest onset in both cases, while all other devices are similar. Addition of PTAA decreases the flowing current. This effect is negated by crosslinking before addition of PTAA. Especially for doctor-bladed OLEDs, the current density of devices containing the EBL is nearly identical to the reference. This suggests that the decrease in current density is due to the toluene solvent attacking the underlying layer and partially dissolving it, allowing the SY and PTAA to mix. Comparing the luminance values, all spin-coated devices have the same turn-on voltage of 2.5 V expected for an emitter material with a bandgap of 2.4 eV. Adding PTAA on non-CL SY results in a turn-on of 4.0 V as the whole luminance curve is shifted to higher voltages. For doctor-bladed devices, the same trend is visible with turn-on voltages at 3 V being marginally higher.

Again, for non-CL PTAA devices, the luminance shifts, and the turn-on voltage is now lying at 4.5 V. As described before, crosslinking reduces the maximum luminance of devices without PTAA, in the case of spin-coated devices by 20% and by 46% if PTAA is added on non-CL devices. Device efficacies are comparable to literature values of OLEDs processed in ambient conditions.[237] Due to its superior solution stability, PTAA on crosslinked SY can return to

98% of the reference luminance. Lower current density, however, enables these devices to have improved current efficacy.

For doctor-bladed devices, crosslinking and the addition of PTAA lead to highly improved brightness with a maximum luminance of 20 600 cd m^{-2}, an increase of 78% compared to the reference. Remarkably, as can be seen in Figure 6.9f, devices are now highly efficient with a maximum efficacy of 6.5 cd A^{-1}. Notably, the efficacy roll-off at higher luminance values is greatly decreased. This effect is being attributed in literature to charge imbalance, bimolecular quenching processes, or the influence of heat or an electric field.[238,239] Addition of an EBL interlayer can therefore reduce these processes most likely by balancing the charge carriers. CIE coordinates stay nearly constant for all spin-coated and doctor-bladed devices except in the case of non-crosslinked OLEDs with PTAA. The EL shift caused by the PTAA consequently also alters the CIE coordinates as can be seen in Table 6.2.

Table 6.2. Turn-on voltage V_{on}, luminance L, current efficacy η_c, and CIE1931 coordinates of fabricated OLEDs.

	Type	V_{on} (V)	Peak L (cd m^{-2})	η_c (cd A^{-1}) @ L (cd m^{-2})			Peak η_c (cd A^{-1})	CIE1931	
				100	1000	10 000		x	y
0.04 cm^2	Ref	2.5	49 986	0.54	1.80	4.33	4.85	0.48	0.51
	Ref CL	2.5	40 153	0.48	1.90	4.42	4.69	0.48	0.50
	PTAA	4.0	27 065	0.39	1.23	5.14	2.86	0.51	0.47
	PTAA CL	2.5	49 078	0.72	2.27	2.66	5.75	0.49	0.50
0.49 cm^2	Ref	3.0	11 531	2.12	4.00	3.45	4.14	0.45	0.53
	Ref CL	3.0	11 120	1.75	3.05	3.24	3.62	0.46	0.52
	PTAA	4.5	11 513	0.80	1.88	3.39	3.44	0.48	0.50
	PTAA CL	3.0	20 606	1.79	4.70	6.32	6.48	0.46	0.53
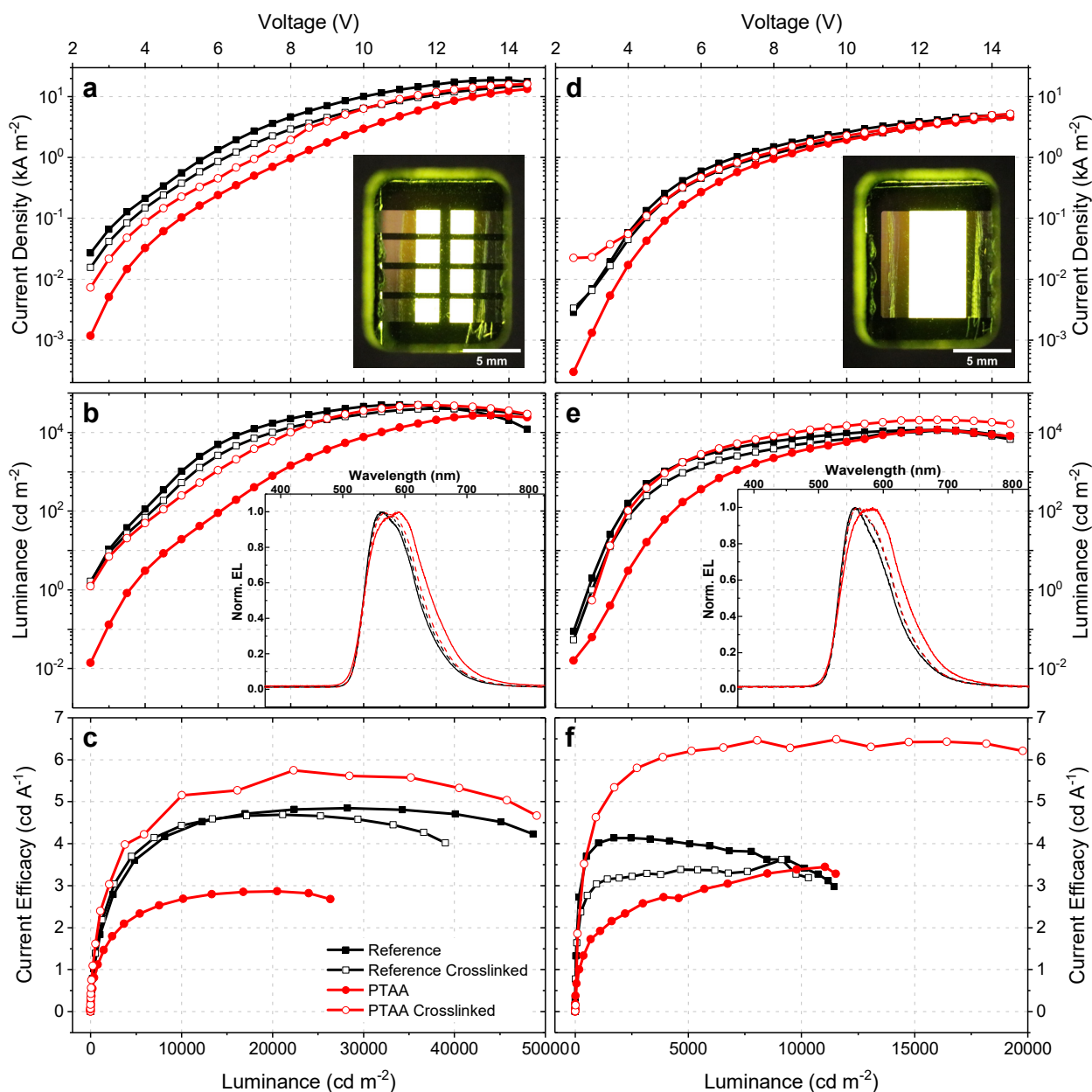
Figure 6.9. JVL characterization of devices fabricated with spin-coated EBL (left) and doctor-bladed EBL (right). While crosslinking of Super-Yellow does reduce the density (a, d) and luminance (b, e) of both device types, adding a PTAA EBL (on crosslinked SY) improves efficacy (c, f). Especially on doctor-bladed devices, the EBL is also able to greatly delay the efficacy roll-off. Insets in a and d show running devices at 4 V. As previously mentioned, PTAA on non-crosslinked SY leads to a redshift in the EL spectra (insets in b and e).

6.6 Conclusion

In conclusion, it could be shown that crosslinking is a viable option to facilitate solution processing of multilayer devices. A novel bisazide crosslinker was successfully employed to improve the solvent resistivity of the commonly used emitter material Super Yellow. Crosslinking properties were studied via TGA and FTIR and washing tests with crosslinked layers confirmed their stability. The crosslinking process did not alter the PL or EL emission spectrum of SY.

Crosslinking enabled the processing of an electron blocking layer from a toluene solution, the same solvent as used for the emitter material. It could be shown that fast processing can be as effective as crosslinking but is not suitable for all production techniques. Different EBL materials were investigated and PTAA was found to be the most promising option. A thinner layer of PTAA resulted in the biggest device improvements.

Devices produced via spin coating and including a PTAA EBL displayed improved luminance as well as current efficacy. The introduction of PTAA led to efficacies up to 5.8 cd A^{-1}. Increasing the active area by transferring the process to the scalable technique of doctor blading, the positive influence of the EBL was even more evident. Luminance could be increased by 78%, reaching values of 20 000 cd m^{-2} and current efficacy by 56% with maximal values of 6.5 cd A^{-1}. Compared to reference devices without the EBL, the efficacy roll-off was significantly decreased, hinting at an effective charge balancing by the blocking layer.

While the crosslinking could be performed successfully it is still not clear which reaction mechanism can be used to explain the crosslinking of PPV materials in this case. Further experiments are needed here. Since the effect of the EBL has been shown to be more pronounced in larger devices, continued upscaling to even larger OLEDs could strengthen the reputation of solution processing as a viable alternative to vapor deposition. Production of fully solution-processed OLEDs is greatly facilitated by employing crosslinkers.

7 Conclusion and Outlook

OLEDs have the potential to revolutionize the lighting and display market due to their low power consumption and good optical abilities. Their stability and lifetime have been drastically improved in recent years. Furthermore, the wasteful evaporation process of today's OLED production is slowly being superseded by solution processing. This new development comes with its own set of challenges such as the question of how to manufacture stable but bendable electrodes or how to fabricate multilayer devices. This thesis has presented some insights into these questions. After a theoretical first part (Chapters 1 and 2), production and measurement setups were developed while in the second part novel materials were introduced into the OLED structure to improve the device's properties and performance. In particular, the following aspects were described:

Chapter 3 introduced custom-built setups to facilitate the production and characterization of devices. For the characterization of OLEDs, two setups were created. Fist, a JVL measurement station, which enables fast and precise measurements of OLEDs. This setup was used for the characterization of all OLEDs in this work. Secondly, an EQE setup using an integrating sphere to assess the OLED's external quantum efficiency. From simple lab equipment, a low-cost haze measurement setup was developed to evaluate the quality of transparent films. This setup allows to quickly compare the qualitative haze of different samples. Lastly, a laser structuring process was implemented and its parameters were evaluated. It was then used in practice to pattern electrodes for upscaled OLED devices.

The fabrication of metal electrodes was shown in chapter 4. A particle-free silver metal-decomposition ink was utilized to create transparent, conductive electrodes. These were shown to be viable alternatives to the commonly used brittle ITO. On flexible PET substrates, silver electrodes showed improved bending stability when compared to ITO. Integrated into OLED devices, silver electrodes on glass were able to outperform ITO electrodes in terms of brightness (10 000 cd m^{-2}) as well as efficacy (5.3 cd A^{-1}). Processed onto flexible substrates, OLEDs showed high durability to bending stress, losing only 2% of the maximum brightness after 150 bending cycles. In contrast, ITO devices lost 99% of their brightness after only a few bends. This makes flexible printed electrodes highly suitable for flex-to-install applications. In a second step, gold electrodes were fabricated from similar metal-decomposition inks using. The electrodes showed lower transparency but higher resistance to oxidation than silver electrodes. Implementation in OLEDs was shown as a proof of concept and resulted in working devices.

Chapter 5 dealt with novel materials to improve device efficacies. In the first part, a composite mixture of zinc oxide and polyethyleneimine was introduced as an electron injection layer. Different ratios of ZnO:PEI and their processing parameters were studied, and the optimal parameters were found to be a 2:1 ratio, a ZnO particle size of 12 nm, and a spin coating speed of 4500 rpm. With these parameters, highly efficient inverted OLEDs were able to be produced reaching up to 4.5 cd A^{-1}. The second part of the chapter explored the potential of two novel molecules as substitutes for PTAA, which does not allow good wetting of perovskite materials. While the hole-conductivity of the new materials was found to be significantly lower, they considerably improved the wetting, enabling inkjet printing of perovskite layers which was not possible on PTAA.

Finally, chapter 6 explored the possibility of cross-linking an emitter layer to create multilayer devices. A novel bisazide crosslinker was utilized to crosslink the emitter material Super Yellow. Crosslinked films showed high solvent resistivity and were able to be incorporated into inverted OLEDs. Spin-coated from the same solvent, an additional layer of PTAA acts as an electron blocking layer. OLEDs incorporating the PTAA layer displayed a heigher luminance up to 20 000 cd m^{-2} (78% increase) as well as an improved efficacy of 6.5 cd A^{-1} (56% increase). The insertion of an electron blocking layer improved the charge carrier balance, evidenced by a reduced efficacy roll-off.

Outlook

The development and improvement of organic light-emitting diodes is still an ongoing process. New materials are being investigated every day and new architectures are tested. Therefore, it is hard to foresee how OLED technology will develop in the next years and decades. Nevertheless, a small outlook can be given as to how the topics of this work can be further developed.

As already described in the main text, the measurement and characterization stations built during this work will be further improved. They have to be adapted to larger devices as upscaling OLEDs is one of the big future goals. At the moment, standard OLEDs in this thesis had an acive area of 4 mm^2 and 49 mm^2. However, work is already underway on scaling up to sizes of 1 inch^2 or 25 cm^2. Automatization of the setups is also preferred to minimize user interactions. The data received must be stored in a suitable format that is as openly accessible as possible as for example in the FAIRmat project at Helmholtz-Zentrum Berlin.

The fabricated electrodes from chapter 4 will further be tested not only for OLED but also for other electronic applications such as solar cells or other sensors. When silver is not a suitable material, gold electrodes may be applied. Additional metals, such as platinum or palladium are being investigated at the time of writing and can also be a future suitable electrode material. The ZnO:PEI interlayer discussed in chapter 5 is actively being applied in the standard recipe for inverted OLEDs within the Hybrid Devices group at Humboldt-Universität zu Berlin. Ternary blends, already reported in literature can be investigated in the future, including hole-blocking molecules or other materials in the mix.[240] The novel molecules to improve wetting have to be further tested in devices. As was shown, they can enable perovskite printing on PTAA-type materials. Polymerization of the molecules is an ongoing goal for the synthesis collaborators from Heidelberg university. Lastly, the multilayer OLED structure and the

crosslinking approach discussed in chapter 6 can be further analyzed. The novel bisazide crosslinker still has to show its potential as a universal, additive crosslinker and has to be tested with other material combinations.

In summary, combining all the approaches from this thesis, multilayer, large-area all-solution processed OLEDs can be seen as an achievable goal for the future.

8 List of Publications

The following publications were produced during this doctorate:

1. Hengge, M., Livanov, K., Zamoshchik, N., Hermerschmidt, F., & List-Kratochvil, E. J. W. (2021). ITO-free OLEDs utilizing inkjet-printed and low temperature plasma-sintered Ag electrodes. Flexible and Printed Electronics, 6(1), 015009. https://doi.org/10.1088/2058-8585/abe604

2. Hermerschmidt, F., Hengge, M., Schröder, V. R., Hänsch, P., Livanov, K., Zamoshchik, N., & List-Kratochvil, E. J. W. (2021). A guide to qualitative haze measurements demonstrated on inkjet-printed silver electrodes for flexible OLEDs. In T.-W. Lee, F. So, & C. Adachi (Eds.), Organic and Hybrid Light Emitting Materials and Devices XXV (Issue August 2021, p. 5). SPIE. https://doi.org/10.1117/12.2594486

3. Hengge, M., Hänsch, P., Ehjeij, D., Benneckendorf, F. S., Freudenberg, J., Bunz, U. H. F., Müllen, K., List-Kratochvil, E. J. W., Hermerschmidt, F. (2022). Crosslinking Super-Yellow to produce super OLEDs: Crosslinking with azides enables improved performance. J. Polym. Sci., 1. https://doi.org/10.1002/pol.20220120

References

[1]   "The long history of light-emitting diodes - Electronic Products," can be found under https://www.electronicproducts.com/the-long-history-of-light-emitting-diodes/, **2011**.

[2]   S. Nakamura, T. Mukai, M. Senoh, *Appl Phys Lett* **1998**, *64*, 1687.

[3]   "OLED Display Market Size, Share," can be found under https://extrapolate.com/Semiconductor-Electronics/oled-display-market/25719, **2022**.

[4]   A. Monkman, *ACS Appl Mater Interfaces* **2021**, *14*, DOI 10.1021/ACSAMI.1C09189.

[5]   "OLED Lifetime: introduction and market status | OLED-Info," can be found under https://www.oled-info.com/oled-lifetime, **2021**.

[6]   T. L. Heath, *A History of Greek Mathematics: From Aristarchus to Diophantus*, Dover Publications, Inc., New Yok, **1981**.

[7]   In *Commission Internationale de l'Éclairage Proceedings, 1924*, Cambridge University Press, Cambridge, **1926**.

[8]   Y. Ohno, T. Goodman, P. Blattner, J. Schanda, H. Shitomi, A. Sperling, J. Zwinkels, *Metrologia* **2020**, *57*, 020401.

[9]   W. D. Wright, *Transactions of the Optical Society* **1929**, *30*, 141.

[10]   B. J. Guild, F. InstP, *Philosophical Transactions of the Royal Society of London. Series A, Containing Papers of a Mathematical or Physical Character* **1931**, *230*, 149.

[11]   M. Orchin, R. S. Macomber, A. R. Pinhas, R. M. Wilson, in *The Vocabulary and Concepts of Organic Chemistry*, **2005**, pp. 1–24.

[12]   A. Köhler, H. Bässler, *Electronic Processes in Organic Semiconductors: An Introduction* **2015**, 1.

[13]   C. Kittel, *Introduction to Solid State Physics*, John Wiley & Sons, Inc., **1953**.

[14]   A. Kahn, *Mater Horiz* **2016**, *3*, 7.

[15]   K. Ehinger, S. Summerfield, S. Roth, *Colloid Polym Sci* **1985**, *263*, 714.

[16]   J. C. S. Costa, R. J. S. Taveira, C. F. R. A. C. Lima, A. Mendes, L. M. N. B. F. Santos, *Opt Mater (Amst)* **2016**, *58*, 51.

[17]   J. Casado, T. M. Pappenfus, L. L. Miller, K. R. Mann, E. Ortí, P. M. Viruela, R. Pou-Amérigo, V. Hernández, J. T. López Navarrete, *J Am Chem Soc* **2003**, *125*, 2524.

[18]   D. Cahen, A. Kahn, *Advanced Materials* **2003**, *15*, 271.

[19]   I. Yavuz, *Physical Chemistry Chemical Physics* **2017**, *19*, 25819.

[20]   Y. Tsutsui, G. Schweicher, B. Chattopadhyay, T. Sakurai, J. Arlin, C. Ruzié, A. Aliev, A. Ciesielski, S. Colella, A. R. Kennedy, V. Lemaur, Y. Olivier, R. Hadji, L. Sanguinet, F. Castet, S. Osella, D. Dudenko, D. Beljonne, J. Cornil, P. Samorì, S. Seki, Y. H. Geerts, *Advanced Materials* **2016**, *28*, 7106.

[21]   R. Silbey, R. W. Munn, *J Chem Phys* **1980**, *72*, 2763.

[22]   Martin Pope, C. E. Swenberg, *Electronic Processes in Organic Crystals and Polymers*, **1999**.

[23]   R. A. Marcus, N. Sutin, *Biochimica et Biophysica Acta (BBA) - Reviews on Bioenergetics* **1985**, *811*, 265.

[24]   A. H. Castro Neto, F. Guinea, N. M. R. Peres, K. S. Novoselov, A. K. Geim, *Rev Mod Phys* **2009**, *81*, 109.

[25]   H. Ishii, K. Sugiyama, E. Ito, K. Seki, *Advanced Materials* **1999**, *11*, 605.

[26]   K. Seki, N. Hayashi, H. Oji, E. Ito, Y. Ouchi, H. Ishii, *Thin Solid Films* **2001**, *393*, 298.

[27]   J. Bardeen, *Physical Review* **1947**, *71*, 717.

[28]   H. Sugimoto, H. Hasebe, T. Furuyama, M. Fujii, *Small* **2021**, *17*, 2104458.

[29]   J. Chavez, L. Ceresa, E. Kitchner, J. Kimball, T. Shtoyko, R. Fudala, J. Borejdo, Z. Gryczynski, I. Gryczynski, *J Photochem Photobiol B* **2020**, *208*, 111897.

[30]   O. Gabriel, "File:Franck-Condon-Prinzip.svg - Wikimedia Commons," can be found under https://commons.wikimedia.org/wiki/File:Franck-Condon-Prinzip.svg, **2007**.

[31]   M. M. Somoza, "File:Vibration-fluor-abs.png - Wikimedia Commons," can be found under https://commons.wikimedia.org/wiki/File:Vibration-fluor-abs.png, **2006**.

[32]   N. Ashcroft, D. Mermin, *Solid State Physics*, Harcourt College Publishers, **1976**.

[33]   S. Dushman, *Physical Review* **1923**, *21*, 623.

[34]   R. H. Fowler, L. Nordheim, *Proceedings of the Royal Society A* **1928**, *119*, 173.

[35]   G. Haacke, *J Appl Phys* **2008**, *47*, 4086.

[36]   R. A. Hatton, M. R. Willis, M. A. Chesters, D. Briggs, *J Mater Chem* **2003**, *13*, 722.

[37]   R. B. Pode, C. J. Lee, D. G. Moon, J. I. Han, *Appl Phys Lett* **2004**, *84*, 4614.

[38]   S. Conoci, S. Petralia, P. Samorì, F. M. Raymo, S. di Bella, S. Sortino, *Adv Funct Mater* **2006**, *16*, 1425.

[39]   L. Hu, H. Wu, Y. Cui, *MRS Bull* **2011**, *36*, 760.

[40]   K. Banzai, S. Naka, H. Okada, *Jpn J Appl Phys* **2015**, *54*, 054101.

[41]   Z. Zhao, T. L. Alford, *Solar Energy Materials and Solar Cells* **2016**, *157*, 599.

[42]   A. I. Hofmann, E. Cloutet, G. Hadziioannou, *Adv Electron Mater* **2018**, *4*, 1700412.

[43]   Y. Cao, G. M. Treacy, P. Smith, A. J. Heeger, *Appl Phys Lett* **1998**, *60*, 2711.

[44]   S. Kirchmeyer, K. Reuter, *J Mater Chem* **2005**, *15*, 2077.

[45]   L. Kinner, F. Hermerschmidt, T. Dimopoulos, E. J. W. List-Kratochvil, *physica status solidi (RRL) – Rapid Research Letters* **2020**, *14*, 2000305.

[46] S. Azoubel, S. Shemesh, S. Magdassi, *Nanotechnology* **2012**, *23*, 344003.

[47] M. Luo, Y. Liu, W. Huang, W. Qiao, Y. Zhou, Y. Ye, L.-S. Chen, *Micromachines (Basel)* **2017**, *8*, 12.

[48] F. Hermerschmidt, I. Burgués-Ceballos, A. Savva, E. D. Sepos, A. Lange, C. Boeffel, S. Nau, E. J. W. List-Kratochvil, S. A. Choulis, *Flexible and Printed Electronics* **2016**, *1*, 035004.

[49] R. Braunstein, *Physical Review* **1955**, *99*, 1892.

[50] A. Bernanose, M. Comte, P. Vouaux, *Journal de Chimie Physique* **1953**, *50*, 64.

[51] M. Sano, M. Pope, H. Kallmann, *J Chem Phys* **1965**, *43*, 2920.

[52] W. Helfrich, W. G. Schneider, *Phys Rev Lett* **1965**, *14*, 229.

[53] C. W. Tang, S. A. VanSlyke, *Appl Phys Lett* **1987**, *51*, 913.

[54] P. A. Tipler, R. A. Llewellyn, *Modern Physics*, Oldenbourg, Houndmills, **2003**.

[55] P. Schulz, J. O. Tiepelt, J. A. Christians, I. Levine, E. Edri, E. M. Sanehira, G. Hodes, D. Cahen, A. Kahn, *ACS Appl Mater Interfaces* **2016**, *8*, 31491.

[56] W. Brütting, C. Adachi, *Physics of Organic Semiconductors*, Wiley, **2012**.

[57] S. R. Forrest, *Philos Trans A Math Phys Eng Sci* **2015**, *373*, DOI 10.1098/RSTA.2014.0320.

[58] K. Stavrou, L. G. Franca, A. P. Monkman, *ACS Appl Electron Mater* **2020**, *2*, 2868.

[59] S. W. Jung, K. S. Kim, H. un Park, R. Lampande, S. K. Kim, J. H. Kim, C. W. Han, H. C. Choi, J. H. Kwon, *Adv Electron Mater* **2021**, *7*, 2001101.

[60] S. Han, X. Feng, Z. H. Lu, D. Johnson, R. Wood, *Appl Phys Lett* **2003**, *82*, 2715.

[61] J. Meyer, T. Winkler, S. Hamwi, S. Schmale, M. Kröger, P. Görrn, H.-H. Johannes, T. Riedl, E. Lang, D. Becker, T. Dobbertin, W. Kowalsky, *https://doi.org/10.1117/12.734051* **2007**, *6655*, 148.

[62] G. Nisato, M. Kuilder, P. Bouten, L. Moro, O. Philips, N. Rutherford, *SID Symposium Digest of Technical Papers* **2003**, *34*, 550.

[63] J.-S. Kim, P. K. H. Ho, N. C. Greenham, R. H. Friend, *J Appl Phys* **2000**, *88*, 1073.

[64] S. Nowy, B. C. Krummacher, J. Frischeisen, N. A. Reinke, W. Brütting, *J Appl Phys* **2008**, *104*, 123109.

[65] R. Windisch, P. Heremans, A. Knobloch, P. Kiesel, G. H. Döhler, B. Dutta, G. Borghs, *Appl Phys Lett* **1999**, *74*, 2256.

[66] L. Kinner, S. Nau, K. Popovic, S. Sax, I. Burgués-Ceballos, F. Hermerschmidt, A. Lange, C. Boeffel, S. A. Choulis, E. J. W. List-Kratochvil, *Journal of Polymer Science* **2022**, *110*, 101107.

[67] S. R. Forrest, D. D. C. Bradley, M. E. Thompson, *Advanced Materials* **2003**, *15*, 1043.

[68] H. Uoyama, K. Goushi, K. Shizu, H. Nomura, C. Adachi, *Nature* **2012**, *492*, 234.

[69] P. Wang, S. Wu, *J Photochem Photobiol A Chem* **1995**, *86*, 109.

[70] A. Köhler, H. Bässler, *Electronic Processes in Organic Semiconductors: An Introduction* **2015**, 1.

[71] G. A. H. Wetzelaer, M. Kuik, M. Lenes, P. W. M. Blom, *Appl Phys Lett* **2011**, *99*, 153506.

[72] Lindholm, J. G. Fossum, E. L. Burgess, *IEEE Trans Electron Devices* **1979**, *26*.

[73] W. Shockley, *Bell System Technical Journal* **1949**, *28*, 435.

[74] G.-J. Wetzelaer, Charge Transport and Recombination in Organic-Semiconductor Diodes, PhD Thesis, University of Groningen, **2014**.

[75] C. B. Honsberg, S. G. Bowden, "Photovoltaics Education Website," can be found under www.pveducation.org, **2019**.

[76] C. A. Gueymard, D. Myers, K. Emery, *Solar Energy* **2002**, *73*, 443.

[77] P. Krüger, R. Knes, J. Friedrich, *Surf Coat Technol* **1999**, *112*, 240.

[78] K. B. Lim, D. C. Lee, *Surface and Interface Analysis* **2004**, *36*, 254.

[79] Z. H. Huang, X. T. Zeng, X. Y. Sun, E. T. Kang, J. Y. H. Fuh, L. Lu, *Org Electron* **2008**, *9*, 51.

[80] K. Norrman, A. Ghanbari-Siahkali, N. B. Larsen, *Annual Reports Section "C" (Physical Chemistry)* **2005**, *101*, 174.

[81] B. T. Chen, *Polym Eng Sci* **1983**, *23*, 399.

[82] F. C. Krebs, *Solar Energy Materials and Solar Cells* **2009**, *93*, 394.

[83] Y. T. Chou, Y. T. Ko, M. F. Yan, *Journal of the American Ceramic Society* **1987**, *70*, C.

[84] P. Calvert, *Chemistry of Materials* **2001**, *13*, 3299.

[85] G. Cummins, M. P. Y. Desmulliez, *Circuit World* **2012**, *38*, 193.

[86] B. Derby, *Annu Rev Mater Res* **2010**, *40*, 395.

[87] A. Klug, P. Patter, K. Popovic, A. Blümel, S. Sax, M. Lenz, O. Glushko, M. J. Cordill, E. J. W. List-Kratochvil, in *Https://Doi.Org/10.1117/12.2187422* (Ed.: E. J. W. List Kratochvil), SPIE, **2015**, p. 95690N.

[88] G. Sauerbrey, *Zeitschrift für Physik* **1959**, *155*, 206.

[89] J. Tauc, R. Grigorovici, A. Vancu, *physica status solidi (b)* **1966**, *15*, 627.

[90] P. Makuła, M. Pacia, W. Macyk, *J Phys Chem Lett* **2018**, *9*, 6814.

[91] U. Riaz, S. M. Ashraf, in *Characterization of Polymer Blends*, Wiley-VCH Verlag GmbH & Co. KGaA, Weinheim, Germany, **2014**, pp. 625–678.

References

[92] A. Einstein, *Ann Phys* **2005**, *14*, 164.

[93] H. Kirihata, M. Uda, *Review of Scientific Instruments* **1981**, *52*, 68.

[94] M. Heber, W. Grünert, *Top Catal* **2001**, *15*, 3.

[95] Y. Park, V. Choong, Y. Gao, B. R. Hsieh, C. W. Tang, *Appl Phys Lett* **1996**, *68*, 2699.

[96] K. Siegbahn, C. Nordling, *ESCA, Atomic, Molecular and Solid State Structure Studied by Means of Electron Spectroscopy*, Almqvist & Wiksell, **1967**.

[97] E. Sokolowski, C. Nordling, K. Siegbahn, *Physical Review* **1958**, *110*, 776.

[98] J. A. C. Santana, *Quantitative Core Level Photoelectron Spectroscopy*, **2015**.

[99] B. Cappella, G. Dietler, *Surf Sci Rep* **1999**, *34*, 1.

[100] F. J. Giessibl, *Rev Mod Phys* **2003**, *75*, 949.

[101] R. García, *Surf Sci Rep* **2002**, *47*, 197.

[102] N. A. Geisse, *Materials Today* **2009**, *12*, 40.

[103] D. Rugar, H. J. Mamin, P. Guethner, S. E. Lambert, J. E. Stern, I. McFadyen, T. Yogi, *J Appl Phys* **1990**, *68*, 1169.

[104] A. Noy, D. v. Vezenov, C. M. Lieber, *Annual Review of Materials Science* **1997**, *27*, 381.

[105] W. Melitz, J. Shen, A. C. Kummel, S. Lee, *Surf Sci Rep* **2011**, *66*, 1.

[106] P. Navard, J. M. Haudin, *Journal of Thermal Analysis* **1984**, *29*, 405.

[107] J. D. Menczel, L. Judovits, R. B. Prime, H. E. Bair, M. Reading, S. Swier, in *Thermal Analysis of Polymers: Fundamentals and Applications* (Eds.: J. D. Menczel, R. B. Prime), John Wiley & Sons, Ltd, **2008**, pp. 7–239.

[108] R. B. Prime, H. E. Bair, S. Vyazovkin, P. K. Gallagher, A. Riga, in *Thermal Analysis of Polymers: Fundamentals and Applications* (Eds.: J. D. Menczel, R. B. Prime), John Wiley & Sons, Ltd, **2008**, pp. 241–317.

[109] C. A. Wilkie, *Polym Degrad Stab* **1999**, *66*, 301.

[110] M. Yamashita, M. Agu, *Jpn J Appl Phys* **1984**, *23*, 1499.

[111] E. G. Shafrin, W. A. Zisman, *Journal of Physical Chemistry* **1960**, *64*, 519.

[112] B. Thomas Young, M. D. For Sec, *Philos Trans R Soc Lond* **1805**, *95*, 65.

[113] D. K. Owens, R. C. Wendt, *J Appl Polym Sci* **1969**, *13*, 1741.

[114] W. Rabel, *Farbe und Lack* **1971**, *77*, 997.

[115] D. H. Kaelble, *J Adhes* **1970**, *2*, 66.

[116] DataPhysics Instruments GmbH, "Anwendung der 'Wetting Envelope,'" can be found under https://www.dataphysics-instruments.com/Downloads/ 13_Anwendung_Wetting_Envelope.pdf, **2021**.

[117] M. E. Schrader, *Langmuir* **2002**, *11*, 3585.

[118] N. F. Mott, R. W. Gurney, *Oxford University Press* **1940**.

[119] J. A. Röhr, D. Moia, S. A. Haque, T. Kirchartz, J. Nelson, *Journal of Physics Condensed Matter* **2018**, *30*, DOI 10.1088/1361-648X/aaabad.

[120] F. Hermerschmidt, M. Hengge, V. R. Schröder, P. Hänsch, K. Livanov, N. Zamoshchik, E. J. W. List-Kratochvil, in *Organic and Hybrid Light Emitting Materials and Devices XXV* (Eds.: T.-W. Lee, F. So, C. Adachi), SPIE, **2021**, p. 5.

[121] ASTM D1003−21, *ASTM International* **2021**, *1*, 1.

[122] International Organization for Standardization, [ISO 13468-1:2019], Geneva **2019**.

[123] W. C. Liu, J. Hwang, A. Koo, H. Wu, R. Leecharoen, H. L. Yu, *J Phys Conf Ser* **2018**, *972*, 012023.

[124] B. Scharfe, S. Lehmann, T. Gerdes, D. Brüggemann, *Journal of Composites Science* **2019**, *3*, 101.

[125] O. Glushko, A. Klug, E. J. W. List-Kratochvil, M. J. Cordill, *J Mater Res* **2017**, *32*, 1760.

[126] M. J. Cordill, O. Glushko, J. Kreith, V. M. Marx, C. Kirchlechner, *Microelectron Eng* **2015**, *137*, 96.

[127] M. J. Cordill, O. Glushko, B. Putz, *Front Mater* **2016**, *3*, 1.

[128] G. B. Nair, S. J. Dhoble, in *The Fundamentals and Applications of Light-Emitting Diodes*, Elsevier, **2021**, pp. 3–33.

[129] T. Smith, J. Guild, *Optometry and Vision Science* **1947**, *24*, 576.

[130] J. Morovi, *Color Gamut Mapping*, John Wiley & Sons, Ltd, Chichester, UK, **2008**.

[131] S. Okamoto, K. Tanaka, Y. Izumi, H. Adachi, T. Yamaji, T. Suzuki, *Jpn J Appl Phys* **2001**, *40*, L783.

[132] M. Shukla, B. Nameeta, *Journal of Polymer Science* **2022**, *15*, 231.

[133] E. Archer, S. Hillebrandt, C. Keum, C. Murawski, J. Murawski, F. Tenopala-Carmona, M. C. Gather, *Adv Opt Mater* **2021**, *9*, 2000838.

[134] I. Tanaka, S. Tokito, *Jpn J Appl Phys* **2004**, *43*, 7733.

[135] S. R. Forrest, D. D. C. Bradley, M. E. Thompson, *Advanced Materials* **2003**, *15*, 1043.

[136] C. J. Huang, Y. K. Su, S. L. Wu, *Mater Chem Phys* **2004**, *84*, 146.

[137] Y. J. Lee, J. W. Bae, H. R. Han, J. S. Kim, G. Y. Yeom, *Thin Solid Films* **2001**, *383*, 281.

References

[138] S. Abreu Fernandes, B. Schoeps, K. Kowalick, R. Nett, C. Esen, M. Pickshaus, A. Ostendorf, *Phys Procedia* **2013**, *41*, 802.

[139] A. Risch, R. Hellmann, *Phys Procedia* **2011**, *12*, 133.

[140] K. H. Kim, S. J. Kwon, T. O. Tak, *Jpn J Appl Phys* **2008**, *47*, 197.

[141] M. Hengge, K. Livanov, N. Zamoshchik, F. Hermerschmidt, E. J. W. List-Kratochvil, *Flexible and Printed Electronics* **2021**, *6*, 015009.

[142] K. L. Chopra, S. Major, D. K. Pandya, *Thin Solid Films* **1983**, *102*, 1.

[143] H. Kim, C. M. Gilmore, A. Piqué, J. S. Horwitz, H. Mattoussi, H. Murata, Z. H. Kafafi, D. B. Chrisey, *J Appl Phys* **1999**, *86*, 6451.

[144] C. Peng, Z. Jia, H. Neilson, T. Li, J. Lou, *Adv Eng Mater* **2013**, *15*, 250.

[145] N. G. Semaltianos, *Appl Surf Sci* **2001**, *183*, 223.

[146] L. Kinner, M. Bauch, R. A. Wibowo, G. Ligorio, E. J. W. List-Kratochvil, T. Dimopoulos, *Mater Des* **2019**, *168*, 107663.

[147] W. Wu, *Nanoscale* **2017**, *9*, 7342.

[148] F. Hermerschmidt, S. A. Choulis, E. J. W. List-Kratochvil, *Adv Mater Technol* **2019**, *4*, 1800474.

[149] W. Yang, E. J. W. List-Kratochvil, C. Wang, *J Mater Chem C Mater* **2019**, *7*, 15098.

[150] M. Vaseem, S.-K. Lee, J.-G. Kim, Y.-B. Hahn, *Chemical Engineering Journal* **2016**, *306*, 796.

[151] Y. Choi, K. Seong, Y. Piao, *Adv Mater Interfaces* **2019**, *6*, 1901002.

[152] L. Kinner, E. J. W. List-Kratochvil, T. Dimopoulos, *Nanotechnology* **2020**, *31*, 365303.

[153] D. Azulai, T. Belenkova, H. Gilon, Z. Barkay, G. Markovich, *Nano Lett* **2009**, *9*, 4246.

[154] A. R. Rathmell, S. M. Bergin, Y.-L. Hua, Z.-Y. Li, B. J. Wiley, *Advanced Materials* **2010**, *22*, 3558.

[155] F. Hermerschmidt, D. Burmeister, G. Ligorio, S. M. Pozov, R. Ward, S. A. Choulis, E. J. W. List-Kratochvil, *Journal of Polymer Science* **2022**, *3*, 1800146.

[156] I. Reinhold, C. E. Hendriks, R. Eckardt, J. M. Kranenburg, J. Perelaer, R. R. Baumann, U. S. Schubert, *J Mater Chem* **2009**, *19*, 3384.

[157] F. M. Wolf, J. Perelaer, S. Stumpf, D. Bollen, F. Kriebel, U. S. Schubert, *J Mater Res* **2013**, *28*, 1254.

[158] S. Wünscher, S. Stumpf, J. Perelaer, U. S. Schubert, *J Mater Chem C Mater* **2014**, *2*, 1642.

[159] C. E. Knapp, J. Chemin, S. P. Douglas, D. A. Ondo, J. Guillot, P. Choquet, N. D. Boscher, *Journal of Polymer Science* **2022**, *3*, 1700326.

[160] D. Chen, H. G. Zachmann, *Polymer (Guildf)* **1991**, *32*, 1612.

[161] S. Wünscher, R. Abbel, J. Perelaer, U. S. Schubert, *J. Mater. Chem. C* **2014**, *2*, 10232.

[162] V. Bromberg, S. Ma, F. D. Egitto, T. J. Singler, *J Mater Chem C Mater* **2013**, *1*, 6842.

[163] I. Genish, A. Irzh, A. Gedanken, A. Anderson, A. Zaban, L. Klein, *Surf Coat Technol* **2010**, *204*, 1347.

[164] S. Dou, L. Tao, R. Wang, S. el Hankari, R. Chen, S. Wang, *Advanced Materials* **2018**, *30*, 1.

[165] N. Zamoshchik, K. Livanov, Y. Sheynin, *Method for Metal Layer Formation*, **2020**, US20200017974A1.

[166] Y. Zhou, C. Fuentes-Hernandez, J. Shim, J. Meyer, A. J. Giordano, H. Li, P. Winget, T. Papadopoulos, H. Cheun, J. Kim, M. Fenoll, A. Dindar, W. Haske, E. Najafabadi, T. M. Khan, H. Sojoudi, S. Barlow, S. Graham, J.-L. Brédas, S. R. Marder, A. Kahn, B. Kippelen, *Science (1979)* **2012**, *336*, 327.

[167] D. Mampallil, H. B. Eral, *Adv Colloid Interface Sci* **2018**, *252*, 38.

[168] B. Lafuente, R. T. Downs, H. Yang, N. Stone, in *Highlights in Mineralogical Crystallography*, DE GRUYTER, Berlin, München, Boston, **2015**, pp. 1–30.

[169] H. Cho, C. Yun, J.-W. Park, S. Yoo, *Org Electron* **2009**, *10*, 1163.

[170] Z. Jiang, S. Huang, B. Qian, *Electrochim Acta* **1994**, *39*, 2465.

[171] R. Serway, J. Jewett, *Principles of Physics A Calculus-Based Text*, Brooks/Cole, **2012**.

[172] L. S. Hung, C. W. Tang, M. G. Mason, *Appl Phys Lett* **1997**, *70*, 152.

[173] A. Berntsen, Y. Croonen, C. Liedenbaum, H. Schoo, R.-J. Visser, J. Vleggaar, P. van de Weijer, *Opt Mater (Amst)* **1998**, *9*, 125.

[174] K. Nie, H. Zhang, J. A. McLeod, D. Zhang, D. Zhou, Y. Xia, J. Zhong, L. Liao, J. Guo, X. Sun, *Org Electron* **2020**, *87*, 105901.

[175] S. Scholz, D. Kondakov, B. Lüssem, K. Leo, *Chem Rev* **2015**, *115*, 8449.

[176] J. Meyer, S. Hamwi, T. Bülow, H.-H. Johannes, T. Riedl, W. Kowalsky, *Appl Phys Lett* **2007**, *91*, 113506.

[177] H. M. Zhang, W. C. H. Choy, *J Phys D Appl Phys* **2008**, *41*, 062003.

[178] H. You, Y. Dai, Z. Zhang, D. Ma, *J Appl Phys* **2007**, *101*, 026105.

[179] R. Schlaf, H. Murata, Z. H. Kafafi, *J Electron Spectros Relat Phenomena* **2001**, *120*, 149.

[180] H. Kang, S. Hong, J. Lee, K. Lee, *Advanced Materials* **2012**, *24*, 3005.

[181] N. Tokmoldin, N. Griffiths, D. D. C. Bradley, S. A. Haque, *Advanced Materials* **2009**, *21*, 3475.

[182] M. Sessolo, H. J. Bolink, *Advanced Materials* **2011**, *23*, 1829.

[183] Y.-J. Pu, N. Morishita, T. Chiba, S. Ohisa, M. Igarashi, A. Masuhara, J. Kido, *ACS Appl Mater Interfaces* **2015**, *7*, 25373.

[184] S. Höfle, A. Schienle, M. Bruns, U. Lemmer, A. Colsmann, *Advanced Materials* **2014**, *26*, 2750.

[185] A. Mai, Implementierung Eines Standardrezepts Für Die Herstellung von Invertierten Organischen Leuchtdioden, Bachelor Thesis, Humboldt-Universität zu Berlin, **2018**.

[186] R. Kaçar, S. P. Mucur, F. Yıldız, S. Dabak, E. Tekin, *Nanotechnology* **2017**, *28*, 245204.

[187] S. P. Mucur, T. A. Tumay, S. Birdoğan, S. E. San, E. Tekin, *Nano-Structures & Nano-Objects* **2015**, *1*, 7.

[188] E. A. Meulenkamp, *J Phys Chem B* **1998**, *102*, 5566.

[189] P. de Bruyn, D. J. D. Moet, P. W. M. Blom, *Org Electron* **2010**, *11*, 1419.

[190] Z. Zhong, Z. Hu, Z. Jiang, J. Wang, Y. Chen, C. Song, S. Han, F. Huang, J. Peng, J. Wang, Y. Cao, *Adv Electron Mater* **2015**, *1*, 1400014.

[191] J. S. Manser, J. A. Christians, P. v. Kamat, *Chem Rev* **2016**, *116*, 12956.

[192] N. G. Park, *Materials Today* **2015**, *18*, 65.

[193] W. Zhang, Y.-C. Wang, X. Li, C. Song, L. Wan, K. Usman, J. Fang, W. Zhang, Y. Wang, X. Li, C. Song, L. Wan, K. Usman, J. Fang, *Advanced Science* **2018**, *5*, 1800159.

[194] M. Xiao, M. Gao, F. Huang, A. R. Pascoe, T. Qin, Y. Cheng, U. Bach, L. Spiccia, *ChemNanoMat* **2016**, *2*, 182.

[195] W. Deng, X. Liang, P. S. Kubiak, P. J. Cameron, *Adv Energy Mater* **2018**, *8*, 1701544.

[196] Y. Xia, S. Dai, *Journal of Materials Science: Materials in Electronics* **2021**, *32*, 12746.

[197] K. M. Reza, S. Mabrouk, Q. Qiao, *Proceedings of the Nature Research Society* **2018**, *2*, 02004.

[198] D. B. Khadka, Y. Shirai, M. Yanagida, J. W. Ryan, K. Miyano, *J Mater Chem C Mater* **2017**, *5*, 8819.

[199] M. Stolterfoht, P. Caprioglio, C. M. Wolff, J. A. Márquez, J. Nordmann, S. Zhang, D. Rothhardt, U. Hörmann, Y. Amir, A. Redinger, L. Kegelmann, F. Zu, S. Albrecht, N. Koch, T. Kirchartz, M. Saliba, T. Unold, D. Neher, *Energy Environ Sci* **2019**, *12*, 2778.

[200] F. Huang, A. R. Pascoe, W.-Q. Wu, Z. Ku, Y. Peng, J. Zhong, R. A. Caruso, Y.-B. Cheng, F. Z. Huang, Z. L. Ku, Y. Peng, J. Zhong, Y. Cheng, A. R. Pascoe, W. Wu, R. A. Caruso, *Advanced Materials* **2017**, *29*, 1601715.

[201] C. Xu, Z. Liu, E.-C. Lee, *J Mater Chem C Mater* **2018**, *6*, 6975.

[202] K. O. Brinkmann, J. He, F. Schubert, J. Malerczyk, C. Kreusel, F. van gen Hassend, S. Weber, J. Song, J. Qu, T. Riedl, *ACS Appl Mater Interfaces* **2019**, *11*, 40172.

[203] A. E. Shalan, *Mater Adv* **2020**, *1*, 292.

[204] J. Küffner, T. Wahl, M. Schultes, J. Hanisch, J. Zillner, E. Ahlswede, M. Powalla, *ACS Appl Mater Interfaces* **2020**, *12*, 52678.

[205] J. You, F. Guo, S. Qiu, W. He, C. Wang, X. Liu, W. Xu, Y. Mai, *Journal of Energy Chemistry* **2019**, *38*, 192.

[206] X. Xu, C. Ma, Y. Cheng, Y. M. Xie, X. Yi, B. Gautam, S. Chen, H. W. Li, C. S. Lee, F. So, S. W. Tsang, *J Power Sources* **2017**, *360*, 157.

[207] S. Zhang, M. Stolterfoht, A. Armin, Q. Lin, F. Zu, J. Sobus, H. Jin, N. Koch, P. Meredith, P. L. Burn, D. Neher, *ACS Appl Mater Interfaces* **2018**, *10*, 21681.

[208] Y. Yang, Q. Yuan, H. Li, Y. Niu, D. Han, Q. Yang, Y. Yang, S. Yi, D.-Y. Zhou, L. Feng, *Org Electron* **2020**, *86*, 105873.

[209] A. Al-Ashouri, A. Magomedov, M. Roß, M. Jošt, M. Talaikis, G. Chistiakova, T. Bertram, J. A. Márquez, E. Köhnen, E. Kasparavičius, S. Levcenco, L. Gil-Escrig, C. J. Hages, R. Schlatmann, B. Rech, T. Malinauskas, T. Unold, C. A. Kaufmann, L. Korte, G. Niaura, V. Getautis, S. Albrecht, *Energy Environ Sci* **2019**, *12*, 3356.

[210] Y. Ko, Y. Kim, C. Lee, Y. Kim, Y. Jun, *ACS Appl Mater Interfaces* **2018**, *10*, 11633.

[211] W. Zhang, J. Smith, R. Hamilton, M. Heeney, J. Kirkpatrick, K. Song, S. E. Watkins, T. Anthopoulos, I. McCulloch, *J Am Chem Soc* **2009**, *131*, 10814.

[212] M. Sendner, J. Trollmann, A. Pucci, *Org Electron* **2014**, *15*, 2959.

[213] M. Hengge, P. Hänsch, D. Ehjeij, F. S. Benneckendorf, J. Freudenberg, U. H. F. Bunz, K. Müllen, E. J. W. List-Kratochvil, F. Hermerschmidt, *Journal of Polymer Science* **2022**, 1.

[214] S. Palsaniya, H. B. Nemade, A. K. Dasmahapatra, *The Journal of Physical Chemistry C* **2019**, *123*, 27959.

[215] Y. Ohnishi, R. Kita, K. Tsuchiya, S. Iwamori, *Jpn J Appl Phys* **2016**, *55*, 02BB04.

[216] K. P. Gritsenko, A. M. Krasovsky, *Chem Rev* **2003**, *103*, 3607.

[217] M. Auer-Berger, R. Trattnig, T. Qin, R. Schlesinger, M. v. Nardi, G. Ligorio, C. Christodoulou, N. Koch, M. Baumgarten, K. Müllen, E. J. W. List-Kratochvil, *Org Electron* **2016**, *35*, 164.

[218] A. Köhnen, M. Irion, M. C. Gather, N. Rehmann, P. Zacharias, K. Meerholz, *J Mater Chem* **2010**, *20*, 3301.

[219] S. Burns, J. MacLeod, T. Trang Do, P. Sonar, S. D. Yambem, *Journal of Polymer Science* **2022**, *7*, 40805.

[220] W. Li, Q. Wang, J. Cui, H. Chou, S. E. Shaheen, G. E. Jabbour, J. Anderson, P. Lee, B. Kippelen, N. Peyghambarian, N. R. Armstrong, T. J. Marks, *Advanced Materials* **1999**, *11*, 730.

References

[221] H. Yan, P. Lee, N. R. Armstrong, A. Graham, G. A. Evmenenko, P. Dutta, T. J. Marks, *J Am Chem Soc* **2005**, *127*, 3172.

[222] C. A. Zuniga, S. Barlow, S. R. Marder, *Chemistry of Materials* **2011**, *23*, 658.

[223] A. Bacher, C. H. Erdelen, W. Paulus, H. Ringsdorf, H. W. Schmidt, P. Schuhmacher, *Macromolecules* **1999**, *32*, 4551.

[224] G. Wu, C. Yang, B. Fan, B. Zhang, X. Chen, Y. Li, *J Appl Polym Sci* **2006**, *100*, 2336.

[225] M. S. Bayerl, T. Braig, O. Nuyken, D. C. Müller, M. Groß, K. Meerholz, *Macromol Rapid Commun* **1999**, *20*, 224.

[226] C. D. Müller, A. Falcou, N. Reckefuss, M. Rojahn, V. Wiederhirn, P. Rudati, H. Frohne, O. Nuyken, H. Becker, K. Meerholz, *Nature* **2003**, *421*, 829.

[227] M. Hengge, P. Hänsch, D. Ehjeij, F. S. Benneckendorf, J. Freudenberg, U. H. F. Bunz, K. Müllen, E. J. W. List-Kratochvil, F. Hermerschmidt, *Journal of Polymer Science* **2022**, 1.

[228] P. Hänsch, Azide Based Cross-Linker for Multilayer Solution Processed Organic Light Emitting Diodes, **2020**.

[229] R. E. Banks, G. R. Sparkes, *J Chem Soc Perkin 1* **1972**, 2964.

[230] L. Kinner, T. Dimopoulos, G. Ligorio, E. J. W. List-Kratochvil, F. Hermerschmidt, *RSC Adv* **2021**, *11*, 17324.

[231] J. H. Noh, S. H. Im, J. H. Heo, T. N. Mandal, S. il Seok, *Nano Lett* **2013**, *13*, 1764.

[232] J.-S. Kim, R. H. Friend, I. Grizzi, J. H. Burroughes, *Appl Phys Lett* **2005**, *87*, 023506.

[233] J. H. Heo, S. H. Im, J. H. Noh, T. N. Mandal, C.-S. Lim, J. A. Chang, Y. H. Lee, H. Kim, A. Sarkar, M. K. Nazeeruddin, M. Grätzel, S. il Seok, *Nat Photonics* **2013**, *7*, 486.

[234] Q. J. Sun, J. H. Hou, C. H. Yang, Y. F. Li, Y. Yang, *Appl Phys Lett* **2006**, *89*, 153501.

[235] S. Ochiai, P. Kumar, K. Santhakumar, P.-K. Shin, *Electronic Materials Letters* **2013**, *9*, 399.

[236] J. C. D. Faria, A. J. Campbell, M. A. McLachlan, *J Mater Chem C Mater* **2015**, *3*, 4945.

[237] C. Amruth, M. Z. Szymański, B. Łuszczyńska, J. Ulański, *Sci Rep* **2019**, *9*, 8493.

[238] A. Soman, M. M, K. N. N. Unni, *Opt Mater (Amst)* **2018**, *79*, 413.

[239] C. Murawski, K. Leo, M. C. Gather, *Advanced Materials* **2013**, *25*, 6801.

[240] R. Kaçar, S. P. Mucur, F. Yıldız, S. Dabak, E. Tekin, *Appl Phys Lett* **2018**, *112*, 163302.